

Morphology and Molecular Dynamics of Polyethylene by ^1H Solid-State NMR

Von der Fakultät für Mathematik, Informatik und Naturwissenschaften der
RWTH Aachen University zur Erlangung des akademischen Grades eines
Doktors der Naturwissenschaften genehmigte Dissertation

vorgelegt von

NING SUN, M. Ing.

aus Zhejiang, Volksrepublik China

Berichter: Universitätsprofessor Dr. Dr. h.c. Bernhard Blümich
Professor Dr. rer. nat. Frank Haarmann

Tag der mündlichen Prüfung: 14.12.2012

Diese Dissertation ist auf den Internetseiten der Hochschulbibliothek online verfügbar.

Die vorliegende Arbeit wurde in der Zeit von August 2009 bis Juli 2012 am Lehrstuhl für Makromolekulare Chemie der Rheinisch-Westfälischen Technischen Hochschule Aachen angefertigt. Herrn Prof. Dr. Dr. h.c. Bernhard Blümich danke ich für die Übernahme der wissenschaftlichen Betreuung dieser Promotionsarbeit. Für die freundliche Übernahme des Korreferats danke ich Herrn Prof. Dr. rer. nat. Frank Haarmann.

To Prof. Dr. Du-Xing Chen, my mentor also my friend.

静以修身，俭以养德。

—孔明《诫子书》

Mit Wissen kommt das Denken und mit dem
Denken der Ernst und die Kraft in die Menge.

Alexander von Humboldt

Abstract

A correlation study on the characterization of polyethylene was carried out between DSC and solid-state NMR. Both methods define the crystallinity of polyethylene precisely, and the benefit of solid-state NMR is its ability to describe the three-component phase composition based on the different molecular dynamics. The results provided by NMR-MOUSE are highly in agreement with those determined by DSC or high-field NMR in a wide crystallinity range. Besides, with the advantages of an open sensor, nondestructive investigation on polyethylene pipes was carried out by NMR-MOUSE which has potential applications in the quality control of plastic pipe productions.

Aging of polyethylene pipes due to the hydrostatic pressure and elevated temperature was investigated by spin-diffusion NMR. Morphological and molecular dynamical changes induced by physical aging were observed. Depending on the fracture types, the changes behave differently which are in turn decided by the applied pressures as well as the failure stages. The fundamental phenomenon of pipe aging is the embrittlement of molecular chains in the amorphous phase which, subsequently, reduces the mechanical resistance of the material against slow crack growth. Therefore, as a consequence, the long term performance of the pipes deteriorates. The current study also indicates that PE100 is an excellent candidate for piping solutions which is able to meet a wide range of end-user specifications.

Morphological and molecular dynamical changes of polyethylene due to the presence of carbon nanotubes were investigated by ^1H high-field NMR. The crystallinity and lamella thickness of polyethylene decreases with increasing amount of nanotubes. This is induced by a chain confinement effect which influences the crystallization kinetics of polyethylene when cooling from the melt. The change of residual dipolar coupling determined by the modified

phase selectable double-quantum pulse sequence indicates that interactions between polymer matrix and nanotubes influence the amorphous phase most remarkably. They increase the chain restrictions and reduce the conformation diversities in this region. Both the above aspects influence the mechanical strength and the thermal stability of carbon nanotube polyethylene composite.

Zusammenfassung

In der folgenden Arbeit wurde eine Korrelationsstudie bezüglich der Morphologie von Polyethylen zwischen DDK und der Festkörper-NMR durchgeführt. Über beide Methoden kann die Kristallinität untersucht werden, jedoch bietet die Festkörper-NMR nicht nur die Möglichkeit die kristallinen und amorphen Bereiche zu untersuchen, sondern auch die Zwischenphase. Die Ergebnisse, die mittels NMR-MOUSE aufgenommen worden sind, korrelieren bezüglich der Kristallinität über weite Bereiche mit den Werten, die mit der DDK und Hochfeld-NMR aufgenommen worden sind. Aufgrund dieser Resultate und der hervorragenden Korrelation besitzt die NMR-MOUSE, als zerstörungs- und kontaktfreie Messmethode, großes Potential im Bereich der Qualitätskontrolle von Kunststoffrohren in der Produktion.

Darüber hinaus wurde die Alterung von Polyethylen Rohren durch den hydrostatischen Druck und erhöhter Temperatur mittels Spin-Diffusions-NMR untersucht. Es konnten sowohl morphologische als auch molekular-dynamische Änderungen aufgrund der physikalischer Alterung beobachtet werden. Je nach Art der Fraktur konnten Veränderungen festgestellt werden, die auf die verwendeten Drücke und des zeitabhängigen Fortschreitens der Fehlstellen zurückzuführen sind. Die Hauptursache der Alterung des Rohres ist die Versprödung der Molekülketten in der amorphen Phase, die den Widerstand des Materials gegen langsames Risswachstum reduziert. Auf diese Weise verschlechtert sich die langfristige Leistungsfähigkeit der Rohre. Die Studie zeigt auch, dass PE100 ein exzellenter Kandidat für Rohrleitungs-Lösungen ist und eine Vielfalt an Spezifikationen für verschiedene Anwendungen erfüllt.

Morphologische und molekulare dynamische Änderungen von Polyethylen wurden durch das Vorhandensein von Kohlenstoff-Nanoröhren mittels ^1H

Hochfeld-NMR untersucht. Die Kristallinität und Lamellendicke von Polyethylen nimmt mit zunehmender Menge von Nanoröhren ab. Dies wird durch einen Einschränkungseffekt auf die Kette verursacht, die die Kristallisation von Polyethylen beim Abkühlen der Schmelze beeinflusst. Die Änderung der restlichen dipolaren Kopplungen, bestimmt durch die modifizierte Phase der wählbaren Doppel-Quanten-Impulsfolge darauf, beeinflusst die Struktureigenschaftsbeziehungen zwischen der Polymermatrix und der Nanoröhren in der amorphen Phase. Sie erhöhen die Kettenbeweglichkeit und reduzieren Vielfalt an Konformationen in dieser Region. Die oben genannten Aspekte beeinflussen sowohl die mechanische Festigkeit und die thermische Stabilität von diesen Nanoverbundwerkstoffen.

Contents

List of Figures	xv
List of Tables	xix
List of Symbols	xxi
List of Abbreviations	xxvii
1 Introduction	1
2 Fundamentals	5
2.1 Polyethylene Morphology	6
2.1.1 Lamella	7
2.1.2 Phase Composition	8
2.2 Polyethylene Molecular Dynamics	10
2.2.1 Translation and Rotation in the Crystalline Phase	10
2.2.2 Crankshaft Motion in the Amorphous Phase	11
2.2.3 Cooperative Motion in the Interphase	12
2.2.4 Molecular Relaxations	13
2.3 NMR Molecular Relaxation	14
2.3.1 Transverse Relaxation	14
2.3.2 Longitudinal Relaxation	16
2.4 NMR Experimental Methods	17
2.4.1 NMR Equipments	18
2.4.2 Pulse Sequences	19

CONTENTS

3	Correlation of DSC and Solid-State NMR in a PE Study	23
3.1	Materials	24
3.2	Characterization by DSC	24
3.2.1	DSC Measurement	24
3.2.2	Crystallinity and Melting Behavior	24
3.3	Characterization by High-Field ^1H FID	26
3.3.1	^1H FID Measurement	27
3.3.2	Model Fit	27
3.3.3	Dead Time Dependence	29
3.3.4	Phase Composition and Relaxation Times – I	32
3.4	Characterization by NMR-MOUSE	33
3.4.1	NMR-MOUSE Relaxation Measurement	33
3.4.2	Data Interpretation	34
3.4.3	Effective Transverse Relaxation Time	35
3.4.4	Phase Composition and Relaxation Times – II	37
3.5	Correlation	38
3.5.1	Phase Composition	38
3.5.2	Relaxation Times	40
3.5.3	Evaluation of Different Methods	41
3.6	Application of NMR-MOUSE to PE Pipes	42
3.6.1	Samples and Correlation	42
3.6.2	Gradients across the Wall	43
3.6.3	Residual Stress	44
3.7	Summary	45
4	Study on Aging of HDPE Pipes by Solid-State NMR	47
4.1	Materials	48
4.2	Aging of HDPE Pipes	48
4.2.1	Hydrostatic Pressure Test	49
4.2.2	Hoop Stress	49
4.3	Phase Composition and Chain Relaxation	52
4.3.1	DSC and ^1H NMR Relaxation Measurements	52
4.3.2	Crystallinity Determined by DSC	53

4.3.3	Phase Composition Determined by ^1H FID	54
4.3.4	Relaxation Times	55
4.3.5	Hoop Stress Correlation in Stage II Failure – I	56
4.4	Domain Sizes by ^1H Spin-Diffusion NMR	58
4.4.1	Spin-Diffusion Measurement	58
4.4.2	Analytical Solutions	59
4.4.3	Spin-Diffusion Coefficients	62
4.4.4	Spin-Diffusion Curves	63
4.4.5	Domain Sizes	65
4.4.6	Hoop Stress Correlation in Stage II Failure – II	66
4.5	Aging Mechanism	67
4.5.1	Annealing and Creep	67
4.5.2	Ductile Fracture versus Brittle Fracture	68
4.5.3	Slow Crack Growth	69
4.6	Summary	71
5	Study of MWNT/LDPE Composite by Solid-State NMR	73
5.1	Materials	74
5.2	Thermal Properties	74
5.2.1	TGA Measurement	75
5.2.2	Thermal Stability and Decomposition	75
5.3	Morphology and Molecular Relaxation	77
5.3.1	^1H FID and DSC Measurement	77
5.3.2	Crystallinity Determined by DSC	77
5.3.3	Lamella Thickness	78
5.3.4	Phase Composition Determined by ^1H FID	80
5.3.5	Transverse Relaxation Times of Solid Composite	80
5.3.6	Transverse Relaxation Time of Composite Melt	81
5.4	^1H Residual Dipolar Coupling by Double-Quantum NMR	83
5.4.1	Dipolar Filter	83
5.4.2	Double-Quantum Measurement	85
5.4.3	Double-Quantum Curves	86
5.4.4	Residual Dipolar Coupling	92

CONTENTS

5.5	MWNT/LDPE Structure and Properties	94
5.5.1	Influence on the Crystallization Kinetics	94
5.5.2	Nanohybrid Shish-Kebab Structure	96
5.5.3	MWNT/LDPE Physical Properties	98
5.6	Summary	99
6	Conclusions and Outlooks	101
	Appendix	105
A	Probe Body Temperature Calibration	105
B	Temperature Dependence of NMR Results	106
C	Systematic Error of DSC	108
D	Systematic Error of NMR-MOUSE	109
E	Systematic Error of High-Field NMR	110
F	Inhomogeneity of PEHD Pipes	111
	References	113
	Acknowledgements	135
	Curriculum Vitæ	137

List of Figures

2.1	Chemical structure of pure polyethylene.	6
2.2	<i>n</i> -alkane chain fold.	7
2.3	Three-component phase model.	9
2.4	Chain translation and rotation in the crystalline phase.	11
2.5	Crankshaft motion in the amorphous phase.	12
2.6	NMR sensors.	18
2.7	Pulse sequences for transverse relaxation measurement.	20
2.8	Pulse sequences for longitudinal relaxation measurement.	21
3.1	DSC traces of PE.	25
3.2	¹ H free induction decay of PE and the fit.	29
3.3	¹ H FID of PE recorded with different dead times.	30
3.4	Dead time influence on ¹ H FID fit.	30
3.5	Dead time dependence of ¹ H FID fit result.	31
3.6	¹ H solid echo decay of PE and the fit.	34
3.7	¹ H longitudinal relaxation recovery of PE and the fit.	35
3.8	Initial echoes of the decays with different echo times.	36
3.9	Solid echo decay and the second echo of the decays with different echo times.	37
3.10	Correlation of PE characterization between DSC and NMR.	39
3.11	Correlation of transverse relaxation times with crystallinity.	40
3.12	Correlation of longitudinal relaxation time with crystallinity.	41
3.13	Phase composition correlation of HDPE pipes determined by high- field NMR and NMR-MOUSE.	42

LIST OF FIGURES

3.14	Morphological gradient of HDPE pipes across the wall.	43
3.15	Effective transverse relaxation times of HDPE pipes across the wall.	44
4.1	Schematic diagram of the standard hydrostatic pressure test setup.	49
4.2	Fracture types and hoop stress.	50
4.3	Crystallinity and melting temperature with storage time determined by DSC.	53
4.4	Phase composition with storage time determined by ^1H FID.	54
4.5	Transverse relaxation times with storage time determined by ^1H FID.	55
4.6	Longitudinal relaxation time with storage time determined by inversion recovery pulse sequence.	56
4.7	Correlation between hoop stress and phase composition.	57
4.8	Correlation between hoop stress and relaxation times.	57
4.9	Spin-diffusion pulse sequence with a double-quantum dipolar filter.	59
4.10	Morphological model for spin-diffusion analytical solutions.	60
4.11	^1H broad line spectrum and deconvolution.	63
4.12	^1H spin-diffusion spectra with different mixing times.	64
4.13	^1H spin-diffusion curves and the fit.	64
4.14	Dependence of the domain sizes on the storage time.	65
4.15	Long period versus storage time.	66
4.16	Correlation between hoop stress and domain size.	66
4.17	Schematic diagram of slow crack growth.	69
5.1	TGA traces of LDPE and MWNT/LDPE composite.	76
5.2	Correlation between melting temperature and crystallinity.	79
5.3	Lamella thickness of MWNT/LDPE nanocomposite.	79
5.4	Phase composition of LDPE nanocomposite determined by ^1H FID.	80
5.5	Transverse relaxation times of LDPE nanocomposite determined by ^1H FID.	81
5.6	^1H FID of LDPE nanocomposite melts.	82
5.7	Transverse relaxation time of LDPE nanocomposite melts.	82
5.8	Spin energy level encodings by double-quantum dipolar filter.	84

LIST OF FIGURES

5.9	Double-quantum pulse sequence with a phase selection filter.	85
5.10	^1H double-quantum spectra with a phase selection period of $\tau_{\text{r}} = 3\ \mu\text{s}$ and different excitation/reconversion times.	87
5.11	^1H double-quantum spectra with a phase selection period of $\tau_{\text{r}} = 40\ \mu\text{s}$ and different excitation/reconversion times.	88
5.12	^1H double-quantum spectra with a phase selection period of $\tau_{\text{r}} = 190\ \mu\text{s}$ and different excitation/reconversion times.	89
5.13	Double-quantum buildup curves of LDPE with different phase selection times.	90
5.14	Double-quantum buildup curves of MWNT/LDPE composite with different phase selection periods.	91
5.15	Fit result of double-quantum buildup curves at the initial excitation/reconversion period.	93
5.16	Residual dipolar coupling and second van Vleck moment.	93
5.17	Nanohybrid shish-kebab supermolecular structure.	97
I	Temperature calibration of NMR solid probe bodies.	106
II	Temperature dependence of phase composition of PE determined by ^1H FID.	107
III	Temperature dependence of transverse relaxation times of PE determined by ^1H FID.	107

LIST OF FIGURES

List of Tables

3.1	Crystallinity, melting temperature, and crystallization temperature of PE determined by DSC.	25
3.2	Phase composition and transverse relaxation times of PE determined by high-field ^1H FID.	32
3.3	Phase composition and relaxation times of PE determined by NMR-MOUSE.	38
5.1	Thermal decomposition parameters of MWNT/LDPE composites determined by TGA.	76
5.2	Crystallinity, melting temperature, and crystallization temperature of MWNT/LDPE composites determined by DSC.	78
I	Systematic error of DSC.	108
II	Systematic error of NMR-MOUSE.	109
III	Systematic error of high-field NMR.	110
IV	Inhomogeneity of PEHD pipe determined by DSC.	111
V	Inhomogeneity of PEHD pipe determined by high-field ^1H FID.	112

LIST OF TABLES

List of Symbols

Symbol	Definition	Unit
α	molecular relaxation in the crystalline phase	–
β	molecular relaxation in the interphase	–
\mathbf{B}_0	static magnetic field	T
\mathbf{B}_1	radiofrequency magnetic field	T
\mathbf{B}_{loc}	local magnetic field	T
χ_0	product of ω_0 and τ_c	–
Δh_m	melting enthalpy	J/g
Δh_m^0	melting enthalpy of 100% crystals	J/g
$\Delta\nu_{1/2}$	line width at half height of broad line spectra	Hz
ΔW	DSC heat flow	mW/mg
δ	stress concentrating factor	–
D	spin-diffusion coefficient	nm ² /ms
D_{res}	residual dipolar coupling	kHz
d	domain size	nm
d_w	wall thickness of the pipe	mm
ϵ	stress exponent in slow crack growth	–
η_0, η_1	reinforce coefficients of nanocomposite	–
E_a^g	activation energy of crystal growth	kJ/mol

Continued on next page

List of Symbols

Continued from previous page

Symbol	Definition	Unit
E_a^n	activation energy of nucleation	kJ/mol
E_a^s	activation energy of slow crack growth	kJ/mol
E_c	Young's modulus of composite	MPa
E_n	Young's modulus of MWNT	MPa
E_p	Young's modulus of neat polymer matrix	MPa
F_k	lattice function of spin k	J
f	fraction of the "tie" and "loop" molecules	–
Γ	stress intensity	MPa/m ^{3/2}
γ	molecular relaxation in the amorphous phase	–
γ_g	gyromagnetic ratio	1/(s·T)
\hbar	Planck's constant over 2π	J·s
ι	exponent for Ω estimation	–
I	signal intensity	–
J	spin-diffusion flux	A·kg/(m ⁶ ·s)
κ	exponent of stretched exponential decay function	–
K	crystallization rate constant	–
λ	calibration constant of K	–
L_c	lamella thickness	nm
M_2	second van Vleck moment	kHz ²
$\overline{M_w}$	weight average molecular mass	kg/mol
M_{xy}	transverse magnetization	A/m
M_z	longitudinal magnetization	A/m

Continued on next page

Continued from previous page

Symbol	Definition	Unit
m	magnetization concentration	A/m ⁴
m_r	residual mass determined by TGA	–
ν	frequency	Hz
n	degree of polymerization	–
Ω	mechanical resistance against slow crack growth	–
ω_0	Larmor frequency	Hz
ϕ	sinusoidal constant in Abragam function	–
ψ	fraction of longitudinal relaxation	–
ρ	proton density	mol/m ³
ρ_{cm}	crystal density	kg/m ³
ρ_t	density of “tie” and “loop” molecules	kg/m ³
R	gas constant	J/(mol·K)
$\langle r^2 \rangle$	mean square distance between the nearest spins	nm ²
\mathbf{r}_k	radius vector from spin k to its nuclear neighbors	–
σ	hoop stress	MPa
σ_e	average energy on the chain folding surface	erg/cm ²
σ_r	fitting residual	–
S_{DQ}	normalized double-quantum signal	–
τ_c	molecular correlation time	μs
τ_{DQ}	double-quantum coherence period	μs
τ_d	varying delay time in saturation recovery and inversion recovery pulse sequences	μs

Continued on next page

List of Symbols

Continued from previous page

Symbol	Definition	Unit
τ_e	echo time in Hahn, CPMG, or solid echo pulse sequences	μs
$\tau_{e/r}$	excitation/reconversion time in dipolar filter	μs
τ_i	time interval between phase selection filter and dipolar filter	μs
τ_m	spin-diffusion mixing time	μs
τ_r	phase selection period	μs
θ_k	angle between \mathbf{r}_k and \mathbf{B}_0	rad
T	temperature	K
T_1	longitudinal (spin-lattice) relaxation time	s
$T_{1\rho}$	longitudinal relaxation time in rotating frame	s
T_2	transverse (spin-spin) relaxation time	μs
T_2^m	transverse relaxation time of polymer melt	μs
$T_{2\text{eff}}$	effective transverse relaxation time	μs
T_c	crystallization temperature	K
T_{end}	end temperature of thermal analysis	K
T_g	glass transition temperature	K
$T_{\text{inflection}}$	inflection temperature of thermal analysis	K
T_m	melting temperature	K
T_m^0	melting temperature of 100% crystal	K
T_{onset}	onset temperature of thermal analysis	K
T_p	programmed probe body temperature	K
T_r	real sample temperature in the probe body	K

Continued on next page

Continued from previous page

Symbol	Definition	Unit
t	time	s
t_d	instrumental dead time of NMR spectrometer	μs
t_s	storage time	h
V_1, V_2	extrusion throughput of PE pipes	kg/h
V_f	free volume	m^3
V_n	volume fraction of nanofiller	–
w	phase composition fraction	–
ξ	Avrami exponent	–
ζ	cut off parameter of Lorentzian line shape	Hz

List of Symbols

List of Abbreviations

Abbreviation	Full wording
CNT	carbon nanotube
CPMG	Carr-Purcell-Meiboom-Gill pulse sequence
DDK	Dynamische Differenzkalorimetrie
DSC	differential scanning calorimetry
FID	free induction decay
GPC	gel permeation chromatography
HDPE	high density polyethylene
IAP	Institut für Angewandte Polymerchemie
IR	infrared spectroscopy
LDPE	low density polyethylene
MAS	magic angle spinning
MDPE	medium density polyethylene
MWNT	multi-wall nanotube
NMR	nuclear magnetic resonance
NMR-MOUSE [®]	NMR mobile universal surface explorer
OW4	Ostroff-Waugh pulse sequence
PE	polyethylene

Continued on next page

List of Abbreviations

Continued from previous page

Abbreviation	Full wording
PE80	HDPE class ¹
PE100	HDPE class ²
PEHD	HDPE class ³
PP	polypropylene
rf	radiofrequency
SCG	slow crack growth
SKZ	Süddeutsches Kunststoff-Zentrum
STDV	standard deviation
TEM	transmission electron microscopy
TGA	thermogravimetric analysis
XRD	X-ray diffraction

¹HDPE class for pipe industry

²current best HDPE class for pipe industry

³lower HDPE class

1

Introduction

Solid-state nuclear magnetic resonance (NMR) has matured as a highly appreciated technique for material science and technology. In the last decades, various NMR methods cornering to different nuclei have been explored and developed for the investigation of polymer structures and properties.^[1-8] Among all, ^1H NMR is still the most efficient one, thanks to its advantages including high sensitivity, time saving, easy going, and superlatively informative. Based on the correlation between structure and properties, ^1H NMR is able to provide detailed information which will lead to the further development of material research in the future.

There are many different NMR techniques, for instance, relaxation, spin-diffusion, and double-quantum that have been well established to elucidate the ^1H nuclear environments in polymer materials. NMR relaxation is the simplest and the most effective method. It is able to extract various parameters and, thus, to describe the morphology as well as molecular dynamics of the material. The current widely used relaxation pulse sequences include single 90° , Hahn,^[9] CPMG (Carr-Purcell-Meiboom-Gill),^[10,11] saturation recovery, and inversion recovery pulse sequences. Free induction decay (FID) recorded after a single 90° pulse has been proved to be the most effective NMR method to describe the phase composition and molecular dynamics of semicrystalline polymers.^[12-15] Besides, the recovery signal of the longitudinal relaxation is able to estimate the morphological domain dimensions of the material.^[16,17] Furthermore, Blümich *et al.*^[18-20] have explored the possibility of employing mobile single-sided NMR on the char-

1 Introduction

acterization of solid polymers with relaxation methods, recently. The positive results promise its application to the study of plastic materials and, thus, heightened the contributions of NMR in materials investigations significantly.

In addition to all the advantages mentioned above, solid-state NMR is also able to provide other more detailed information by describing the behavior and interactions of spin pairs. Two typical techniques as spin-diffusion NMR and double-quantum NMR are widely used. Spin-diffusion NMR is elaborated by the diffusion coefficients and the distance of the magnetization transfer. It is particularly useful for the quantitative determination of domain sizes depending on the different spin diffusivities in different phases. Nowadays, sufficiently reliable analytical solutions have been established^[21–25] which enable spin-diffusion NMR as a convenient method to describe the morphology of semicrystalline polymers. On the other hand, double-quantum NMR deals with the dipolar couplings between spin pairs which reflects the intra- and intermolecular interactions between protons. It is widely used to investigate the crosslinks of elastomer networks and their interaction with the inorganic fillers. Up to now, different fitting models are available to estimate the coupling information of the spin pairs in the polymer matrix,^[26–30] and it is worthwhile to explore the applications of double-quantum NMR to semicrystalline polymers.

This Ph.D. work focuses on the study of morphology and molecular dynamics of polyethylene by ^1H solid-state NMR. The main designation of such work is to establish the connections between molecular information and properties of semicrystalline polymers, thus, to explain their physical performances. This issue helps to figure out the application difficulties of the materials and, consequently, improve their contributions in different utilization fields. Besides, as one of the most informative techniques, the further improvement of the application of solid-state NMR to materials research is also a very important topic. This includes the exploration of new NMR methods that suitable for diversified material systems and the investigation of different NMR hardwares for a wider application to the material study.

To meet such ends, three major topics were studied and will be presented: first, investigation of the application of mobile single-sided NMR to the plastic industry; second, study on aging of polyethylene pipes by solid-state NMR; and

third, study of carbon nanotube polyethylene composite by solid-state NMR. This dissertation will, therefore, first introduce the principal basis for the application of solid-state NMR to semicrystalline polymers in Chapter 2, in which the molecular motions and the nuclear magnetic relaxation mechanisms will be highlighted. In Chapter 3, a correlation study of the characterization of polyethylene with different methods will be presented and, at the same time, the nondestructive detection of the morphological and molecular dynamical gradients across the high density polyethylene pipe wall by mobile single-sided NMR will be introduced in Section 3.6. Afterwards in Chapter 4, by investigating the domain sizes via spin-diffusion NMR in Section 4.4, the aging mechanism of high density polyethylene pipes due to hydrostatic pressure and elevated temperature will be discussed on a molecular level in Section 4.5. Chapter 5 presents the study of carbon nanotube low density polyethylene composite, in which by investigating the ^1H residual dipolar couplings in the amorphous phase in Section 5.4, the change of physical properties of the nanocomposite due to the presence of nanotubes will be explained in Section 5.5. Finally, by speculating on the perspectives of solid-state NMR in material science and technology, the work will be concluded in Chapter 6.

1 Introduction

2

Fundamentals

Polyethylene (PE) is a very important material as an integral part of our daily lives. It was first reported by von Pechmann in 1898 by the decomposition of diazomethane.^[31] However, its potential importance was not recognized until 1930s when Friedrich and Marvel inadvertently created PE from ethylene.^[32] In 1950s, the invention of Ziegler-Natta catalyst led to the development of coordination polymerization which made the production of essentially linear high density polyethylene (HDPE) possible.^[33,34] Consequently, the application fields of PE broadened significantly and, thus, increased its commercial demand dramatically. Nowadays, thanks to its versatilities with respects of the mechanical properties, easy processability and recyclability at a relatively low cost, as well as the easily available raw materials, PE becomes one of the most widely used thermoplastic polymers. PEs with different densities and structures are able to fulfill diverse applications industrially and domestically. The current annual consumption of PE is approximately 70 million tons,^[35] and its main service fields cover cables, moldings, pipes, films, and so on.

The investigation of chemical and physical properties of PE has been carried out since its appearance. In the last several decades, various techniques such as X-ray diffraction (XRD), mechanical measurement, infrared spectroscopy (IR), dielectric measurement, differential scanning calorimetry (DSC), transmission electron microscopy (TEM), gel permeation chromatography (GPC), and solid-state NMR have been established to study the different aspects of PE. Its

2 Fundamentals

structure and chain arrangement, phase composition and morphology, as well as molecular dynamics in different phases have been intensively investigated. Generally, different analytical methods are based on different principles, thus, the obtained information is also different. One of the most notable advantages of solid-state NMR over its counterparts is the abilities to distinguish the phase components of semicrystalline polymeric materials based on their different chain motions and relaxations in a detailed way.^[36,37] Besides, by combining different NMR techniques richer information can be extracted which helps to understand the properties of the material better. Furthermore, the wide detection range of molecular motion frequencies by NMR, from 10^{-1} to 10^{12} Hz, guarantees its feasibility for diversified molecular conditions. In the last decade, solid-state NMR has been widely applied to study the phase composition, molecular relaxations, phase domain dimensions, as well as molecular interactions of PE in different situations.^[38-43]

2.1 Polyethylene Morphology

PE is the simplest polymer molecule which consists of a backbone with a great number of covalently linked carbon atoms. Simultaneously, a pair of hydrogen atoms attaches on each carbon atom. As shown in Figure 2.1, PE is an n -alkane, where n is the polymerization degree which ranges from 100 to as high as 250 000 or even more. In chemically pure PE, the terminals of each polymer chain are methyl groups. Depending on the polymerization methods, the molecular chains can be either linear, branched, or crosslinked. The different degrees and lengths of the branches or the different crosslink densities of PE are the main reasons for its diversified categories.

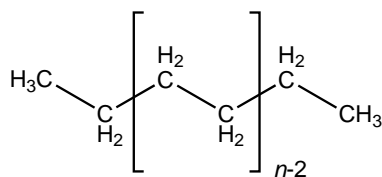


Figure 2.1: Chemical structure of pure PE.

2.1.1 Lamella

In linear PE, due to the smallest atomic volume of hydrogen, the steric effects between alkane units against the chemical bond rotation is the lowest. Besides, the uniformly nonpolar molecular chains eliminate the intra- or intermolecular electrostatic interactions. Therefore, long PE chains are highly flexible. In addition, due to the total symmetric structure along the backbone, these n -alkane chains strongly intend to fold back to themselves in regular arrays.^[44] Figure 2.2(a) shows a regular tight chain folding model, in which the chains form 180° folds then re-enter into the nearest adjacent neighboring site in the (001) plane. This type of fold is known as the adjacent re-entry model.^[45–47]

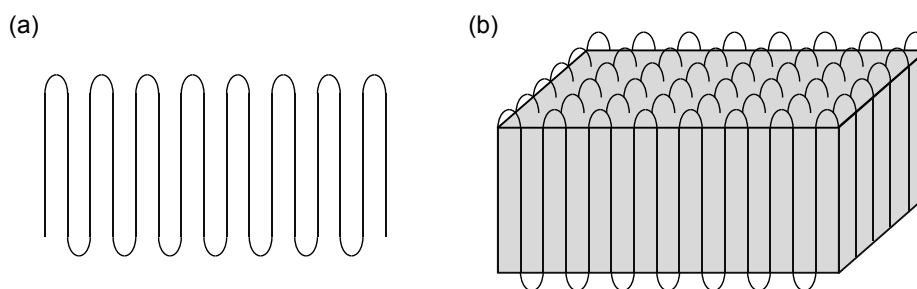


Figure 2.2: (a) Regular tight chain fold of n -alkane, and (b) lamella structure with stacks of tight folded chain arrays.

Due to the high surface energy, a single regular array is not able to exist stably. Thus, either a number of arrays tend to pack themselves together in stack, or the free chains on the array surface continue the folding procedure at the adjacent positions.^[48] Both the above processes enable the arrays to grow in a third dimension, resulting in a layered structure with a certain thickness, as shown in Figure 2.2(b). This structure is conventionally known as a lamella and it is the stem of the crystals in polymer. The direction along the molecular chains in the lamella is normally defined as the ‘ c ’ axis.

The above two spontaneous assembly steps are the fundamental reasons for the formation of the crystalline structure in PE.^[49] In the crystal, the chain segments are well ordered which provide the desirable stiffness and tensile strength for

2 Fundamentals

applications. However, PE consisting of only crystals would be a friable material with poor toughness and impact strength which is mechanically undesirable. As a matter of fact, no pure crystalline PE is naturally available.

2.1.2 Phase Composition

The application value of PE rests on the merit of its mechanical properties which are in turn decided by its intrinsic structure. After more than 50 years intensive study, it is now well accepted that PE is a semicrystalline polymer with three different phases according to the degree of order of the chains.^[50-52] The ordered phase is consisted by lamellae with the chain segments fold in regular arrays which refers as the crystalline phase. The disordered chain segments are normally continuous with those from the crystalline phase and compose the noncrystalline region. In this region, the molecular chains can be classified into two different phases according to their arrangement.

It has been indicated in Figure 2.2 that during the 180° tight fold, parts of the chain segment have to stay out of the lamella before the chains re-enter into the adjacent positions. This phenomenon is the source of the disordered chain arrangement. In fact, adjacent re-entry is not the only manner applicable during the chain packing. As shown in Figure 2.3, the continuing chains from the crystalline phase traverse the lamellae and consist the noncrystalline zones: they (1) connect to an adjacent lamella; (2) fold back to themselves to the original one but not re-enter at the adjacent positions; or (3) terminate as chain ends.^[53,54] These different behavior produces the chain conformations as “ties”, “loops”, and “cilia” in the noncrystalline region, in which the chain segments are more loosely packed. These types of entry are known as random re-entry model or switchboard model.^[55,56] Guttman *et al.*^[57] came to the result that in linear PE about 70% of the folds re-enter to the adjacent or next adjacent positions, while leaving about 30% for the random re-entry or “cilia”. However, in branched PE, due to the relatively stronger steric effect at the branching points, the possibility of 180° re-entry reduces. In fact, branching degree is the major factor that determines the adjacent to random re-entry ratio which, consequently, induces the phase composition differences among different PEs.

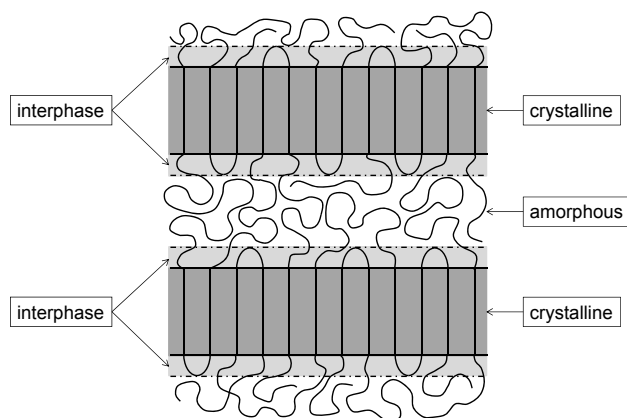


Figure 2.3: Three-component phase model.

When concerning to the degree of disorder, the situations are different depending on the positions of the chain segments and their re-entry types in the noncrystalline region. Figure 2.3 describes a three-component phase model cross-section of PE.^[58] The folded chain segments with the highest degree of order compose the crystalline phase. These chain segments are fixed by the lamella structure with a fully extended conformation. On the other hand, the chains in the noncrystalline region with random re-entries or “cilia” conformations are largely disordered. These chain segments are considered as the amorphous phase with high freedoms on their trajectory and represent a wide range of chain conformations. At the boundary between the crystalline phase and the amorphous phase exists a third phase, which is composed by the chain segments exhibit varying degrees of order as they traverse from the crystalline phase to the amorphous phase. They incorporate two different molecular conformations, one is the tight “loops” by adjacent re-entry, the other is the ends of “cilium” or “tie” that connected with the lamellae. The chains in this region are normally referred as the interphase.

The coexistence of the three phases with different chain conformations and molecular properties, their interaction and connection with each other, makes PE desirably stiff and meanwhile tough for applications. A common way to classify different PEs is according to their densities, as HDPE, medium density PE (MDPE), and low density PE (LDPE). PEs with different densities possess

2 Fundamentals

different proportions of the three phases, the phase composition.¹ Many physical properties of PE such as stiffness, toughness, tensile strength, and impact strength are related to the phase composition. Therefore, in order to understand the mechanical behavior and to tailor the applications of PE, it is essential to characterize the phase composition precisely.

2.2 Polyethylene Molecular Dynamics

The concept of semicrystalline is important which enables to describe PE as a composite of crystalline and noncrystalline² regions (see above). In addition to the different types of chain order, the intrinsic phase differences in the semicrystalline polymers are associated with different molecular dynamics. The molecular dynamic is related to specific chain motions and relaxations which allow classifying the phases by different analytical techniques.

2.2.1 Translation and Rotation in the Crystalline Phase

In the crystalline phase, the chain segments are compactly organized, in which the space in between is little and, thus, restricts the chain mobilities. The chain motions in this region are accomplished by the coordinated movements with other repeat units in the lamella. Figure 2.4 describes the typical molecular motions in the crystalline phase,^[59] in which two different motion categories are exhibited: translation and rotation. The rotation movement, also known as 180° flip, is achieved by a screw rotation of the whole chain segment about the ‘*c*’ axis for 180° flip-flop.^[59] This rotational flip accounts only the initial and final states of the motion with an inherent for- and backward frequency. For a rigid chain, all the repeat units in the lamella rotate simultaneously, thus, the flip energy barrier is proportional to the lamella thickness. However, Fröhlich^[60,61] proposed that due to the high flexibility of *n*-alkane, a twist must develop and move through the crystal during the rotation which involves torsional bond angle distortions. Both

¹Phase composition normally refers to the degree of crystallinity as well as the amount fraction of the interphase and the amorphous phase.

²interphase and amorphous

the rigid and flexible rotations accompany by a half repeat unit shift along the ‘ c ’ axis, and cause one end of the chain segment to translate out of the lamella, as shown on the right of Figure 2.4.

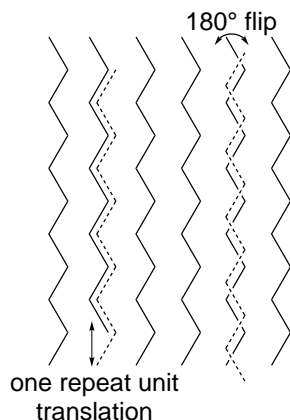


Figure 2.4: Chain translation and rotation in the crystalline phase.

In translation movement, the chain segments in the lamella translate in such a way that the phases of the chain segment before and after the movement are equivalent, while the whole chain segment shifts along the ‘ c ’ axis.^[59] The energy barrier of such movement is also proportional to the number of repeat units involved. Enough energy must be accumulated for the translation of one repeat unit out of the crystallography in a fine lamella structure. In fact, experimental evidence showed that the translation process occurs easily within the disordering of the ‘ c ’ axis when there are imperfections in the lamella,^[62] as shown on the left of Figure 2.4. Both the translation and 180° flip movements are related to the α -relaxation^[63,64] with a narrow relaxation frequency which provides the chain mobilities in and through the crystalline phase.

2.2.2 Crankshaft Motion in the Amorphous Phase

In the amorphous phase, when the temperature is above the glass transition temperature (T_g) of the polymer material, the chain segments are highly flexible thanks to the loose chain packing.^[65] Extra empty space caused by the random chain arrangement, known as free volume (V_f), consists of the holes in the polymer

2 Fundamentals

matrix.^[66,67] When the system has sufficient energy, the movements can lead chain segments to jump into the holes by collaborative bond rotation with several repeat units, but without disturbing the stem polymer chains,^[68] as shown in Figure 2.5.^[69] A series of such motions enables the polymer chains to change their positions completely. These segmental movements in the amorphous phase are known as crankshaft motions.^[70]

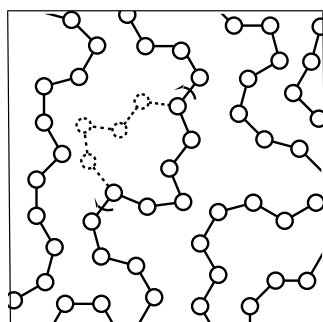


Figure 2.5: Crankshaft motion in the amorphous phase.

Previous investigations indicated that crankshaft motion can be achieved by the coordination of carbon atoms with different successive numbers, ranging from 4 to 6, on the polymer backbone.^[70–72] It is believed that the chain segments involved in this motion are much shorter than in the α -relaxation in the crystalline lamella.^[73] Crissman *et al.*^[74] and Boyd *et al.*^[75] associated γ relaxation with the large scale chain motions in the amorphous phase, which is featured by extremely broad frequencies or time domain. As a matter of fact, the crankshaft motion in this region is assumed as the major candidate for the molecular mechanism of γ relaxation.^[71,76]

2.2.3 Cooperative Motion in the Interphase

The interphase is a transitional phase between the crystalline phase and the amorphous phase, which makes the chain motions in this region more complicated and arbitrary. On one side, the chains continue from the crystalline phase and have at least one of their terminals attaches on the axial cross-section of the lamella,

consistently. Thus, the chain motions are partially constrained by the crystalline structure.^[77] On the other side, the chain segments are also the extensions from the amorphous phase with high flexibility. Furthermore, the segmental mobilities are also decided by the re-entry types as indicated in Section 2.1.2. Therefore, the chain motions in the interphase display a wide range of varieties. In fact, most of the chain segments move cooperatively with the chain motions from either the lamella or the amorphous region. Boyd^[78] and Mandelkern *et al.*^[79,80] demonstrated that the partial constrained interphase molecular motions are related to the β relaxation which proceeds with an intermediate frequency distribution.

2.2.4 Molecular Relaxations

Depending on the molecular circumstances, different relaxation types can be observed in the semicrystalline polymers. Matsuo *et al.*^[81] have investigated the relaxation activation energies of PE with different techniques. The result showed that the activation energy for the α relaxation in the crystalline phase is from 100 kJ/mol to 200 kJ/mol at ambient temperatures. While for the β relaxation in the interphase it is about 100 kJ/mol, and for the γ relaxation in the amorphous phase it is around 20 kJ/mol. In addition, Hronský *et al.*^[82] reported the different relaxation frequencies of PE by a combined dielectric measurement and solid-state NMR study. They demonstrated that the α relaxation frequency in the crystalline phase is about 10^9 MHz and that of the γ relaxation in the amorphous phase is about 10^7 MHz. All these results effectively prove the different chain mobilities in the different phases. It can be summarized that the chains in the crystalline phase are highly confined with low mobility, those in the amorphous phase are highly flexible with high mobility, and for those in the interphase both the chain confinement and mobility stay intermediately.^[64,83,84]

The different relaxation mechanisms in each phase are the fundamentals for the molecular dynamical differences and they also influence the physical performance of PE. Therefore, to understand PE, the relation between physical properties and phase composition, the study and interpretation of chain relaxations are effective. One of the most efficient approaches for this, as demonstrated before, is solid-state NMR. However, in order to understand its abilities for the phase

2 Fundamentals

decomposition and morphological study of semicrystalline polymers, it is essential to explain the basis of the molecular relaxations characterized by solid-state NMR in the first step.

2.3 NMR Molecular Relaxation

All NMR experiments are carried out in a static magnetic field (\mathbf{B}_0). Suppose the spins are in a right-handed three dimensional Cartesian coordinate system. In the case of spins $\frac{1}{2}$, in the ‘ z ’ direction, which is parallel to \mathbf{B}_0 , there are two spin states with different energies. The values of $+\frac{1}{2}$ and $-\frac{1}{2}$ describe the directions of the nuclear moments either aligned with or against \mathbf{B}_0 . The latter state is the one with higher energy, and the distribution of spins between these two states follows the Boltzmann’s distribution law; the difference in energy between the spins $+\frac{1}{2}$ and $-\frac{1}{2}$ is the dominant interaction measured by NMR. At the same time, in the ‘ xy ’ plane which is perpendicular to \mathbf{B}_0 , all the spins precess about \mathbf{B}_0 with a so called Larmor precession frequency. By applying a second rotating magnetic field, designated \mathbf{B}_1 , also known as radiofrequency (rf) field, in the ‘ xy ’ plane, the precessing nuclei can be made to flip. If the \mathbf{B}_1 rotates exactly at the Larmor frequency, the resonance happens. Consequently, the magnetization of the spin changes both along the ‘ z ’ axis and in the ‘ xy ’ plane. One fundamental method of NMR is to detect the spin magnetization recover back to its initial states after the application of \mathbf{B}_1 via either transverse relaxation or longitudinal relaxation.

2.3.1 Transverse Relaxation

Transverse relaxation describes the relaxation of the magnetization in the ‘ xy ’ plane which may involve interactions between different spins. Therefore, it is also known as spin-spin relaxation. Spin-spin interactions induce a variation of local magnetic fields (\mathbf{B}_{loc}) throughout the whole spin system which in turn influences the spin precession. Spins with different precession frequencies tend to get out of the uniform phase and, consequently, the magnetization intensity decreases. In other words, after the rf pulse, the magnetization in the ‘ xy ’ plane decays to zero

2.3 NMR Molecular Relaxation

by spin dephasing with a time constant called transverse (spin-spin) relaxation time T_2 . If \mathbf{B}_{loc} varies greatly throughout the spin system, the significant difference in precession frequencies between spins leads the magnetization to decay faster. $1/T_2$ is used to represent the relaxation rate as:

$$M_{\text{xy}}(t) = M_{\text{xy}}(0) e^{-t/T_2}, \quad (2.1)$$

where M_{xy} is the transverse magnetization, and $M_{\text{xy}}(0)$ is the corresponding signal intensity before the first rf pulse. Normally, T_2 is defined as the time at which the M_{xy} has decayed to 37% of $M_{\text{xy}}(0)$. In transverse relaxation, there is no energy transmission involved.

In polymers, segmental chain motions are the major sources that influence the internuclear interactions, which in turn influence the deviation of \mathbf{B}_{loc} from \mathbf{B}_0 for a specific spin. Depending on the degree of deviation, T_2 of the system changes. Bloembergen^[85] has introduced a calculation model to estimate T_2 in 1948. However, McBrierty *et al.*^[86] assumed that a Gaussian distribution correction would be more appropriate for the solid materials such as semicrystalline polymers. In a system with all spins $\frac{1}{2}$, the T_2 calculation model can be written as:

$$\left(\frac{1}{T_2}\right)^2 = \frac{9}{32} \gamma_g^4 \hbar^2 \sum_k |F_{k_0}|^2, \quad (2.2)$$

where γ_g is the gyromagnetic ratio, \hbar is the Planck's constant over 2π . Statistically, the definition of $F_{k_0} = (3 \cos^2 \theta_k - 1)/r_k^3$ can be applied in solid polymers, where \mathbf{r}_k is the radius vector from spin k to its nuclear neighbors and θ_k is the angle between \mathbf{r}_k and \mathbf{B}_0 .^[87]

In order to understand this model, it is necessarily to first focus on the angle factor $3 \cos^2 \theta_k - 1$. When all angles are available for the internuclear vectors in a three dimensional frame, i.e., $\cos^2 \theta_k = 1/3$, F_{k_0} will then be averaged to zero, which may make T_2 very high; an example of this is seen in the transverse relaxation of liquids. However, in solid polymers the possibility of the angular diversities reduces significantly.

In the crystalline phase, due to the chain confinement and less mobilities, the intermolecular angular diversity between spins is small which causes the chain

2 Fundamentals

segmental behavior in this region to be anisotropic. Thus, the deviation of \mathbf{B}_{loc} from \mathbf{B}_0 is extremely wide, and the relaxation rate in this region is very high with a short T_2 . On the other hand, in the amorphous phase at a temperature higher than T_g , the less chain restriction increases both the chain mobilities and the angular diversities. The isotropic chain behavior in this region reduces the \mathbf{B}_{loc} deviation and, subsequently, reduces the relaxation rate. Therefore, T_2 in the amorphous phase is much longer than in the crystalline phase. In the interphase, both the angular diversities and the chain mobilities stay intermediate. Thus, this region displays an intermediately T_2 between the crystalline phase and the amorphous phase. In typical semicrystalline polymers, T_2 ranges from about $10 \mu\text{s}$ in the crystalline phase to as high as 1 ms in the totally amorphous region.^[87]

2.3.2 Longitudinal Relaxation

Longitudinal relaxation describes the relaxation of the magnetization in the ‘ z ’ direction which involves the energy between spins and their environmental lattices. Therefore, it is also known as spin-lattice relaxation. In spin system, the diverse molecular motions induce alternating \mathbf{B}_{loc} s with a wide range of correlation frequencies. When these frequencies are comparable to the spin resonance frequency in \mathbf{B}_0 , the energy transmits efficiently between the spins and their surrounding lattices. Consequently, the spins are able to flip between different energy levels continuously. After the rf pulse, the magnetization in the ‘ z ’ direction recovers back to its initial state by transmitting the energy from spins $-\frac{1}{2}$ to the lattices with a time constant called longitudinal (spin-lattice) relaxation time T_1 . Longitudinal relaxation is governed by the frequency fluctuations of \mathbf{B}_{loc} that occur close to the spin resonance frequency. $1/T_1$ is used to describe the relaxation rate as:

$$M_z(t) = M_z(0)(1 - e^{-t/T_1}), \quad (2.3)$$

where M_z is the longitudinal magnetization, and $M_z(0)$ is the corresponding signal intensity before the first rf pulse. Normally, T_1 is defined as the time for M_z recovers back to 63% of its original intensity after the rf pulse.

In polymers, the diversified chain motions cause the frequency fluctuations to differ from phase to phase. Based on this the morphological information can

be obtained by NMR T_1 measurement. By modifying Bloembergen's calculation method, McBrierty *et al.* introduced the estimation model of T_1 for semicrystalline polymers with the similar approach as described for T_2 .^[85,86] For a spin $\frac{1}{2}$ system, it can be written as:

$$\frac{1}{T_1} = \frac{9}{8} \frac{\gamma_g^4 \hbar^2}{\omega_0} \left(\frac{2\chi_0}{1 + \chi_0^2} \sum_k |F_{k_1}|^2 + \frac{2\chi_0}{1 + 4\chi_0^2} \sum_k |F_{k_2}|^2 \right), \quad (2.4)$$

where ω_0 is the Larmor frequency of the spins in \mathbf{B}_0 ; $\chi_0 = \omega_0 \tau_c$, τ_c is the molecular correlation time which is reciprocally related to the molecular relaxation frequencies; F_{k_1} and F_{k_2} are the lattice functions which are proportional to the relaxation frequency distribution.^[88]

In the T_1 calculation, only the time dependent part of the function is relevant. According to Equation 2.4, the value of T_1 reaches the minimum when the relaxation distribution is very wide and, at the same time, $\chi_0 \simeq 0.5$ to 1. The current typical proton spin precession frequencies in NMR range from 10^7 Hz to as high as 10^9 Hz. It is already known that the molecular relaxation frequencies of PE also range from 10^7 Hz in the amorphous phase to 10^9 Hz in the crystalline phase.^[82] Therefore, the correlation between the spin precession frequencies and the molecular motions is comparable in all phases. However, due to the extremely wide molecular relaxation frequency distribution in the amorphous phase, the energy transmission efficiency in this region is higher. Thus, T_1 in the amorphous phase is normally shorter than in the crystalline phase in the NMR spectroscopically applicable temperature range. McCall^[87] mentioned that experimental T_1 values determined by NMR for polymers are usually higher than the theoretically estimated values. This can be explained by the relaxations in which only the chain segments engage in the motions have to transfer the magnetization along the entire chain through spin-diffusion.

2.4 NMR Experimental Methods

The bases of NMR for materials studies are the molecular information extracted from the NMR signal after the rf pulse. By applying different pulse sequences

2 Fundamentals

different information can be obtained. In solid polymer study, certain specific characteristics of the spectrometer hardwares are required to generate precise pulses as well as to record accurate signals.

2.4.1 NMR Equipments

The resolution and sensitivity of NMR spectrometers have been significantly improved during the last several decades. Nowadays, spectrometers with a wide range of resonance frequencies from 1 MHz to 1000 MHz are available. Besides, in addition to the conventional homogeneous high-field NMR, the development of the open magnet geometries has led to the booming of the applications of the low-field single-sided NMR to various areas.^[89] All these progresses make NMR a more and more attractive and convenient technology for material characterization and research.

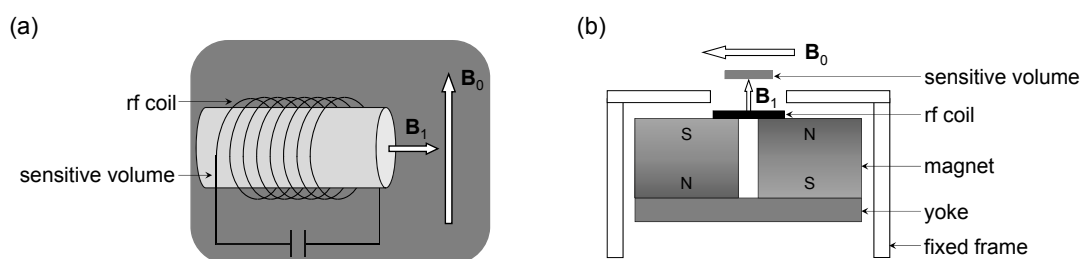


Figure 2.6: Principal schematic sensor of (a) high-field NMR and (b) unilateral low-field NMR-MOUSE.

Figure 2.6(a) shows the principal schematic sensor of high-field NMR,^[90] in which B_0 is normally generated by superconducting magnets. The rf coil is double functioned: (1) as a transmitter to generate the B_1 , and (2) as a receiver to record the signal after the rf pulse. The sensitive volume is inside the rf coil. Due to the fast molecular relaxation of semicrystalline polymers such as PE, several essential requirements on the solid-state spectrometer which are more stringent than its liquid-state counterpart must be met.^[91] First, the pulse programmer must be able to produce short duration pulses of microseconds or even less with a width and stabilities that are controlled with deviations of less than 1%. Second, a

fast analogue-to-digital converter is indispensable. It allows to apply a as short as possible dwell time to capture enough points of the FID after the rf pulse. Third, a sensitive signal receiver with a extremely short instrumental dead time is desirable to record sufficient signals at the beginning of the FIDs.

Figure 2.6(b) shows the digram of a NMR-MOUSE[®] (NMR mobile universal surface explorer),^[89,92,93] in which \mathbf{B}_0 is generated by arrays of permanent magnets with a field intensity ranging from 0.1~1 T. Due to the open and single-sided magnet arrangement, \mathbf{B}_0 in this system is inhomogeneous with a magnetic gradient up to 20 T/m.^[94-96] The surface rf coil is placed on the top of the magnet arrays and plays the same functions as in the high-field NMR. The sensitive volume is over the rf coil within certain specific distance. Recently, NMR-MOUSE acquired a more and more important role in the NMR technology. The advantages of open sensor as well as small volume and weight make it advisable to investigate the objects out of the NMR laboratory in a noninvasive manner. Furthermore, with the incorporation of the digital lift, the profile NMR-MOUSE is able to sweep the detailed profile information of the testing specimens on a microscopic scale within its sensitive range.^[97]

2.4.2 Pulse Sequences

In previous section, two different relaxation processes as transverse and longitudinal relaxations in NMR have been described. The pulse sequences used to study these two relaxation processes are different. The simplest way to observe the transverse relaxation is the FID measured after a single 90° pulse in the high-field NMR, as described in Figure 2.7(a). When the signals are detected under homogeneous \mathbf{B}_0 , T_2 of liquids can be simply obtained by fitting the FIDs with the exponential function in Equation 2.1. However, for semicrystalline polymers, due to the complexity of the spin couplings, modification of the normal exponential decay function is necessary. Besides, multicomponent function is essential for the spin systems with different relaxation behavior, and based on the signal intensities of each component, the phase composition is extractable. However, due to the instrumental dead time, the fitting distortion due to the loss of initial signals has to be taken into consideration.

2 Fundamentals

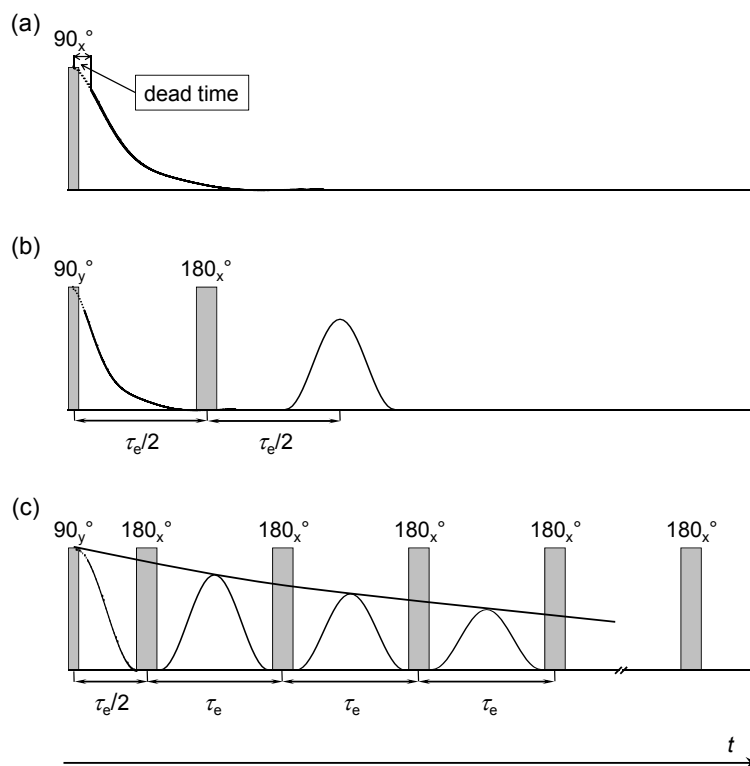


Figure 2.7: Pulse sequences for transverse relaxation measurement: (a) single 90° pulse, (b) Hahn echo, and (c) CPMG. $\tau_e/2$ is time interval between 90° pulse and 180° pulse in the spin echo pulse sequences, and τ_e is known as echo time.

Hahn and CPMG pulse sequences, which are known as spin echo methods, are also widely used to investigate the proton transverse relaxations. In fact, these sequences are more popular as they can diminish the dephasing effect caused by the inhomogeneity of the \mathbf{B}_0 and, thus, to extract the intrinsic T_2 of the specimens. Figure 2.7(b) presents the Hahn echo pulse sequence. After the 90° excitation pulse, the transverse magnetization starts to decay with time. If a 180° pulse is applied along an axis in the “ xy ” plane at time $\tau_e/2$, the magnetization is able to refocus and the signal reaches to the maximum with a same period of $\tau_e/2$ after the 180° pulse. This refocused signal is known as an echo. With the Hahn echo pulse sequence, the decaying signal is acquired by applying a list of varying τ_e s. The fundamentals of the CPMG pulse sequence are the same as those of Hahn pulse sequence, the only difference is instead of applying different τ_e s between

the pulses, it fixes τ_e and applies a number of 180° pulses to record the echoes between them, as shown in Figure 2.7(c). The shortest possible τ_e is decided by the instrumental dead time, the 90° pulses length, as well as the acquisition time. In fact the relative long τ_e also leads to severe signal loss at the beginning of the decays, especially in CPMG pulse sequence.

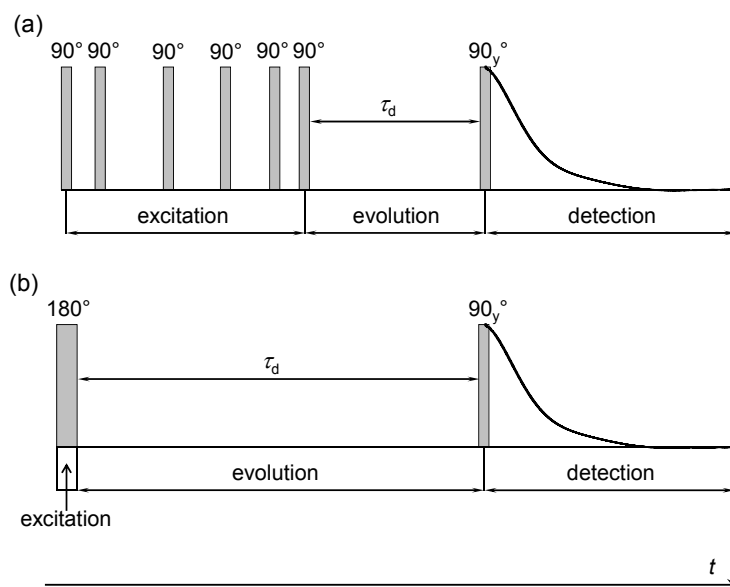


Figure 2.8: Pulse sequences for longitudinal relaxation measurement: (a) saturation recovery pulse sequence and (b) inversion recovery pulse sequence.

There are two different pulse sequences available to observe the longitudinal relaxation, saturation recovery and inversion recovery pulse sequences, as shown in Figure 2.8. The basic construction of these two pulse sequences is the same, which can be resolved into excitation, evolution, and detection parts. The main difference between them is the excitation mechanism which can be also read from their names. In the saturation recovery pulse sequence, before the evolution time, a series of 90° pulses with arbitrary phases is applied to excite the spins and to suppress the global magnetization on the ‘ z ’ axis. On the other hand, in the inversion recovery pulse sequence, a 180° pulse is used to excite the spins and to lead the magnetization on the ‘ z ’ direction to flip to the minus direction. After the excitation period, a delay time τ_d is applied in both cases to investigate the

2 Fundamentals

recovering of the magnetization back to its thermodynamic equilibrium state and, thus, to evaluate the spin longitudinal relaxation. After τ_d with the application of the 90° pulses the recovered magnetization intensities can be detected. In both sequences a varying list of τ_d is applied to build up the recovery curves. T_1 can be obtained by fitting the recovery curves with the exponential function as Equation 2.3. In general, the phase resolution of longitudinal relaxation methods is not as good as that of the transverse relaxation methods in solid polymer studies. However, morphological information can be still estimated based on the differences in T_1 .

In addition to the basic relaxation pulse sequences, today, more advanced NMR methods are available for the modern characterization of polymer materials, for instance, the high resolution solid-state NMR spectroscopy, multidimensional NMR, etc.^[14,22,98–102] In particular, as demonstrated in Chapter 1, the abilities of double-quantum NMR to observe the intra- and/or intermolecular nuclear interactions between protons as well as those of spin-diffusion NMR to detect the magnetization diffusion processes are the most widely applied. Both of them provide more detailed information which helps to understand the materials better. They will be introduced and applied separately under certain specific molecular conditions in the following chapters.

3

Correlation of DSC and Solid-State NMR in a PE Study

The degree of crystallinity is without doubt the most widely discussed issue in both investigation and application of PE. Nowadays, different analytical methods such as XRD,^[103,104] IR,^[105] DSC,^[106,107] and solid-state NMR^[42,108] are able to characterize the crystallinity of semicrystalline polymers. Different assumptions based on either the long range order, optical transmittance, enthalpy latent, or molecular motions have to be taken so as to apply these methods to describe the morphological complexity of PE.^[104] However, they will lead to controversy results. Besides, two-component crystalline-amorphous phase model is widely used to simplify the description of semicrystalline polymers, such as the crystallinity determined by DSC. This causes the description of the well accepted third phase, the interphase, a problem. All these issues make the correlation of the phase compositions determined by different methods necessary.

In the current study, phase compositions of different PEs characterized by DSC as well as high- and low-field solid-state NMR were compared. The melting behavior and the NMR molecular relaxations of the samples were also studied. At the same time, the application potential of the NMR-MOUSE to semicrystalline polymer was evaluated by comparison with high-field NMR. The morphological and molecular dynamical gradients of HDPE pipes caused by different processing parameters were monitored by the NMR-MOUSE in a nondestructive manner.

3.1 Materials

A series of PE samples with different crystallinities were either purchased from Aldrich-Sigma or kindly donated by research collaborators. All of them are non-crosslinked, however, their structures as molecular weight, branching degree, and branching length is various. The samples were studied as received.

3.2 Characterization by DSC

DSC is a classical and widely used technique on polymer science. Based on the latent heat as well as the melting behavior, DSC is able to elucidate the glass transition, crystallization kinetics, and crystallization thermodynamics of polymers. For the fundamental principles and applications previous work as well as references there are recommended. ^[109,110]

3.2.1 DSC Measurement

A NETZSCH DSC 204 apparatus was applied to investigate the melting behavior and crystallinity of PE samples. The DSC temperature scans were carried out between room temperature and 180 °C with both heating and cooling rates of 10 °C/min. A nitrogen gas flow rate of 20 cm³/min was applied to create the inert atmosphere so as to avoid the oxidation or decomposition reactions.

3.2.2 Crystallinity and Melting Behavior

Figure 3.1 depicts a typical DSC scan of PE, in which the heating and cooling traces are labeled as endothermic and exothermic processes, respectively. There are three important parameters which can be characterized by DSC: (1) the melting temperature (T_m) which is defined as the peak of heating traces, (2) the crystallization temperature (T_c) which is defined as the peak of the cooling traces, and (3) the crystallinity (w_c) which is derived from the melting enthalpy (Δh_m) by integrating the area under the heating traces as the shaded pattern shown in the figure. In this study, the specific melting enthalpy of $\Delta h_m^0 = 293 \text{ J/g}$ for ideal 100% PE crystals was used to calculate w_c . ^[111,112]

3.2 Characterization by DSC

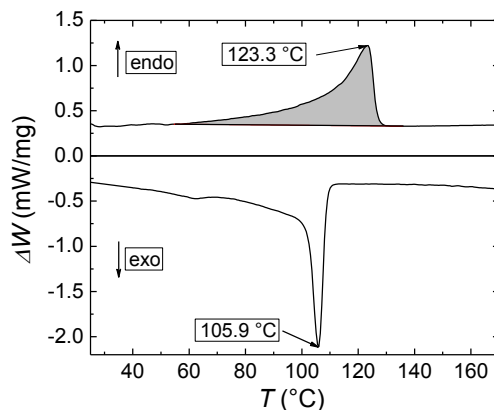


Figure 3.1: DSC traces of PE.

Table 3.1: Crystallinity, melting temperature, and crystallization temperature of PE determined by DSC.

Samples	T_c °C	T_m °C	w_c %
1	105.9	123.3	33.4
2	105.5	124.2	37.4
3	98.7	114.6	41.5
4	112.9	130.4	56.0
5	114.4	134.0	65.3
6	119.1	143.4	70.3

In order to have the result comparable between DSC and NMR, uniform thermal history of the samples is essential. However, DSC measurements involve heating and temperature encoding, by which the thermal history is changed after the first scan. Therefore, in this study, only the first heating and cooling traces were used to identify T_c , T_m , and w_c for all samples.^[113] Table 3.1 shows the results, in which the samples are sorted and numbered from 1 to 6 according to w_c . Both T_c and T_m increase with w_c , except for the third sample which has the lowest values. This indicates, basically, the crystal size changes in accordance

with w_c , and their molecular structure differences do not influence the melting behavior apparently.

3.3 Characterization by High-Field ^1H FID

Due to the various benefits of ^1H FID measurements, in the last decade, intensive investigations have been carried out on its applications to semicrystalline polymers.^[38,42,83,114] To name just a few of its advantages, first thanks to the fast longitudinal relaxation and high natural abundance of ^1H , it is effectively time saving. One FID measurement normally takes only 2~10 min including signal averaging. Second, FID is the most accurate NMR transverse relaxation signal for the crystalline phase in semicrystalline materials, as the extremely short dwell time promises to record the initial signals of the fast decays as many as possible. Third, well established fitting models are available for the data interpretation which guarantees the extracted morphological and molecular dynamical information accurate.

However, there are still remaining issues need to be taken into consideration, in which the most obvious one is caused by the instrumental intrinsic dead time (t_d) before the acquisition opening. It causes a significant signal loss in the crystalline phase due to its high relaxation rate. The influence of the inherent signal blank at the beginning of FIDs on the accuracy of the data interpretation has been realized since decades. One common way to compensate this drawback is to generate the lost signal at the beginning of FIDs. Engelsberg and Lowe^[115] used the zero-time-resolution technique^[116] to rebuild the lost signal. This method can well rebuild the blank signal, however, it must be performed at the expense of the time saving advantage of standard FID measurements. Litvinov *et al.*^[113] demonstrated that one can apply the solid echo and, by extrapolating the signals recorded with different echo times, establish the signal point at time zero. Hansen *et al.*^[42] estimated the zero time signal by measuring the melted samples. Liquids exhibit longer relaxation times which allow them to ignore the relatively small fraction of signal loss during t_d . Both the above methods can only generate one data point at zero time which can partially compensate for fit errors caused

3.3 Characterization by High-Field ^1H FID

by the missing signal at the beginning of the decays. However, the addition of only one more point at the beginning of FID can contribute only a very limited improvement of the fit. In the current work, the influence of t_d on the FID fit quality was evaluated. The fit was performed on the FIDs without reconstruction of the initial signals, and the influence of the fit extrapolation on the result of the phase composition was evaluated without any fit coordination control at the signal blank region (initial region) of the FIDs.

3.3.1 ^1H FID Measurement

^1H static FID measurements after the single 90° pulse¹ were performed on a 700 MHz Bruker NMR spectrometer. A high power magic angle spinning (MAS) probe body with a 3.2 mm coil was applied and the optimized 90° rf pulse was $2\ \mu\text{s}$. The FIDs were recorded with a dwell time of $0.1\ \mu\text{s}$, and the number of scans was 32 with a recycle delay of 5 s. A series of measurements with different t_d from $5\ \mu\text{s}$ to $10\ \mu\text{s}$ was performed with a time increment of $1\ \mu\text{s}$ between each step. All measurements were carried out at room temperature.

3.3.2 Model Fit

Pake^[117] has deduced an expression to describe the relaxation of the crystalline phase represented by ^1H broad line spectrum of a spin $\frac{1}{2}$ system. However, in order to apply this model to the FID, an inverse Fourier transformation is indispensable. Look *et al.*^[118] solved this problem by applying Fresnel function with the definition of the integral functions. Besides, Brereton^[119] introduced a precise analytical function which is able to describe the decays of the noncrystalline phase with a single relaxation time. Therefore, by combining Look's function and several Brereton's functions, the relaxation behavior of semicrystalline polymers can be described. However, due to the complexity of these two functions with too many fit coefficients, the data analysis is not a trivial task, and fit errors can easily occur.^[38] Instead, Dadayli *et al.*^[12] introduced a more simplified model by combining an Abragam function,^[120] a stretched exponential decay function,^[121]

¹For pulse sequence, please see Figure 2.7(a).

3 Correlation of DSC and Solid-State NMR in a PE Study

and several exponential decay functions to describe the decays of the crystalline phase, the interphase, and the amorphous phase, respectively.¹ In the current situation, a three-component fit model is applied to meet the phase model that has been described in Section 2.1.2. The fit function is:

$$I(t) = I(0)^c \exp \left[-\frac{1}{2} \left(\frac{t}{T_2^c} \right)^2 \right] \frac{\sin(2\pi\phi t)}{2\pi\phi t} + I(0)^i \exp \left[-\left(\frac{t}{T_2^i} \right)^\kappa \right] + I(0)^a \exp \left(-\frac{t}{T_2^a} \right), \quad (3.1)$$

where t is the time domain; I is the signal intensity in arbitrary units, in which the superscripts c , i , and a represent the crystalline phase, the interphase, and the amorphous phase, respectively; ϕ is the sinusoidal oscillation constant; κ is the exponent of the stretched exponential decay function which depending on the phase softness changes between 1 (pure exponential decay) and 2 (pure Gaussian decay). Phase composition is deduced by the signal intensity of each phase obtained at zero time, for instance, crystallinity can be calculated by: $w_c = I(0)^c / [I(0)^c + I(0)^i + I(0)^a]$. Previous work has proved that softness of the interphase is irrelevant to the crystallinity, and only the corresponding signal intensities change from one sample to another.^[42] Therefore, partially constrained model fit of κ being fixed to 1.5 was applied for all samples in this study.

Figure 3.2 shows the FID fit results and the fit residuals. Zero time is defined as the center of the rf pulse. The benefit of FID fit over the broad line deconvolution is its automatic extrapolation of the signal back to zero time and, thus, to compensate the signal loss induced by t_d . The initial fit result in the short time domain² built by the fit model reaches a plateau at $t_d = 0.1 \mu\text{s}$, based on which the signal lost between 0 and $6.8 \mu\text{s}$ ³ of about 25% can be calculated. This signal loss is mainly from the crystalline phase, as presented by the decays

¹This is the current most widely applied model for the fit of FIDs recorded from the semicrystalline polymers. There are also other models available, some of them have been investigated and discussed in previous work,^[38] and the result showed that there are differences between the phase compositions achieved by different models. However, the influence of different fit models on T_2 has, up to now, not been discussed.

²The time domain NMR is not able to record the signal due to t_d .

³The first valid signal point is recorded at $6.8 \mu\text{s}$ in this study.

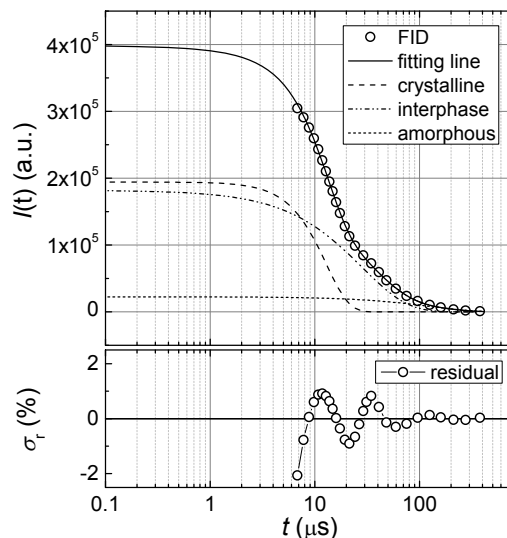


Figure 3.2: ^1H FID of PE measured on high-field NMR and the fitting results with the indication of fitting residuals. The decomposed three components are presented with different line styles.

of the decomposed sublimes.¹ Due to the beat profile of the FID between $20\ \mu\text{s}$ and $30\ \mu\text{s}$, the fit residual (σ_r) acts as a damped oscillation at the time domain from $6.8\ \mu\text{s}$ to $90\ \mu\text{s}$. This behavior was first observed in inorganic crystals and is able to describe the ^1H dipolar couplings. The beat profile has been frequently discussed in PE studies over the last decades,^[122–125] and it is also the reason for the implant of the sinusoidal term in the Abragam function. However, the side effect is the oscillation manner, the function generates the deviation of the fit result from the true values at the beginning of FIDs. This induces distortions when extrapolating the fit line to zero time, and may lead to fitting errors.

3.3.3 Dead Time Dependence

According to the current observation, σ_r s at the beginning of the FIDs that recorded with different t_{d} s are consistently negative, and the absolute values get higher when the signal approaches the first valid point. If this observation is common to all fits, the value of t_{d} will then influence the total deviation of the

¹Crystalline phase decays the fastest, thus, leads to the most significant signal loss.

3 Correlation of DSC and Solid-State NMR in a PE Study

extrapolation. Hence, it is necessary to evaluate the fit distortions with different t_{dS} . Figure 3.3 shows the FIDs recorded with different t_{dS} which are presented in a semilogarithmic scale. The decays at long time domain are identical, the only difference between them is the cut of the signal at the initial regions.

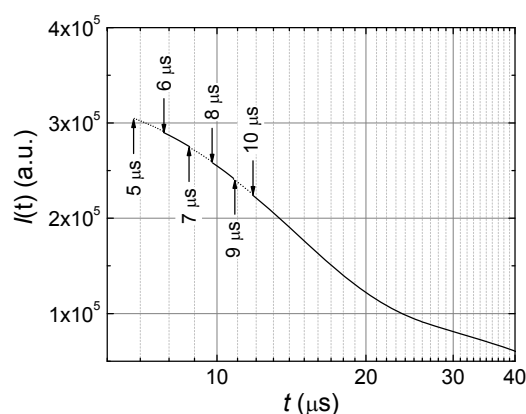


Figure 3.3: ^1H FID of PE recorded with different dead times.

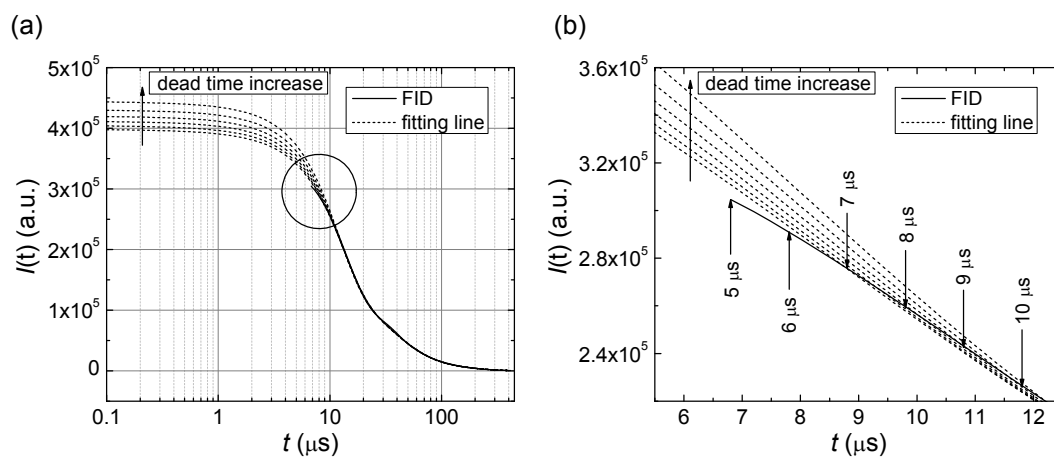


Figure 3.4: Fit of PE ^1H FIDs, in which from bottom to top the dashed lines present the fit results of FIDs with a dead time from $5\ \mu\text{s}$ to $10\ \mu\text{s}$: (a) whole time domain, (b) magnified display of the circled region in Figure (a).

Figure 3.4 shows the fit results. In Figure 3.4(a), the extrapolated signals at the signal blank region increase with increasing t_d . Besides, all the fitted

3.3 Characterization by High-Field ^1H FID

values are higher than the first signal point at $6.8 \mu\text{s}$ that is measured with $t_d = 5 \mu\text{s}$. Therefore, the extrapolated values at time less than $6.8 \mu\text{s}$ deviate to higher values than the real data, as no true signal points are available to constrain the fit. This indicates the increasing t_d causes the fit distortion to be more severe. Figure 3.4(b) is a zoomed display of the fits in the initial region of the FIDs. The fitting program only controls the deviations of less than 2% at the first valid data point for each FID. However, for the FID recorded with $t_d = 10 \mu\text{s}$, the deviation increases to more than 10% compared to the real signal recorded at $6.8 \mu\text{s}$ with $t_d = 5 \mu\text{s}$. Thus, by extrapolating the signal to zero time in this case ($t_d = 10 \mu\text{s}$), the deviation becomes very strong, which will definitely lead to calculated phase compositions different from the true values.

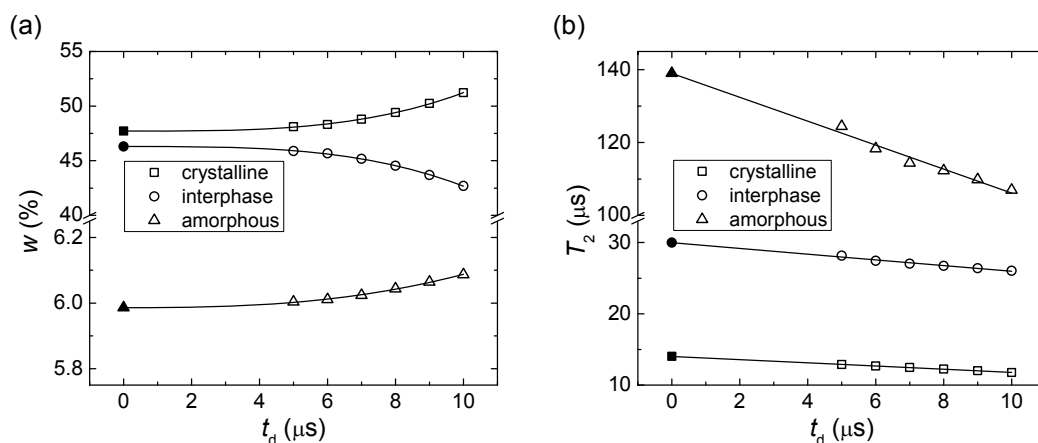


Figure 3.5: Dead time dependence of ^1H FID fit results: (a) phase composition and (b) transverse relaxation times.

Figure 3.5 shows the t_d dependent fit results. Both phase composition and T_2 are influenced, in which the amounts of the crystalline phase and the amorphous phase increase with t_d , while that of the interphase decreases. T_2 s from different phases act in a more consistent way that all of them decrease with t_d , and T_2^a is affected most remarkably. By extrapolating the dependence to $t_d = 0$,¹ it is

¹Due to the lack of supporting theory, the extrapolation of the results was performed according to the manner of t_d dependence. The phase composition was extrapolated by power law function and the T_2 s were extrapolated linearly.

3 Correlation of DSC and Solid-State NMR in a PE Study

able to extract the true values for phase composition and T_2 , as indicated by the solid symbols in the figures. The results illustrate that the t_d influence on phase composition is not obvious when t_d is lower than $6 \mu s$, as plateaus can be observed for all phases by then. On the other hand, T_2 s from different phases are all linearly dependent to t_d . The changes of T_2^c and T_2^i with t_d are weak, however, for T_2^a it is quite strong. An as high as 10% deviation of the extrapolated T_2^a from that of determined by the FID recorded with $t_d = 5 \mu s$ can be observed.

3.3.4 Phase Composition and Relaxation Times – I

Table 3.2 shows the phase composition and T_2 s determined by high-field 1H FID. All the values are obtained with the extrapolation of t_d to zero. w_c changes in the same way as observed by DSC, while the fraction of interphase (w_i) decreases with increasing w_c . The fraction of amorphous phase (w_a) behaves differently, when w_c is less than 60%, the detected w_a are uniformly around 6.0%, while when w_c is more than 70%, the amorphous phase is not detectable. Besides, T_2 seems not to be subject to obvious change with increasing w_c in all phases. T_2^c , T_2^i , and T_2^a are around $13.5 \mu s$, $28.0 \mu s$, and $138.0 \mu s$, respectively.¹

Table 3.2: Phase composition and transverse relaxation times of PE determined by high-field 1H FID.

Samples	w_c %	w_i %	w_a %	T_2^c μs	T_2^i μs	T_2^a μs
1	47.7	46.3	6.0	14.0	30.0	139.0
2	50.6	43.6	5.9	13.6	30.0	133.4
3	54.3	39.8	6.0	13.9	27.7	145.8
4	71.6	28.4	0	13.3	31.1	–
5	79.4	20.6	0	12.9	25.5	–
6	86.1	13.9	0	13.0	27.4	–

¹ T_2^a s of the samples with w_c higher than 70% are not available, as the amorphous phase is not observable for them. Due to the strong chain confinement caused by the high crystallinity, the relaxation of the amorphous phase is not detectable.

3.4 Characterization by NMR-MOUSE

Although there are many advantages for conventional high-field NMR, its applications are still hampered somewhat due to the fact that the sample dimensions have to be small enough to fit into a big and heavy magnet installed in dedicated laboratories. Besides, the spectrometers are also expensive.^[126] On the other side, the NMR-MOUSE is far less expensive, portable, and does not impose restrictions neither on the sizes of the object nor the places of the measurement. However, because of the relatively longer instrumental intrinsic dead time, its applications to semicrystalline polymers are still not wide, and up to now few relevant publications are available on this subject.^[127–130] Therefore, it is important and worthwhile to further evaluate the application of NMR-MOUSE to the characterization of semicrystalline polymers, and to prove its validation in this field with samples in a wide range of crystallinities.

3.4.1 NMR-MOUSE Relaxation Measurement

A profile NMR-MOUSE with 20.6 MHz ^1H resonance frequency was applied to study the relaxations of PE. The magnet used to generate the sensitive volume is similar to that presented in Figure 2.6(b), in which four permanent magnets with specific polarization directions were placed and fixed on the top of a yoke. The digital lift enables to sweep the sample voxels in the sensitive range.^[97]

A 90° – 90° solid echo train was applied to record the ^1H transverse relaxation of PE. It is similar to the CPMG pulse sequence as described in Figure 2.7(c). Instead of 180° pulses after the first 90° pulse, all the pulses in the solid echo chain are 90° pulses. Besides, the phase of the first rf pulse differs by 90° from those of the rest pulses in the pulse sequence.^[11] The optimized $2.2\ \mu\text{s}$ 90° rf pulses with the shortest available echo time of $21.8\ \mu\text{s}$ were used, and the echo numbers were 600. All the samples were repeated for three times and the number of scans for each were 1024 with a recycle delay of 2 s. Besides, in order to get rid of the heating effect caused by the high power rf pulses, an air cooling system was applied. A saturation recovery pulse sequence, which is similar to that presented in Figure 2.8(a), was used to evaluate the ^1H longitudinal relaxation. In stead of

3 Correlation of DSC and Solid-State NMR in a PE Study

record the whole decays as on the high-field NMR, in our case, another 90° pulse was applied to acquire the echoes on the NMR-MOUSE for signal acquisition by the rf coil. The recycle delay for this measurement was 1 s and other parameters and setups were all the same as those for the solid echo train measurement.

3.4.2 Data Interpretation

The relaxation decays recorded by the solid echo train can be well described by multicomponent exponential decay functions as Equation 2.1. This is also applicable for semicrystalline polymers.^[127] In this work, a three-component fit model was used to meet the established phase model.

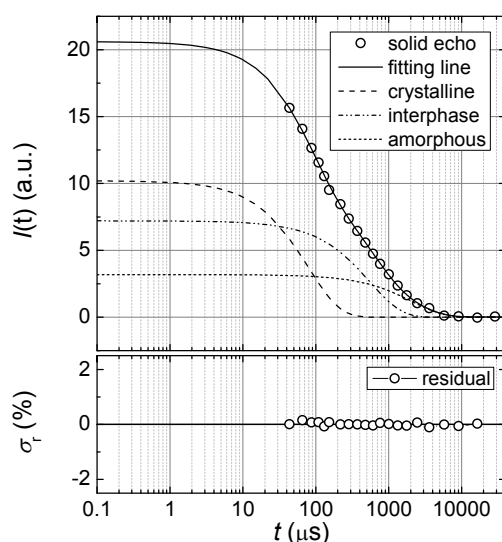


Figure 3.6: ^1H solid echo decay of PE measured with the NMR-MOUSE and the fit results with the indication of fit residuals. The decomposed three components are presented with different line styles.

Figure 3.6 is the fit result, in which the first valid data point was recorded at $43.6 \mu\text{s}^1$ after the application of the first 90° pulse. By extrapolating the fit curve to $1 \mu\text{s}$ the signal plateau is observed. The signal lost due to the dead time effect at the initial region of the decay is around 25% which is at the same level

¹Due to the over lowed signal intensity induced by the inhomogeneity of \mathbf{B}_0 , all the first echoes did not use for the data interpretations.

as that has been observed by high-field ^1H FID. However, there is no oscillation behavior observed in the fit residual which indicates the distortion induced by the fit extrapolation can be ignored. The phase composition can be calculated in the same way as indicated in Section 3.3.2.

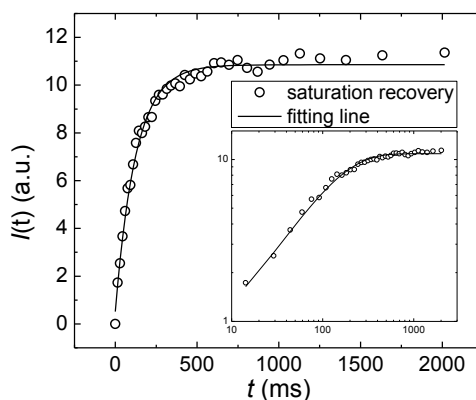


Figure 3.7: ^1H longitudinal relaxation recovery of PE measured with the NMR-MOUSE and the fit result. The inserted figure shows the results on a double-logarithmic scale.

The longitudinal recovery can be only fitted with one-component model as Equation 2.3. The obtained T_1 is able to correlate with the morphology. Figure 3.7 shows the fit result with the inserted display in a double-logarithmic scale. The signal suffers strong fluctuation due to the low signal to noise ratio, however, the fit line still meets with the data points well.

3.4.3 Effective Transverse Relaxation Time

The transverse relaxation rates detected by high-field NMR and NMR-MOUSE are different, as shown in Figure 3.2 and Figure 3.6. The time domain recorded by NMR-MOUSE is 100 times longer than that recorded by the high-field NMR, which indicates a much lower relaxation rate. This phenomenon was first investigated by Ostroff and Waugh,^[131] and the applied solid echo train versus double solid echo train is also known as OW4 pulse sequence.^[132] The over lowed relaxation rate, in this case, is caused by the inhomogeneity of the magnetic field of the NMR-MOUSE. The significant field gradient leads to a strong space modulation

3 Correlation of DSC and Solid-State NMR in a PE Study

of \mathbf{B}_0 and \mathbf{B}_1 , consequently, causes a spin flip angle distribution between different voxels within the sensitive volume.^[133,134] The subsequent spin-lock effects^[131] influence the signal decay, in which a mixture of transverse and longitudinal relaxations can be detected simultaneously. Therefore, the relaxation time determined by solid echo train on the NMR-MOUSE is not pure T_2 , but rather a combination of T_2 and the longitudinal relaxation time in rotating frame, $T_{1\rho}$. This specific relaxation time is conventionally referred as $T_{2\text{eff}}$, and it is echo time dependent.

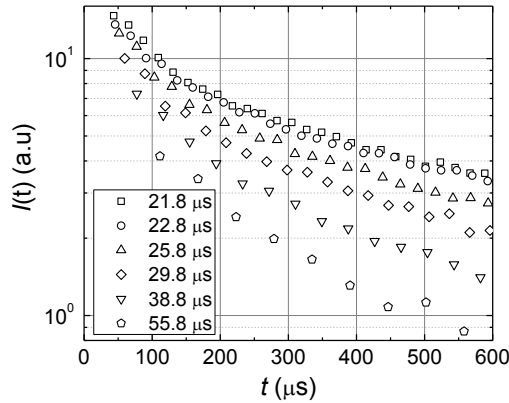


Figure 3.8: Initial echoes of the decays with different echo times recorded by NMR-MOUSE.

By placing the specimens in a homogeneous \mathbf{B}_0 in the presence of a large static gradient, Bain *et al.*^[135] have calculated the remaining spin echo signals in the ‘ xy ’ plane with increasing echo numbers. They deduced the contribution of the transverse relaxation on each specific echo in the decay and, at the same time, described the effect of longitudinal relaxation induced by the gradient. By describing the time and space dependent \mathbf{B}_{loc} of an inhomogeneous NMR open sensor, Hürlimann *et al.*^[136] introduced a simplified expression to describe the relaxation rate at the initial part of the decays recorded by CPMG pulse sequence for the liquids as:

$$\frac{1}{T_{2\text{eff}}} = \frac{1}{T_2} - \psi \left(\frac{1}{T_2} - \frac{1}{T_{1\rho}} \right), \quad (3.2)$$

where $0 \leq \psi \leq 1$ is related to the direction of \mathbf{B}_{loc} in each echo. This equation illustrates the decreasing of the detected transverse relaxation rate due to spin-

lock effects. It is also applicable for the solid samples measured by the solid echo train. However, the calculation of ψ is different. Figure 3.8 shows the initial part of the decays measured with different τ_e , in which by increasing τ_e the signal deteriorates faster. This indicates the spin-lock effect gets weaker with the increasing τ_e , which makes the T_2 contribution higher. Figure 3.9 is a comparison between the decays with and without spin-lock effect. The “□” symbolized decay is built by taking the second echo recorded with different echo times, in which the spin-lock effect gets weaker with time, as longer τ_e s were applied for the signal acquisition at the long time domain. The relaxation rate difference between the normal solid echo decay and the built up second echo with different τ_e s is clear, in which the time domain shift is about 100 times. The decay built by the second echoes behaves similar as ^1H FID recorded by high-field NMR. However, due to the severe signal loss of more than 65% at the initial part, the dead time effect will definitely lead to the fit result be unreliable. In fact, the spin-lock effect, the higher $T_{2\text{eff}}$ than T_2 , is the main reason which makes the NMR-MOUSE applicable for semicrystalline polymers with the solid echo train method.

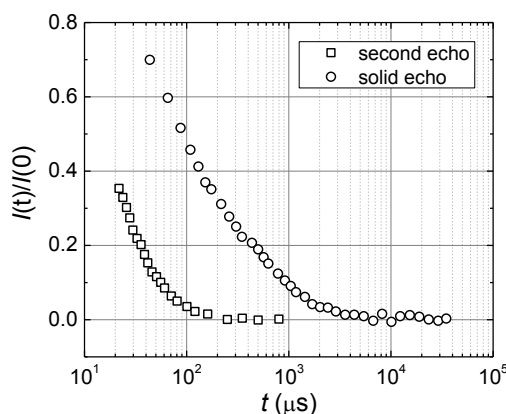


Figure 3.9: Solid echo decay and the second echo of the decays with different echo times recorded by NMR-MOUSE.

3.4.4 Phase Composition and Relaxation Times – II

Table 3.3 shows the phase composition, $T_{2\text{eff}}$, and T_1 determined by NMR-MOUSE, in which w_c changes the same as observed by DSC, and w_i changes the same as

3 Correlation of DSC and Solid-State NMR in a PE Study

observed by high-field ^1H FID. The amorphous phase is observable for all samples by NMR-MOUSE and the values of w_a are around 10%. $T_{2\text{eff}}$ seem not to change with w_c either, the detected $T_{2\text{eff}}^c$, $T_{2\text{eff}}^i$, and $T_{2\text{eff}}^a$ are around 80 μs , 600 μs , and 2500 μs , respectively. However, T_1 increases with increasing w_c significantly.

Table 3.3: Phase composition, effective transverse relaxation times, and longitudinal relaxation time of PE determined by NMR-MOUSE.

Samples	w_c %	w_i %	w_a %	$T_{2\text{eff}}^c$ μs	$T_{2\text{eff}}^i$ μs	$T_{2\text{eff}}^a$ μs	T_1 ms
1	49.3	37.1	13.6	96.5	629.6	2373.1	125.9
2	52.2	34.2	13.6	92.8	844.1	3340.2	132.1
3	57.2	34.2	8.5	86.7	564.4	2634.1	138.7
4	58.4	28.8	12.8	67.6	417.1	1671.4	163.5
5	67.3	24.2	8.5	83.3	625.3	2206.1	233.9
6	72.8	18.3	10.3	76.3	516.2	2141.6	254.8

3.5 Correlation

The correlation of phase composition between DSC and solid-state NMR is presented by plotting the crystallinity of DSC (w_c^{DSC}) on the abscissa axis and the crystallinity of solid-state NMR (w_c^{NMR}) on the ordinate axis. The amount of the interphase and the amorphous phase determined by NMR (w_i^{NMR} and w_a^{NMR}) are correlated with the amorphous phase determined by DSC (w_a^{DSC}). Besides, the correlation between the relaxation times and w_c^{DSC} are also presented.

3.5.1 Phase Composition

Figure 3.10¹ describes the correlation of phase compositions determined by different methods, in which Figure 3.10(a) shows the result for the crystalline phase.

¹The errors of the NMR-MOUSE data in both Figure 3.10 and Figure 3.11 are induced by the systematic error, the detailed information is presented in Appendix D.

The increasing tendencies of w_c^{DSC} and high-field NMR w_c^{NMR} are identical, as the same slope as the masterline can be observed. However, a systematic 15% higher w_c^{NMR} than w_c^{DSC} is detected. Though a similar increasing tendency is observed, the results of w_c^{NMR} determined by NMR-MOUSE is more complicated. With w_c^{DSC} range from 30% to 70%, the changing behavior can be divided into three stages. When w_c^{DSC} is higher than 55%, NMR-MOUSE w_c^{NMR} are in good agreement with w_c^{DSC} , while when w_c^{DSC} is lower than 45%, NMR-MOUSE w_c^{NMR} is, however, almost identical to high-field NMR w_c^{NMR} . It seems that the NMR-MOUSE w_c^{NMR} reaches a platform in the range of w_c^{DSC} from 45% to 55%. However, due to the lack of data points, the real behavior in this region is not clear.

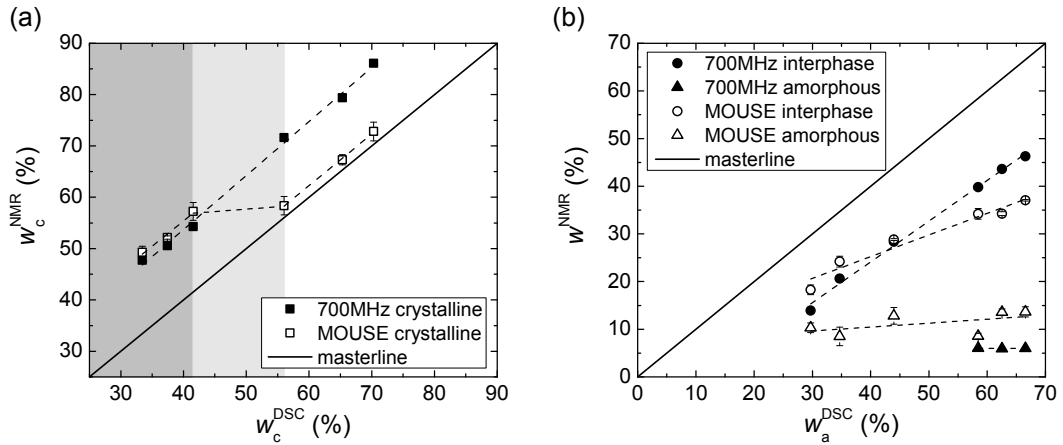


Figure 3.10: Correlation of phase composition of PE with different crystallinities determined by DSC and solid-state NMR, the masterline indicates the situation when the results from different methods are identical: (a) crystallinity and (b) the amounts of the interphase and the amorphous phase.

As only a two-component phase model is applicable for DSC, w_i^{NMR} and w_a^{NMR} determined by both high-field NMR and NMR-MOUSE are correlated with w_a^{DSC} , as shown in Figure 3.10(b). With increasing w_a^{DSC} , on one hand, w_i^{NMR} s determined by both high-field NMR and NMR-MOUSE increase, in which the slope of high-field NMR w_i^{NMR} is identical to the masterline, while that of the NMR-MOUSE w_i^{NMR} is relatively lower. The values of w_i^{NMR} determined by high-field NMR and NMR-MOUSE are almost the same, and both of them are about 10% lower than w_a^{DSC} . On the other hand, w_a^{NMR} determined by both NMR methods

3 Correlation of DSC and Solid-State NMR in a PE Study

not subject to obvious change between different samples, and the value determined by NMR-MOUSE is overall 5% higher than that determined by high-field NMR in the low crystallinity region.

3.5.2 Relaxation Times

Figure 3.11 presents the correlation of the transverse relaxation times. The magnitude difference between T_2 and $T_{2\text{eff}}$ is more than 10 times. Their crystallinity dependences are almost identical, in which both T_2 and $T_{2\text{eff}}$ are stable in all phases with increasing w_c^{DSC} . The stable T_2 and $T_{2\text{eff}}$ indicate the molecular dynamics in different phases of the current samples are independent on the phase composition.

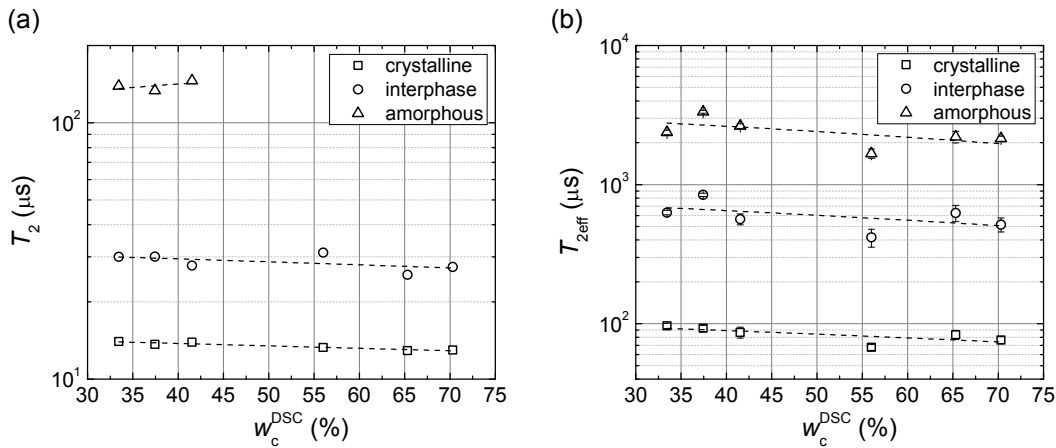


Figure 3.11: Correlation of transverse relaxation times with crystallinity determined by DSC: (a) high-field NMR and (b) NMR-MOUSE.

Figure 3.12 shows the correlation between w_c^{DSC} and T_1 determined by NMR-MOUSE, in which T_1 increases roughly linearly with increasing w_c^{DSC} . Though it is not able to extract the phase composition by one-component fit model, the morphological heterogeneity of the phase domains can be still illustrated based on T_1 differences.^[16,17,137] In longitudinal relaxation, the diversity of the molecular dynamics in the microscopic scale is an important factor that influences the overall T_1 . The relaxation rate is higher at the boundary regions between different phases, where a wider range of \mathbf{B}_{loc} frequencies is available for more

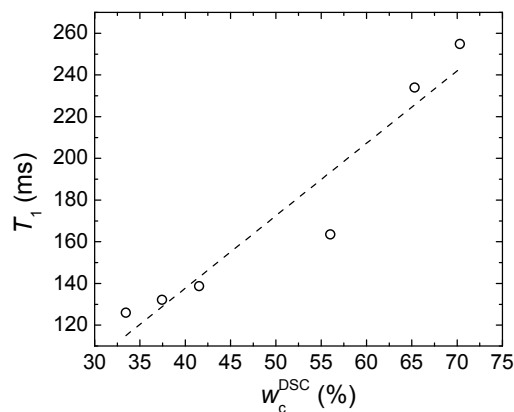


Figure 3.12: Correlation of longitudinal relaxation time determined by NMR-MOUSE with crystallinity determined by DSC.

efficient energy transmission.^[113] With increasing T_1 , it can be inferred that the energy transmission between the spins and lattices becomes less efficient, which indicates the domain enlargement due to increasing w_c .

3.5.3 Evaluation of Different Methods

Based on the above observations, it is clear the consistency between DSC and high-field NMR is high for the characterization of the phase composition of semicrystalline polymers. The benefit of NMR is its ability to extract three components, which is more precise according to the modern phase model. Besides, NMR is also able to describe the molecular dynamics of each phase according to their relaxations. For the current samples, one problem of high-field NMR is the slightly lower phase resolution at room temperature especially for the samples with high crystallinity. When w_c^{DSC} is higher than 55% the amorphous phase is not detectable. This problem can be solved by enlarging the molecular dynamical difference between phases, and one common strategy is to increase the probing temperature. The optimal temperature is depending on the samples. For detailed information please refer to Appendix A and Appendix B.

The application of NMR-MOUSE to the characterization of semicrystalline polymers with a wide range of crystallinities was explored for the first time. Three-component phase composition can be well described for all samples at

3 Correlation of DSC and Solid-State NMR in a PE Study

room temperature, and the results are in good agreement with those determined by other methods. Besides, relaxation times determined by NMR-MOUSE are not only able to describe the molecular dynamics but also the morphology of the material. Furthermore, the small error bars indicate the reproducibility of the NMR-MOUSE is high for solid polymer study.

3.6 Application of NMR-MOUSE to PE Pipes

Thanks to the advantages as portable and open sensor, the applications of NMR-MOUSE to semicrystalline polymers are strongly attractive and with high potential in industry. The most apparent benefit is its ability to investigate the final products in a nondestructive manner on-site. In the current work, the morphological and molecular dynamical gradients of HDPE pipes across the wall were studied by NMR-MOUSE, and its influences on the quality of the final product will be discussed.

3.6.1 Samples and Correlation

Two different HDPE pipes as PE100 and PE80 were extruded with different throughputs of $V_1 = 40$ kg/h and $V_2 = 120$ kg/h in Süddeutsches Kunststoff-Zentrum (SKZ), Würzburg, Germany. The phase composition of the bulk pipes was investigated and correlated by high-field NMR and NMR-MOUSE.

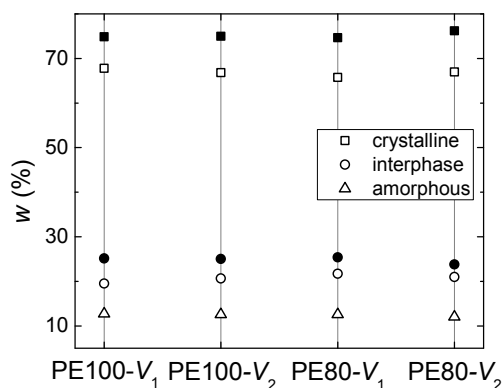


Figure 3.13: Phase composition correlation of HDPE pipes determined by high-field NMR (solid symbol) and NMR-MOUSE (open symbol).

3.6 Application of NMR-MOUSE to PE Pipes

Figure 3.13 shows the phase composition, in which the correlation is in good agreement with that observed in the high w_c region presented in the previous section. Therefore, in the current case, w_c of the pipes determined by NMR-MOUSE can be assumed similar to that determined by DSC.

3.6.2 Gradients across the Wall

Figure 3.14 shows the phase composition of PE100 and PE80 pipes produced with different extrusion throughputs. The digital lift is used to sweep the sensitive slice across the wall to measure a profile. From left to right of the abscissa axis, the figures present the outer surface to the inner surface of the pipes. w_c of PE100 is higher than that of PE80, however, the difference between the pipes with different extrusion throughputs is minor. Most importantly, the morphological gradient across the wall is obvious for all pipes, in which w_c increases slightly from the outer to the inner surface, and the increment is most pronounced at the outer surface regions, as indicated by the gray patterns in the figures. The amounts of the other two phases generally decrease from the outer to the inner surface, and the decreasing tendency is more obvious in the amorphous phase than in the interphase.

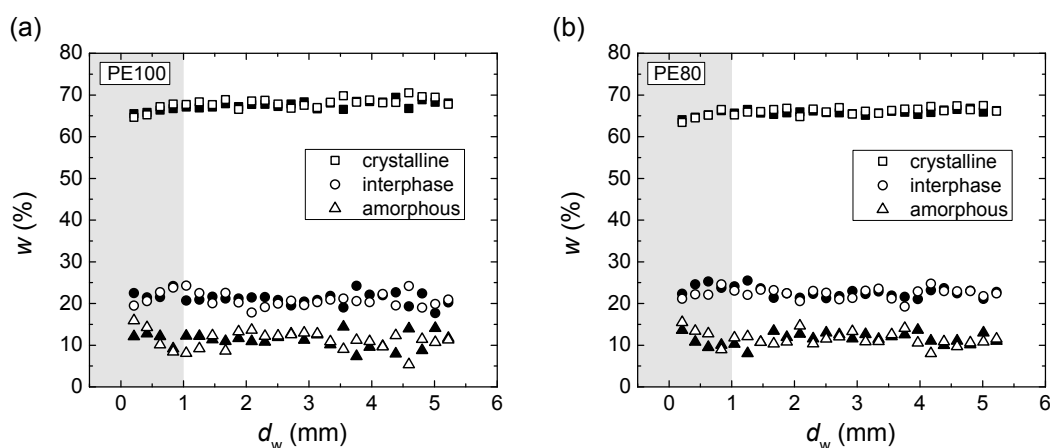


Figure 3.14: Morphological gradient of HDPE pipes across the wall determined by NMR-MOUSE: (a) PE100 and (b) PE80. The solid symbols represent the pipes with the extrusion throughput of V_1 and the open symbols represent those with V_2 .

3 Correlation of DSC and Solid-State NMR in a PE Study

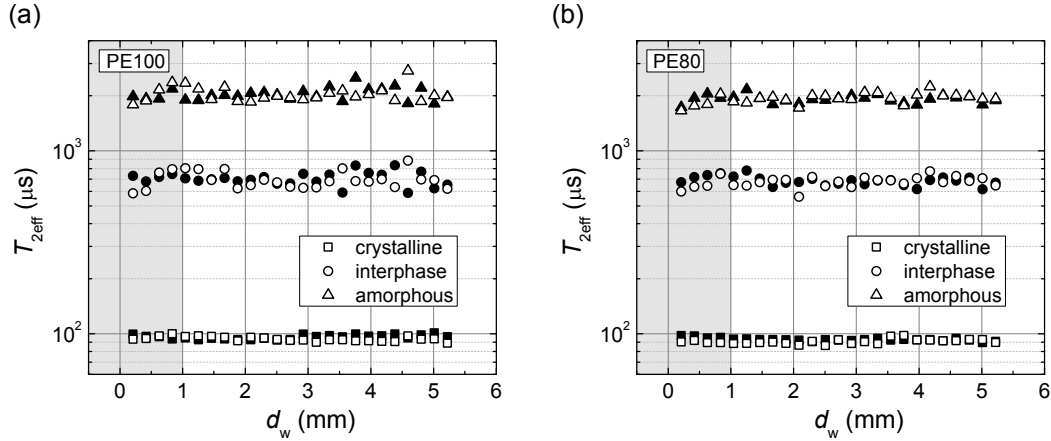


Figure 3.15: Effective transverse relaxation times of HDPE pipes across the wall determined by NMR-MOUSE: (a) PE100 and (b) PE80. The solid symbols represent the pipes with the extrusion throughput of V_1 and the open symbols represent those with V_2 .

Figure 3.15 presents the corresponding $T_{2\text{eff}}$, in which molecular dynamical gradients can be also observed at the outer surface region. $T_{2\text{eff}}^c$ decreases slightly with the wall depth, while $T_{2\text{eff}}^i$ and $T_{2\text{eff}}^a$ increase. This indicates the crystal perfection increase, and at the same time, the chain-frozen effect in the noncrystalline region decreases from outer to inner surface.

3.6.3 Residual Stress

Based on all the above observations, it is clear that morphological and molecular dynamical gradients exist across the pipe wall. In order to understand these phenomena, it is necessarily first to learn the technology of pipe processing by extrusion molding. In pipe extrusion, in order to assist the shaping of the pipe wall, the outside surface is solidified immediately by quenching the melt in the vicinity of the die.¹ While the inner surface is exposed to the air, in which the solidification proceeds with natural cooling. As a consequence, the thermal history differs across the pipe wall, and leads to the generation of the morphological and molecular dynamical gradients. Due to the quenching, at the outer surface

¹Water spray is a widely used method.

region, the chain segments are frozen quickly to intermediate states before they develop into the crystalline lamellae, or relax to a total flexible conformation in the amorphous phase. While in the inner surface region, the chains possess more time to construct a better phase structure, thanks to the slower cooling rate.

Right after the extrusion, the strong morphological and molecular dynamical gradients make the chain segments in the pipe thermodynamically unstable. This causes strong residual stress across the pipe wall, which significantly influences the physical properties and the durabilities of the pipe.^[138,139] Williams *et al.*^[140,141] deduced the actual stress over the crack of the pipes under pressure with the presence of the residual stress across the wall. They demonstrated that the residual stress in the pipe strongly influences the overall stress distribution in the wall and, thus, affects their long term performance. Therefore, it is essential to prevent the formation of the morphological and molecular dynamical gradients during pipe processing. One common strategy is the application of the annealing technique, i.e. by storing the pipes under elevated temperatures for a specific period. With higher free volume the frozen chain segments are able to relax, and to develop into either the crystalline phase or the amorphous phase. Consequently, the residual stress is released and the final physical properties of the product are guaranteed. However, it is necessarily to aware that the chain migration and formation of the perfect phase structure cannot be achieved completely within limited time, and whenever place the pipes in a suitable condition the annealing procedure can be resumed again.

3.7 Summary

The characterization of PE with different crystallinities was carried out by DSC, high-field NMR, and NMR-MOUSE, respectively. A correlation study between different methods was performed. The results indicate that the phase compositions determined by DSC and NMR agree with each other very well in a wide range of crystallinities. However, the different theoretical hypotheses of different methods have to be taken into account. T_{2s} and $T_{2\text{eff}s}$ determined by high-field NMR and NMR-MOUSE are relatively stable for each phase regardless the crys-

3 Correlation of DSC and Solid-State NMR in a PE Study

tallinities of the sample. However, T_1 determined by NMR-MOUSE increases with the crystallinity, which indicates the domain dimension of the phases increases.

The morphological and molecular dynamical gradients of HDPE pipes was observed by NMR-MOUSE across the pipe wall. They are induced by quenching during the extrusion molding, and this phenomenon is more remarkable at the outer surface region of the pipe. The gradients are the main reasons for the residual stress that influences the physical properties and long term performance of the pipes. In the current study, it has been proved NMR-MOUSE is an effective technique to monitor the qualities of HDPE pipes. Besides, all the above observations indicate that solid-state NMR is an information rich technique that is able to describe the morphology and molecular dynamics of semicrystalline polymer precisely. It is an effective method able to provide important details in the polymer material study.

4

Study on Aging of HDPE Pipes by Solid-State NMR

One of the major applications of HDPE is for pipes to transport and distribute water, natural gas, and sewer.^[142] Pipe systems made of HDPE are a cost effective solution for various piping problems, municipally and industrially. Its advantages include unique joint integrity, toughness, flexibility, lower weight, great durability towards corrosion, etc.^[143] According to the criteria, HDPE pipes are expected to have a lifetime up to 50~100 years under normal operating condition.^[144] However, the real service time, in fact, depends on the local conditions such as the temperature, pressure, and humidity where the systems are installed. HDPE was first introduced into high pressure water distribution early in the 1980s,^[145] and its demand was steadily increasing over the last decades. Nowadays, the first generation systems reach 30 years of service time. Considering an average lifetime of about 50 years for these pipe systems, it becomes more and more important to estimate their remaining service time. To meet this end it is necessarily to understand the aging mechanism of HDPE pipes.

Agings that occur to HDPE pipes can be attribute to two aspects, chemical and physical.^[146] Chemical aging is dominated by the oxidations on molecular chains,^[147] while instead, physical aging is caused by the mechanical changes of the material. Both of them influence the morphology and mechanical properties of the pipe and, consequently, affect its long term performance.^[148] In the present

4 Study on Aging of HDPE Pipes by Solid-State NMR

work, physical aging of HDPE pipes was simulated by the hydrostatic pressure test at elevated temperature. The changes of morphology and molecular dynamics of the pipe due to aging were investigated by a combination of DSC and solid-state NMR. Both of them are related to the storage time. The reason of such phenomena will be discussed, and based on which the aging mechanism of the HDPE pipes will be explained.

4.1 Materials

All the pipes were extruded by SKZ with the same processing parameters. The extrusion temperature was 190 °C and the extrusion throughput was 40 kg/h. Two different HDPE classes were applied for this study. The first one is PE100, it is the current highest class in the HDPE pipe group. According to ISO 12162 this material should stand with a 10 MPa hoop stress (σ) for 50 years at 20 °C.^[144] The introduction of PE100 is more than one decade ago, which was expected to meet the extended requirements from the end users that are beyond the technical or economical limits of those already existing HDPE pipes. Now it is a well established pipe material offering reliable operational performance under extreme loading conditions. A whole range of end-user specifications as well as both national and international standards have been met by PE100 material today. The other PE is from a less quantified class. It is typically used for applications other than pipes, and the pipes made from it are only available for the laboratory study and comparison. These pipes are named as PEHD pipes in this work.

4.2 Aging of HDPE Pipes

As early as in mid-1980s, Eriksson and Ifwarson^[149] have established the hydrostatic pressure test system to evaluate the quality of plastic pipes. It is now the most widely used method to simulate the natural aging of HDPE pipes in an accelerated manner. In general, based on the testing result, three different stages of failures can be identified according to the fracture types, and in terms of which the lifetime of the pipes can be estimated.^[149–151]

4.2.1 Hydrostatic Pressure Test

Hydrostatic pressure test of the HDPE pipes was carried out in SKZ with the standard setup as shown in Figure 4.1.^[152] Both ends of the pipe segments are connected to and closed by the molds, in which the controlled hydrostatic pressure was applied. Then the whole system is placed in an atmosphere bath which is able to control the temperature of the system. The benefit of this setup is its ability to simulate different aging procedures by simply changing the testing media in- and outside of the pipes as well as the testing temperature of the whole system.

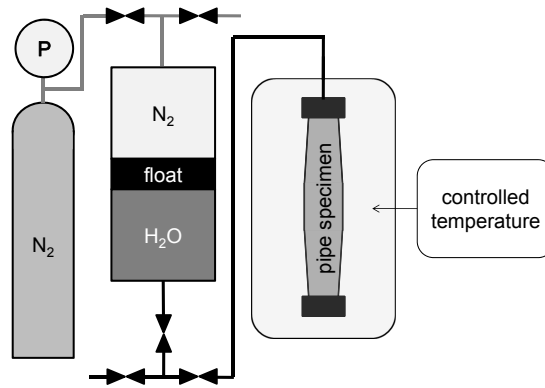


Figure 4.1: Schematic diagram of the standard hydrostatic pressure test setup.

In the current study, hydrostatic pressure test of the HDPE pipes was carried out at 80 °C for all specimens. In order to prevent the chemical reactions, deionized water both in- and outside of the pipes was applied and the hydrostatic pressure is provided by nitrogen. Different hydrostatic pressures¹ were applied to observe different failures according to the storage time (t_s). The observation time window in the current work was up to 12 000 h, which is more than 1 year and 4 months.

4.2.2 Hoop Stress

The result of the hydrostatic pressure test is conventionally presented on a logarithmic scale in which the abscissa is the dependent variate $\lg(t_s/h)$ and the

¹ σ applied in the hydrostatic pressure test was ranging from 2 MPa to 7 MPa.

4 Study on Aging of HDPE Pipes by Solid-State NMR

ordinate is the independent variate $\lg(\sigma/\text{MPa})$, as shown in Figure 4.2(a).^[152] Normally, three failure stages can be observed according to the different absolute gradient between $\lg \sigma$ and $\lg t_s$. Stage I failure is featured by a low absolute gradient of $|d(\lg \sigma)/d(\lg t_s)| \approx 0.03$ and high σ , while in stage II failure the absolute gradient increases to about 0.3 with lower σ . In stage III failure, the absolute gradient is very high, an almost vertical decrement of $\lg \sigma$ with little change on $\lg t_s$ can be observed, and σ in this stage is very low. The fracture types of the pipe in these three stages are also different. In stage I failure the fractures are ductile, in which a yield followed by a large deformation of the material can be observed. In stage II failure the fractures are brittle which is characterized by the formation of slit leakage. Stage III failure also shows the brittle fractures, but here a number of slit leakages occurs simultaneously on the specimens.^[153–157]

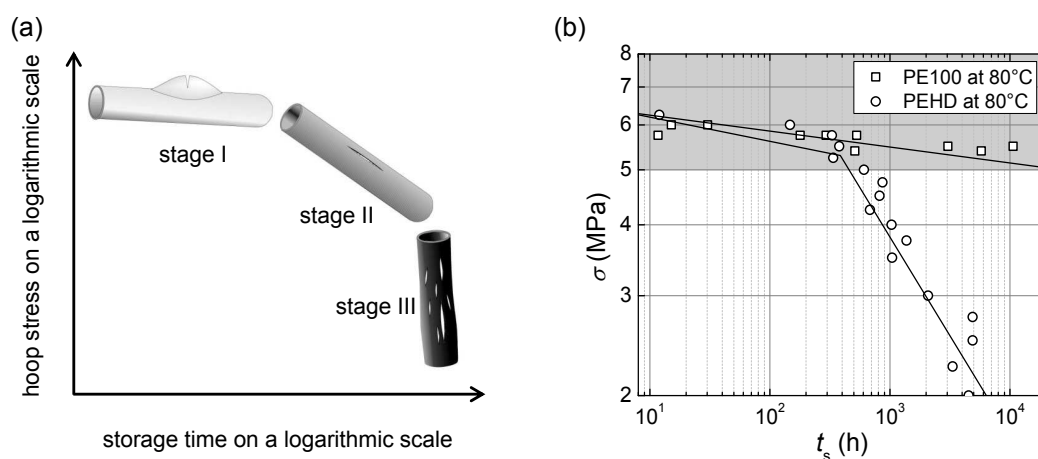


Figure 4.2: (a) Schematic diagram of fracture curve for HDPE pipes at elevated temperature, and (b) hoop stress as a function of the storage time (the data are provided by SKZ).

Eriksson and Ifwarson^[149] have described the fracture mechanism in different stages. In stage I and II failure the fractures are purely mechanical and related the models for physical aging. However, stage III failure which happens at much lower stresses than stage II failure requires a certain level of oxidative degradation. In fact, these three failure types are in competition with each other during the test. When σ is very high, the yield occurs very fast which leads the pipes to

ductile stage I failure, while when σ is low, the long testing period induces the oxidative reactions to deteriorate the material, thus, the pipes end up in brittle chemical fractures with stage III failure. With the application of moderate σ , the pipes are subjected to an intermediate stress, and brittle physical fractures occur within a medium testing span, so that the samples end up in stage II failure.

In stage III failure, the chemical degradation is caused by the migration and the gradual loss of anti-oxidants in the bulk material. In this case, the oxidation of the molecular chains with the oxygen from carbonyl and hydro-peroxides takes place more easily. This reaction leads to chain scissions in the material and, thus, reduces the molecular weight.^[158] Khelidj *et al.*^[159] and Colin *et al.*^[157,160] reported that the brittle stage III failure of HDPE pipe occurs when the weight average molecular mass becomes lower than the critical value of $\overline{M}_w = 70$ kg/mol. The chemical aging of HDPE pipes has been extensively studied by the Gedde's group.^[161–163] They claimed that when the hydrostatic pressure test takes place with a temperature higher than 90 °C and relatively low σ , the pipe failures are more probably governed by chemical oxidation.

Instead of chemical deterioration, physical aging rather involves with mechanical changes on the material.^[148] Litvinov and Soliman^[113] have investigated the stage I failure of pipes made of polypropylene (PP) copolymers under different testing temperatures. They claimed that the failure in stage I is accompanied by the annealing in the crystalline phase as well as by the chain elongation in the noncrystalline regions. Lu and Brown^[150,164] reported that the brittle fracture in stage II failure of HDPE pipes is due to slow crack growth, which can be explained by the stress concentration effect.

Figure 4.2(b) illustrates the hydrostatic pressure test results of the specimens. For PE100 pipes, in the current observation time window, σ decreases slightly with t_s and all the detected fractures are ductile. These characterizations indicate a typical stage I failure. However, PEHD pipes behave differently, in which stage II failure with σ less than 5.5 MPa can be detected after only about 350 h storage. Besides, with σ of about 2 MPa the test can last for only 3300 h before the brittle fractures occur to the pipe. The initial σ at stage I failure of these two different pipes are similar, which indicates the tensile strengths of them are about the same. However, when considering durability, PEHD pipe is not a good

candidate for long term pipe systems to transport water, especially, at elevated temperature. Furthermore, no stage III failure was observed for both classes, which indicates the chemical deterioration has been diminished to a very low extent. It is uncompetitive at least in the current testing window.

4.3 Phase Composition and Chain Relaxation

The failures observed in both PE100 and PEHD pipes are dominated by physical aging.¹ In order to understand the aging mechanism, the study of morphology and molecular dynamics is very important. Both solid-state NMR and DSC were applied to investigate the change of the phase composition due to the hydrostatic pressure and elevated temperature. Besides, the molecular dynamics are also studied via high-field ¹H FID and longitudinal relaxation.

4.3.1 DSC and ¹H NMR Relaxation Measurements

All samples for investigation are from the pipe parts without obvious fracture or yield. A NETZSCH DSC 200F3 apparatus was applied to study the melting behavior as well as the crystallinity. The experimental parameters are the same as described in Section 3.2.1.

¹H static NMR measurements were performed on a Bruker 200 MHz NMR spectrometer by using a high power solid-state probe body with a 4 mm coil. The optimized 90° rf pulse was 3 μs. In order to have better resolution among different phases, all the measurements were performed at 90 °C.² The FIDs were recorded with a 0.5 μs dwell time, the number of scans was 64 with a recycle delay of 5 s, and the shortest available t_d of 5.5 μs was applied. ¹H FID recorded after single 90° pulse³ was applied to extract the phase composition as well as T_2 , and inversion recovery pulse sequence⁴ was applied to measure the longitudinal relaxation.

¹stage I or stage II failure

²For detailed information about the optimum probe body programmed temperature and sample real temperature, please see Appendix A and Appendix B.

³For pulse sequence, please see Figure 2.7(a).

⁴For pulse sequence, please see Figure 2.8(b).

4.3.2 Crystallinity Determined by DSC

Figure 4.3^{1,2} depicts w_c and T_m determined by DSC. The crystallinity of PE100 increases slightly with t_s under the testing condition. For PEHD the changes are more complicated. All the after tested pipes show higher w_c than that of the fresh pipe. However, the increment is less for those with longer t_s .

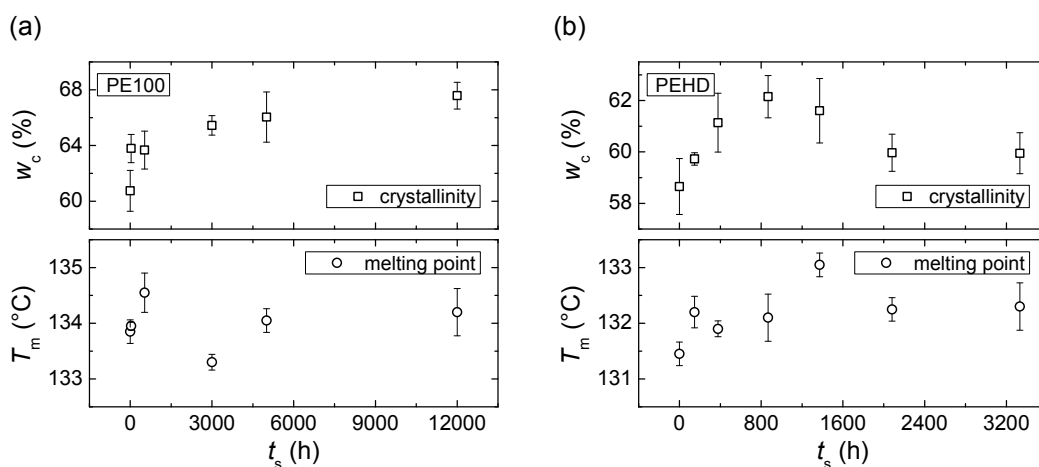


Figure 4.3: Dependence of DSC crystallinity and melting temperature on the storage time for: (a) PE100 and (b) PEHD.

In stage I failure, the maximum increment of w_c in PEHD pipes is about 4%, while it is only about 2% for PE100 even after 12 000 h storage. In stage II failure of PEHD pipes, the increment of w_c reduces to about 2% after more than 2000 h storage. In addition, w_c of PE100 is in general 2~5% higher than that of PEHD. T_m shows more arbitrary changes due to the hydrostatic pressure test in both classes. Though the systematic error of T_m determined by the DSC apparatus is very low, no clear trend can be described. Nevertheless, it can be still confirmed that T_m of PE100 is generally about 2 °C higher than that of PEHD, which indicates a larger crystal size.^[165]

¹The errors in the figures are calculated based on repeated measurements, in which two specimens from different spots of the pipe were measured for PE100 pipes at each different storage time and three specimens were measured for the PEHD pipes. The error is mainly induced by the inhomogeneity of pipes which is indicated in Appendix F for PEHD pipes. As an industrially available class, the homogeneity of PE100 pipes is higher than PEHD pipes.

²For systematic error of DSC, please see in Appendix C.

4.3.3 Phase Composition Determined by ^1H FID

Figure 4.4^{1, 2, 3} shows the phase composition determined by ^1H FID. The three-component fit model as Equation 3.1 was applied to fit all the decays. At a temperature of 90°C , the resolution between the interphase and the amorphous phase has been improved significantly. The NMR w_c is in overall about 5% higher than that determined by DSC.

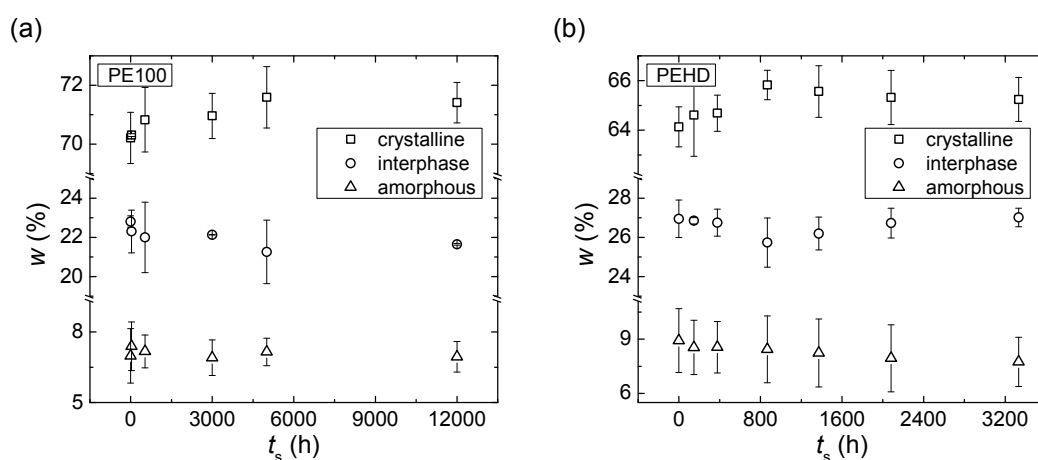


Figure 4.4: Dependence of the phase composition on the storage time determined by ^1H FID: (a) PE100 and (b) PEHD.

In the crystalline phase, the changes due to hydrostatic pressure test are basically the same as those observed by DSC for both PE100 and PEHD pipes. However, due to the three-component fit model, the changes of the noncrystalline phases are more complex. In PE100, the amount of the interphase decreases steadily with t_s , while that of the amorphous phase is about stable. In PEHD, the changing behavior of the interphase is in an inverse manner compare to that of the crystalline phase, and the amount of the amorphous phase decreases mildly with t_s . Besides, the crystallinity of PE100 is higher than that of PEHD. The amount of interphase of PEHD is higher than that of PE100, while that of the amorphous phases are almost at the same level for them.

¹The errors in the figures are calculated in the same way as described for Figure 4.3.

²For inhomogeneity of PEHD pipes, please see Appendix F.

³For systematic error of high-field NMR, please see in Appendix E.

4.3.4 Relaxation Times

Figure 4.5 shows T_2 of different phases with t_s determined by ^1H FID. T_2 of each phase for both PE100 and PEHD undergoes a constant reduction with t_s . Besides, T_2 decrement in PEHD is more significant than PE100, especially, in the interphase and the amorphous phase. For instance, T_2^a of PEHD subjects an approximate 30% reduction after 3300 h storage, while it is only about 15% for PE100 even after 12000 h. This indicates PEHD is more liable to aging under hydrostatic pressure test. Furthermore, T_2 differences between PE100 and PEHD are also obvious, especially in the interphase and the amorphous phase, in which T_2^i of PE100 is about 15% higher than that of PEHD in overall and that of T_2^a is about 10% higher. As demonstrated in Section 2.3, T_2 is related to the molecular dynamics. A shorter T_2 indicates a higher chain restriction and lower chain flexibility. The result of T_2 illustrates that during the hydrostatic pressure test, the chains in all phases get more restricted with t_s . As a result, the brittleness of the material increases, which reduces its impact strength. Besides, the higher T_2^i and T_2^a of PE100 also guarantee a better toughness over PEHD.

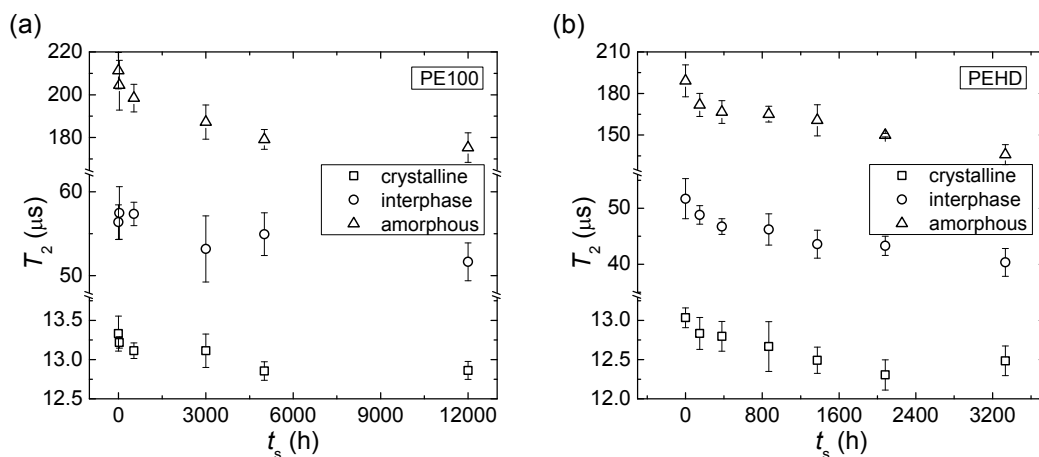


Figure 4.5: Dependence of ^1H transverse relaxation times of different phases on the storage time determined by FID: (a) PE100 and (b) PEHD.

For HDPE, the inversion recovery curves measured at high-field can only be fitted by one-component model. T_1 increases with t_s in both PE100 and PEHD pipes, and the increment is more remarkable between the samples in the short t_s

4 Study on Aging of HDPE Pipes by Solid-State NMR

region in both cases, as shown in Figure 4.6. In PE100, after about 3000 h, T_1 reaches a plateau, while in PEHD this time is about 800 h. T_1 gradient is higher in PEHD than PE100, while the overall values are lower. As discussed in Section 3.5.2, in semicrystalline polymers T_1 relates to the domain dimensions, increasing T_1 indicates the domain sizes of the phase increases with t_s .

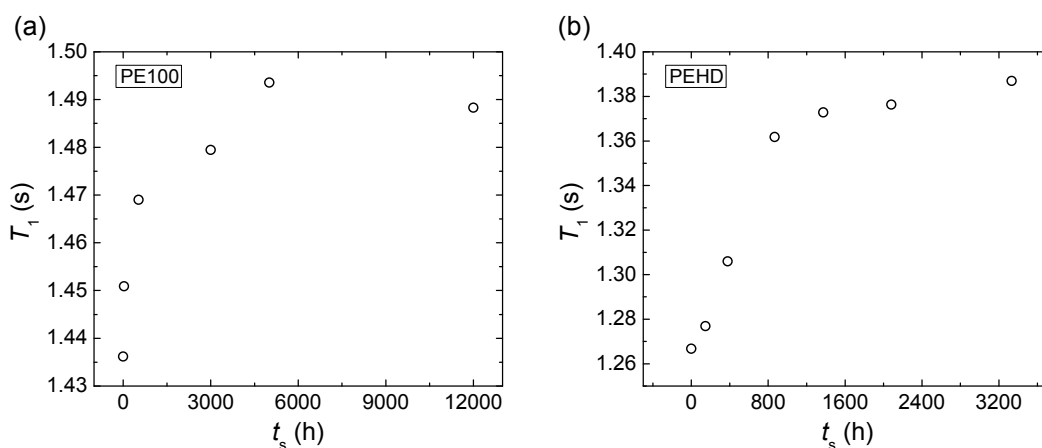


Figure 4.6: Dependence of ^1H longitudinal relaxation time on the storage time by inversion recovery pulse sequence: (a) PE100 and (b) PEHD.

4.3.5 Hoop Stress Correlation in Stage II Failure – I

For stage I failure, as shown in Figure 4.2(b), the change of σ with t_s is very weak. Therefore, the correlation is only investigated for stage II failure for PEHD, where the brittle fractures are featured by a higher $|\text{d}(\lg \sigma)/\text{d}(\lg t_s)|$ absolute gradient. The transition from stage I to stage II failure occurs at around 350 h, at which the failures are dominated by both ductile and brittle fractures simultaneously. Hence, in order to correlate σ with pure stage II brittle fractures, the correlation was carried out on the samples with t_s higher than 800 h.

Figure 4.7 shows the correlation between phase composition and σ^{-1} . Both crystallinities determined by DSC and ^1H FID are reciprocal to σ^{-1} . The absolute gradient of $|w_c/\sigma^{-1}|$ determined by DSC is higher than that determined by ^1H FID. The fraction of the interphase determined by ^1H FID is proportional to σ^{-1} , while that of the amorphous phase is in a weak reciprocal ratio. Figure 4.8

4.3 Phase Composition and Chain Relaxation

shows the correlation between relaxation times and σ^{-1} . T_2^c , T_2^i as well as T_2^a are all reciprocal to σ^{-1} , and the absolute gradient follows $|T_2^a/\sigma^{-1}| > |T_2^i/\sigma^{-1}| > |T_2^c/\sigma^{-1}|$. On the other hand, T_1 is proportional to σ^{-1} . The correlations of phase composition and relaxation time with σ^{-1} behave similar to their relations with t_s . However, these phenomena are unobservable for the stage I ductile fractures.

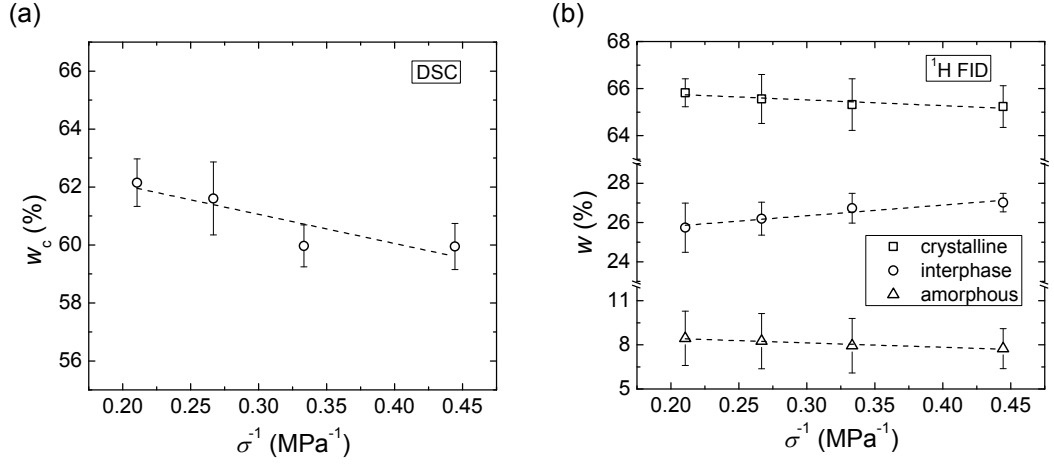


Figure 4.7: Correlation between hoop stress and phase composition of PEHD pipes in stage II failure: (a) DSC crystallinity and (b) ^1H FID phase composition.

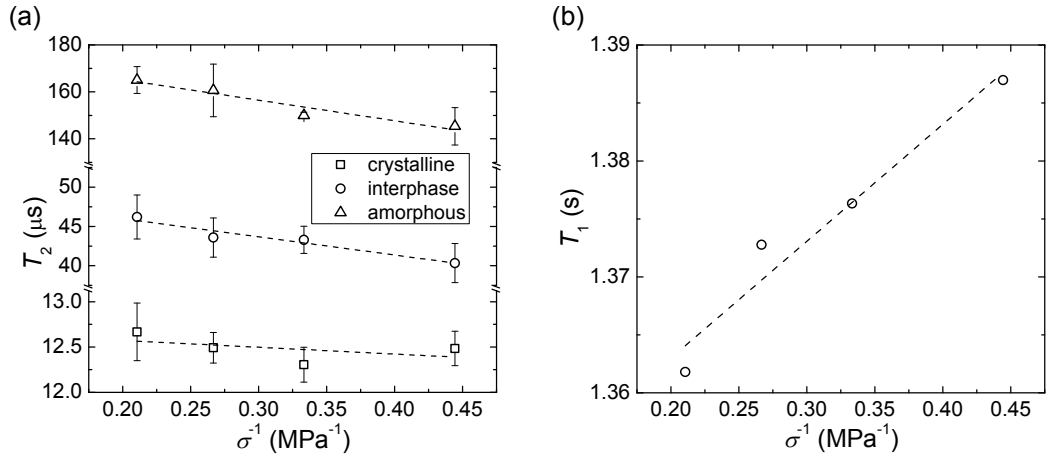


Figure 4.8: Correlation between hoop stress and relaxation times of PEHD pipes in stage II failure: (a) ^1H transverse relaxation time by FID and (b) ^1H longitudinal relaxation by inversion recovery pulse sequence.

Both phase composition as well as molecular relaxation change with t_s . The phase composition changes differently at different failure stages, and the observation from DSC as well as NMR are basically the same. However, in order to understand the molecular mechanism behind the observed phenomena, more detailed morphological information is necessarily.

4.4 Domain Sizes by ^1H Spin-Diffusion NMR

^1H spin-diffusion was first introduced by Goldman,^[166] which was then developed to establish a connection between the distance scale of the morphological heterogeneous in polymers and the time scale of the spin-spin relaxation in NMR entities.^[23,167–171] It is a powerful approach, able to characterize the domain sizes of semicrystalline polymers and polymer blends in a broad dimensional scale, from 0.1 nm to about 200 nm, based on different aspects (e.g. morphology and molecular dynamics).^[22,172–175] Spin-diffusion process can be either directly measured by the resolved different chemical shifts on the resonant lines of the solid samples,^[168,169,176] or the different molecular dynamics reflected by the NMR line width of absorption broad line spectra,^[22] or on the corresponding T_2 determined by FID.^[177,178] The quantitative morphological information is deduced based on the different rates of the spins diffuse across different domains due to the distinctions in molecular organization, molecular dynamics, and/or phase composition. Information derived from spin-diffusion NMR is often similar to that obtained from XRD^[179] or coherent neutron scattering.^[180] However, in contrast to the latter techniques, the benefit of ^1H spin-diffusion is that no isotopic labeling of the specimens is necessarily. Besides, one most obvious advantage of spin-diffusion NMR over XRD and/or coherent neutron scattering is its abilities to describe the domain sizes of the noncrystalline regions of semicrystalline polymer, i.e. the interphase and the amorphous phase.

4.4.1 Spin-Diffusion Measurement

The samples used in the previous section are measured by spin-diffusion pulse sequence on the Bruker 200 MHz NMR spectrometer with the same probe body

and identical parameters as used for the ^1H FID measurement. Figure 4.9 represents the spin-diffusion pulse sequence with a double-quantum dipolar filter.^[26,98] The first four 90° pulses compose the dipolar filter, where $\tau_{e/r}$ is the excitation/reconversion time and τ_{DQ} is the double-quantum coherence period. After that, a spin-diffusion period labeled by different mixing times τ_m is applied to evaluate the magnetization diffusion. Finally, with the application of the fifth 90° pulse, the rf coil records the signals. In the present measurements, both $\tau_{e/r}$ and τ_{DQ} were fixed to $5\ \mu\text{s}$ which is suitable for semicrystalline polymers, and a varying list of τ_m within the time scale shorter than T_1 was used to evaluate the spin-diffusion process.^[171]

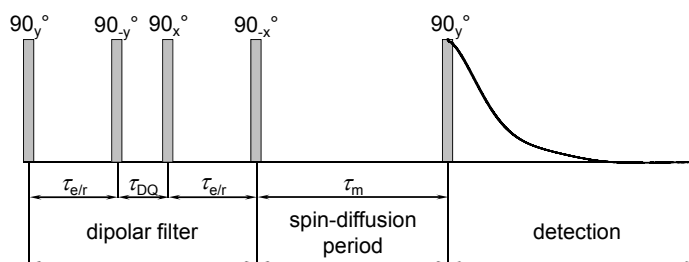


Figure 4.9: Spin-diffusion pulse sequence with a double-quantum dipolar filter.

4.4.2 Analytical Solutions

The application of ^1H spin-diffusion NMR to the domain size evaluation is based on the multicomponent phase model with lamellar core structures in the semicrystalline polymers. Figure 4.10^[181] describes the lamellar three-component phase model that is suitable for PE, in which the lamella ‘ c ’ axis is in the horizontal direction. Lamellae are the stems, and the interphase as well as the amorphous phase assemble on them layer by layer. The morphological period is composed by (half-)amorphous–interphase–crystalline–interphase–(half-)amorphous. d_c , d_i , d_a are the domain sizes of the crystalline phase, the interphase, and the amorphous phase along the ‘ c ’ axis, respectively. In order to match the morphology model and the spin-diffusion analytical solutions, several assumptions are necessary. First the molecular structure and chain organization in each independent phase are homogeneous. Second, there are clear boundaries between each phase,

4 Study on Aging of HDPE Pipes by Solid-State NMR

which are identified by different molecular dynamics. Third, the structure of the morphological period throughout the whole material matrix is uniform.

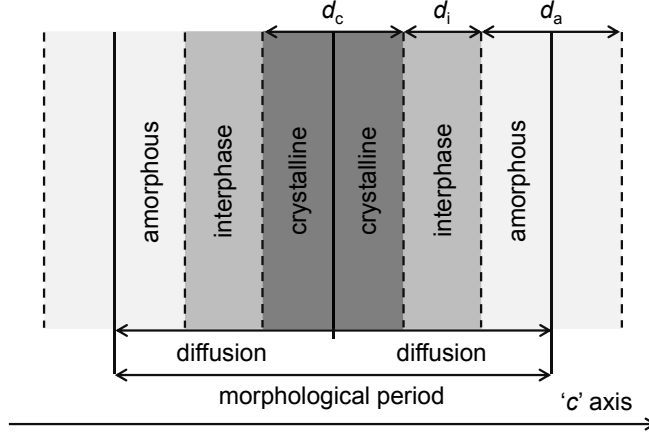


Figure 4.10: Morphological model for spin-diffusion analytical solutions.

With the application of a double-quantum dipolar filter, the spin magnetization concentrates in the crystalline phase. Right after that, the magnetization starts to diffuse along 'c' axis out of the crystalline domains in both directions. When τ_m is very short, the magnetization can hardly leave the crystalline regions, while when τ_m is long enough the magnetization is able to spread over the whole morphological period. It starts in the crystalline phase and diffuses through the interphase to the amorphous phase. In order to make the spin-diffusion process able to be described by the analytical solutions, several assumptions are essential. First the spin-diffusion processes in each phase follow the Fick's diffusion law along 'c' axis as:

$$D \frac{\partial^2 m}{\partial x^2} = \frac{\partial m}{\partial t}, \quad (4.1)$$

where m is the magnetization concentration, D is the diffusion coefficient, x is the space dimension along 'c' axis. The diffusion time t , in the current case, is equal to τ_m . Second, the molecular dynamics are homogeneous throughout each phase domain, and is supposed to be an average effect of chain motions and atomic interactions; therefore, it can be assumed that the spin-diffusion in each phase is governed by a single coefficient D_c , D_i , and D_a in the crystalline phase, the interphase, and the amorphous phase, respectively. Third, the magnetization

4.4 Domain Sizes by ^1H Spin-Diffusion NMR

concentrations as well as the diffusion fluxes are continuous through the morphological period; however, due to the different proton densities in each phase, the diffusion flux should be rewritten as:

$$J = -\rho D \frac{\partial m}{\partial x}, \quad (4.2)$$

where J is the diffusion flux, and ρ is the proton density. Fourth, magnetization diffuses only along the ‘ c ’ axis to both ends of the morphological period, while there’s no diffusion between different periods or across each period’s center, as indicated by the solid vertical lines in Figure 4.10.

Finally, with all the above assumptions, the magnetization intensity of each phase can be written as a function of ρ and m . In one morphological period with a diffusion time of τ_m after the double-quantum dipolar filter the equations are:^[181]

$$I_c(\tau_m) = 2 \int_0^{\frac{d_c}{2}} \rho_c m_c dx, \quad (4.3a)$$

$$I_i(\tau_m) = 2 \int_{\frac{d_c}{2}}^{\frac{d_c}{2} + d_i} \rho_i m_i dx, \quad (4.3b)$$

and

$$I_a(\tau_m) = 2 \int_{\frac{d_c}{2} + d_i}^{\frac{d_c + d_a}{2} + d_i} \rho_a m_a dx, \quad (4.3c)$$

where m_c , m_i , and m_a represent the magnetization of the crystalline phase, the interphase, and the amorphous phase, respectively, and m of each phase related to D_c , D_i , and D_a , all together. Based on these analytical solutions, domain size of different phases can be extracted. The deduction of the whole analytical solution is very complicated. For more detailed information, Buda’s Ph.D. thesis^[182] and the references there^[22,23,171,172,183,184] are recommended.

Besides, information of ρ and D is indispensable for the solutions. For HDPE, it is well accepted that the density of the crystalline phase is 0.99 g/cm^3 and that of the amorphous phase is 0.87 g/cm^3 .^[185] The density of the interphase is, however, not available. In the current study, an arithmetic average value of the crystalline phase and the amorphous phase was taken,^[40] and based on which the

4 Study on Aging of HDPE Pipes by Solid-State NMR

proton densities of $\rho_c = 0.14 \text{ mol/m}^3$, $\rho_i = 0.13 \text{ mol/m}^3$, and $\rho_a = 0.12 \text{ mol/m}^3$ for each phase can be calculated, respectively.

4.4.3 Spin-Diffusion Coefficients

Spin-diffusion coefficient indicates the diffusivity of the magnetization, it is related to the chain motions as well as intra- and intermolecular interactions in different phases. The values of D_c and D_a for semicrystalline polymers can be calculated as:^[23]

$$D_c \approx \frac{1}{12} \sqrt{\frac{\pi}{12 \ln 2}} \langle r^2 \rangle \Delta\nu_{1/2} \quad (4.4a)$$

and

$$D_a \approx \frac{1}{6} \langle r^2 \rangle [\zeta \Delta\nu_{1/2}]^{1/2}, \quad (4.4b)$$

where $\Delta\nu_{1/2}$ is the line width at the half height of the spectrum of each different phases, the values can be obtained from the deconvolution of the proton NMR broad lines as shown in Figure 4.11. $\langle r^2 \rangle$ is the mean square distance between the nearest spins, in the current study, $\langle r^2 \rangle = 0.0484 \text{ nm}^2$ is taken for all phases, and is assumed to be temperature independent.^[40] ζ is a cut off parameter for the Lorentzian line shape.^[186] It is the frequency width of the Lorentzian broad line from the adsorption signals of the amorphous phase. Again, due to a lack of supportive theory, the same strategy as ρ_i was applied to calculate D_i for the interphase in this study.

According to the current results, D from different phases does not subject to big changes with t_s under hydrostatic pressure test, and all the differences observed are in the error range. Therefore, uniform diffusion coefficients of $D_c = 0.38 \text{ nm}^2/\text{ms}$, $D_i = 0.23 \text{ nm}^2/\text{ms}$, and $D_a = 0.08 \text{ nm}^2/\text{ms}$ were applied for PEHD. While for PE100, these values are $0.39 \text{ nm}^2/\text{ms}$, $0.24 \text{ nm}^2/\text{ms}$, and $0.08 \text{ nm}^2/\text{ms}$, respectively. It is obvious that due to the different molecular dynamics D differs remarkably between different phases. The $D_c > D_i > D_a$ relation indicates the magnetization diffusivity in the crystalline phase is higher than that in the interphase, and that of the amorphous phase is the lowest. Besides, D_c in PE100 is higher than in PEHD, which indicates that the diffusion in PE100 proceeds faster than PEHD in the crystalline phase.

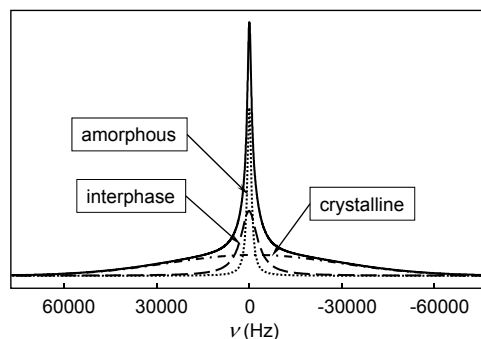


Figure 4.11: ^1H broad line NMR spectrum of HDPE. The deconvolution according to different T_2 s illustrates a crystalline phase with the widest line width (dash dotted line), a interphase with an intermediate line width (long dashed line), and an amorphous phase with the narrowest line width (dotted line).

4.4.4 Spin-Diffusion Curves

Figure 4.12 shows the spin-diffusion spectra of PE100 pipe recorded at different τ_m .¹ All the figures are in the coordinate systems with the same scales on both abscissa and ordinate axes. The line shape changes according to τ_m , in which the narrow line component gets stronger with increasing τ_m . After the application of the double-quantum dipolar filter for about 1 ms, the magnetization starts to diffuse from the crystalline phase to the interphase, as shown in Figure 4.12(a). A weak signal with narrow bandwidth can be observed on the top of the strong broad line, which describes the signals from the interphase and the crystalline, respectively. When τ_m is long enough, the magnetization is able to diffuse throughout the whole morphological period, thus, signals from all phases can be detected as shown in Figure 4.12(d).

The three-component model as Equation 3.1 is again applied to extract the magnetization intensity of each phase at different τ_m from the corresponding FIDs. The spin-diffusion curves of each phase are displayed in Figure 4.13. The diffusion process completes at $\tau_m \approx 100$ ms, after which the magnetization is dispersed homogeneously in the whole matrix. The diffusion curves also give the information of the phase composition at long τ_m , but only within the time domain

¹The presented result is from the pipe without hydrostatic pressure test.

4 Study on Aging of HDPE Pipes by Solid-State NMR

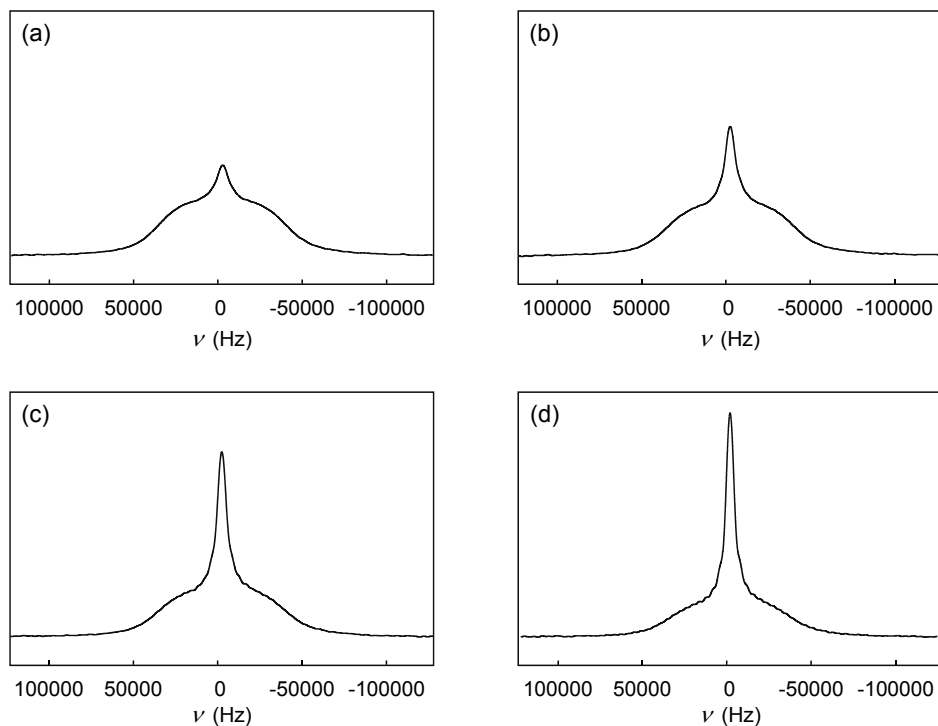


Figure 4.12: ^1H spin-diffusion spectra with different mixing times: (a) $\tau_m = 1$ ms, (b) $\tau_m = 6$ ms, (c) $\tau_m = 22$ ms, and (d) $\tau_m = 300$ ms.

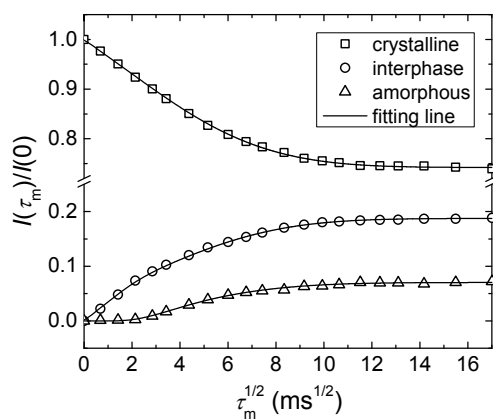


Figure 4.13: ^1H spin-diffusion curves. The symbols are the experimental data and the solid lines are the fitting results by the analytical solutions.

where no obvious longitudinal relaxation is detected. For example, from $\tau_m \approx 100$ ms to $\tau_m \approx 300$ ms in the current case. The solid lines are the fit results by the analytical solutions, based on which the domain sizes can be obtained.

4.4.5 Domain Sizes

Figure 4.14¹ depicts the dependence of domain sizes on the storage time. It is similar to the phase composition described in Section 4.3.2, except d_a , in which an increasing trend was observed in PE100, while a decreasing trend was observed in PEHD in the long t_s region. The difference between these two different pipe classes is obvious: d_c of PE100 is about 30% higher than that of PEHD in overall and d_a is about 5% higher, while d_i of them is similar.

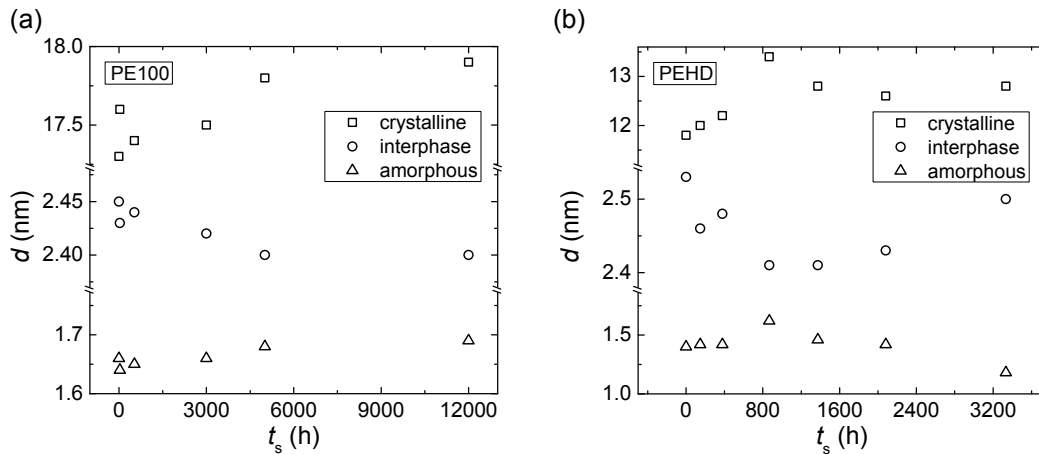


Figure 4.14: Dependence of the domain sizes on the storage time: (a) PE100 and (b) PEHD.

Figure 4.15 shows the dependence of the long period on the storage time. It is similar to d_c in both PE100 and PEHD samples. This is because the crystalline phase is the dominant phase in HDPE. However, the sensitivity of the change of the long period to the hydrostatic pressure test is different between these two classes, in which PEHD changes remarkably more than PE100.

¹The errors as shown in Figure 4.4 can be used as the reference to estimate the errors of the domain size in Figure 4.14 and the long period in Figure 4.15 determined by NMR spin-diffusion measurement.

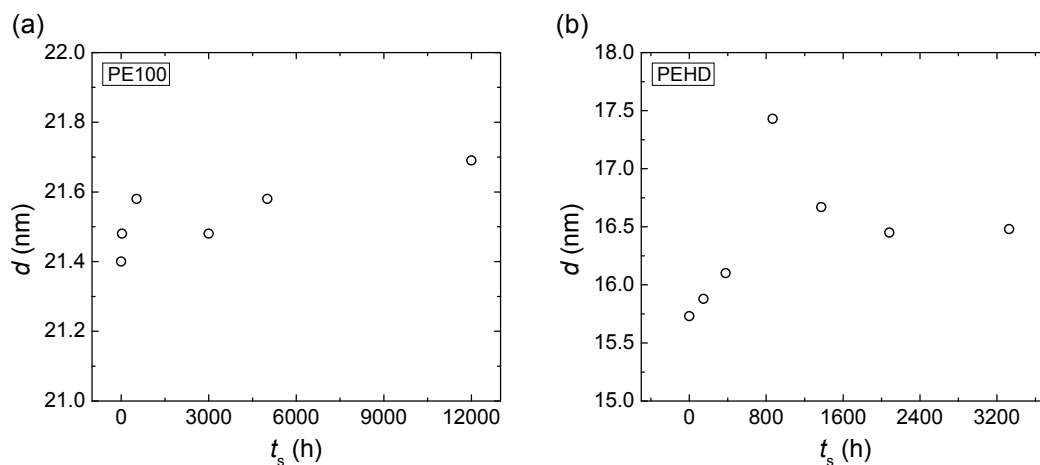


Figure 4.15: Long period versus storage time: (a) PE100 and (b) PEHD.

4.4.6 Hoop Stress Correlation in Stage II Failure – II

Figure 4.16 shows the correlation between σ^{-1} and d of PEHD pipes in stage II failure. The dependence of each phase behaves the same as the phase composition shows in Figure 4.7(b). However, this phenomenon is not observable in stage I failure, neither in PEHD nor in PE100.

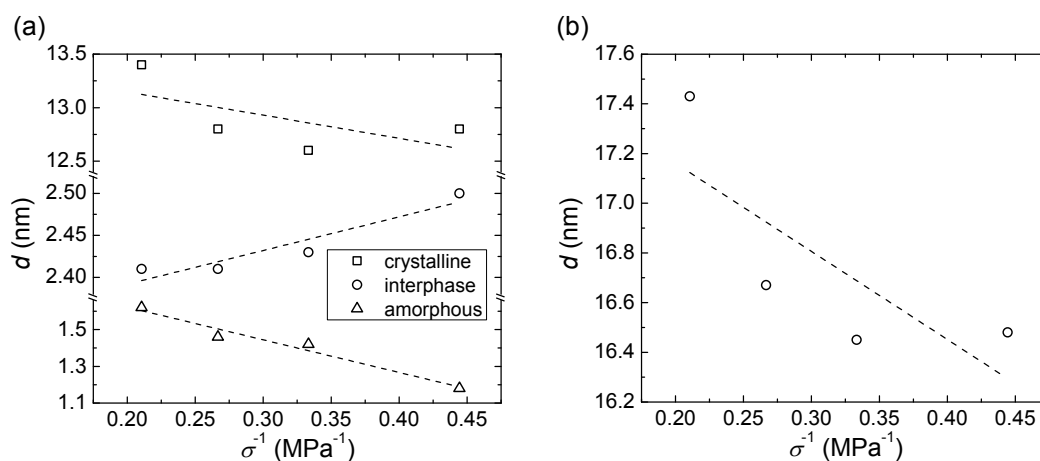


Figure 4.16: Correlation between hoop stress and domain size of PEHD in stage II failure: (a) domain size from different phases, and (b) long period.

4.5 Aging Mechanism

The consistent morphological and molecular dynamical changes due to the hydrostatic pressure test were observed by both DSC and NMR. In this section, based on the above observations the molecular mechanism of the physical aging of HDPE pipes will be presented according to their fracture types.

4.5.1 Annealing and Creep

As demonstrated in Section 3.6.3, due to the processing technology, chain-frozen effect in the noncrystalline region as well as the crystallography flaws in the crystalline region cause the morphology imperfections in HDPE pipes. However, when these pipes are subjected to hydrostatic pressure test at 80 °C, the elevated temperature provides an ideal condition to reinitialize the annealing due to the increasing of the chain mobilities in each phase.^[113] It is well known that annealing can improve the crystal structure, thanks to the migration and the rearrangement of chain segments.^[187] The initial frozen chain segments in the noncrystalline region are released due to the elevated temperature, and the strong segmental crankshaft motions are able to assist the chains to develop into the crystalline phase at the crystal flaw points. Consequently, the phase composition is changed. Annealing is the main reason for the observations in Figure 4.3, Figure 4.4, and Figure 4.14, where both the crystallinity and domain size of the crystalline phase get higher than the fresh pipes for all specimens after the hydrostatic pressure test and, at the same time, those of the interphase decrease.

In addition to the annealing effect, the hydrostatic pressure expose the pipes to a constant stress during the test. This stress induced drawing effect that causes the chain segments in the noncrystalline region to creep and to reorient.^[161,188,189] The subsequent strong elongation reduces the chain entanglement in this region and improves their degree of order. Thus, the conformation diversity and the chain mobility decreases.^[190] This can be proved by the constant T_2 reduction with t_s in all phases as shown in Figure 4.5. T_2 reduction is a sign of the pipe embrittlement, by which the toughness of the material deteriorates and, thus, reduces the pipe's mechanical performance. In fact, annealing also reduces T_2^c

due to the improvement of the crystal structures and, meanwhile, creep assists to improve the chain arrangement at the crystal flaws. In other words, the annealing and creep effects are complementary, they change the morphology and molecular dynamics together under the hydrostatic pressure test condition and, as a result, the softness of the material decreases.

4.5.2 Ductile Fracture versus Brittle Fracture

The hydrostatic pressure test results in Section 4.2.2 show that, according to the testing condition, there are two failure stages observed in PEHD pipes with different fracture types. It is commonly accepted that the ductile failure is induced by the overload of the stress, in which depending on the testing configuration a deformation of as high as 1000% can occur. The brittle fracture happens with a lower stress and little deformation. Lustiger^[191] has explained the molecular mechanisms of HDPE ductile and brittle fracture based on the morphological model in Figure 2.3.

In ductile failure, when the specimens bear under high stress, the “tie” and “loop” molecules between lamellae get stretched with a high deformation. At this stage, the toughness of the material is still high, higher than the adhesive strength between the chain segments in lamellae. Therefore, slips between the chains in the lamellae happen along the ‘*c*’ axis, and resulting the lamellae break into small blocks, which is known as Mosaic blocks.^[192,193] During this process, the creep effect not only elongates the “tie” molecules between lamellae, but also assists those tight “loops” with adjacent re-entry conformation to develop into the crystalline structure, thanks to the reorientation effect. Besides, the formation of Mosaic blocks only reduces the lamella dimension on the plane perpendicular to ‘*c*’ axis, but does not destroy the structure of the long period along the ‘*c*’ axis. Therefore, the domain sizes and long period increase, as shown in Figure 4.14 and Figure 4.15 in stage I failure for both PE100 and PEHD.

However, in the brittle failure with an extremely low stress, the “ties” and “loops” are under a constant tension but without obvious deformations. In such occasion, the chains creep at a low rate which causes the embrittlement of the materials. After a long period of time, chain scissions in the amorphous phase

happen due to oxidation, relaxation, and disentanglement which result in brittle fractures in the planes perpendicular to the ‘ c ’ axis.^[194] These fractures are typical for the stage III failure symbolized by the reduction of \overline{M}_w . However, in stage II failure, due to an intermediate stress, though the fractures are brittle, the molecular mechanism is different and more complicated.

4.5.3 Slow Crack Growth

In stage II failure, the fractures can be explained by slow crack growth (SCG), which is controlled by the macroscopic creep of the material.^[195] Over the last decades, this phenomenon has been studied thoroughly by Brown and coworkers^[148,164,196–199] as well as Barry and Delatycki.^[200,201]

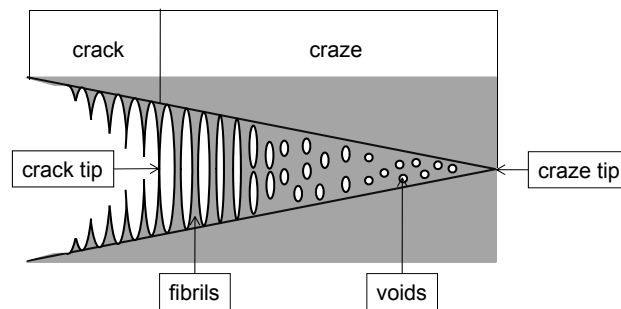


Figure 4.17: Schematic diagram of slow crack growth.

When the material is subjected to constant tension, the stress tends to concentrate to certain points such as the crystal flaws or the catalyst residuals, which are known as stress concentration points. At these points, it is found to yield the voids due to the stress concentration effect, which, subsequently, induce the formation of the crazes. The size of the voids increases with time by merging which, at the same time, creates the fibril structures in the material. Due to the creep effect, fibrils enlarge with time by continuous drawing, and when they eventually reach a limiting draw ratio breakdown occurs via failure. This is the major process of the crack formation, which is well described in Figure 4.17.^[202] However, the fibrils’ breakdown is not induced by chain scissions but the pulling of molecules through the crystalline lamellae as well as molecular disentanglement

4 Study on Aging of HDPE Pipes by Solid-State NMR

in the noncrystalline regions.^[203] Therefore, structure deterioration happens both in the crystalline and the amorphous phases.

Lu and Brown^[150,164,204] have developed an empirical model to estimate t_s when the material failure is dominated by SCG. It is able to describe the structure of the PE which relates to its service time as:

$$t_s = \Omega \Gamma^{-\epsilon} \exp\left(\frac{E_a^s}{RT}\right), \quad (4.5)$$

where Ω is the mechanical resistance of the material against SCG; Γ is the stress intensity which is decided by the geometric factor of the specimen, the global stress surrounding the defects including the residual stress, and the size of the craze where the fractures start; ϵ is a constant for the given material, for PE a $\epsilon = 3$ is widely accepted,^[205] E_a^s is the activation energy of SCG which varies from 85 kJ/mol to 110 kJ/mol depending on the PE class; T is the absolute temperature of the hydrostatic pressure test; and R is the gas constant. So if hydrostatic pressure test condition is set, t_s is rather determined by Ω , the ability of the material to hinder the craze formation and merging under tension. Brown *et al.*^[195] related Ω with the structure of material as:

$$\Omega \propto \frac{f}{d_c} \left(\frac{\delta^{\frac{1}{2}}}{\rho_t}\right)^\iota, \quad (4.6)$$

where f is the fraction of the free “tie” and “loop” molecules, δ is the stress concentrating factor, ρ_t is the density of “tie” and “loop” molecules, ι is a constant and a $\iota = 5$ is accepted for HDPE. In the current case, f is related to the fraction of the noncrystalline phases, and ρ_t is reciprocally related to T_2 . During the hydrostatic pressure test, due to the embrittlement caused by the creep as well as annealing effects the density of noncrystalline region increases, while the amount fraction of it decreases. Besides, d_c is also overall higher than in fresh pipes. Therefore, the decreasing Ω depresses the hinder ability against SCG and the material ends up to final brittle failure.

Furthermore, the changes of w_c as well as d_c in the stage II failure in PEHD pipes are a consequence of a competition between the annealing/creep effects and SCG. During the whole test annealing/creep effects increase w_c and d_c on one side,

while on the other side, the deterioration of crystalline structure caused by SCG reduces w_c and d_c , at the same time. When t_s is short, the annealing/creep effects dominate the morphological change, therefore, as a consequence, increments of w_c as well as d_c are observed. However, when t_s is long enough, the annealing/creep effects reach their saturation, while SCG keeps on continuously and becomes the dominant factor, thus, weaker increments of w_c and d_c based on the value after the annealing/creep effects are observed. This outcome is also supported by the correlation results between hoop stress and phase composition/domain sizes as shown in Figure 4.7 and Figure 4.15. With a high σ , creep is more remarkable due to the stronger drawing effect, while when σ is low the SCG turns to be more obvious due to the constant tensions.

In a word, the reduction of the molecular mobilities due to annealing and creep effects is the main reason for the aging and failure of HDPE pipes. The failure types are determined by the load of stress, i.e. the deformation of the chain segments under drawing, and they will in turn influence the morphology of the material.

4.6 Summary

Aging of HDPE pipes due to hydrostatic pressure and elevated temperature was studied by a combination of DSC and solid-state NMR. According to the applied hydrostatic pressures, two different fracture types were observed, which can be classified as stage I or stage II failure. Morphological and molecular dynamical changes are detected in both stages. The molecular dynamics change more consistently, in which T_2 decreases with t_s in all phases. It is induced by the annealing and creep effects which lead to the embrittlement of the materials, and the embrittlement is the main reason for the stage II failure.

The morphology changes in more complicated ways. For the specimens break in stage I failure, both w_c as well as d_c are higher than that of the fresh pipe, and those of the specimens with a longer testing time increase more remarkably. However, for those that break in stage II failure, though both w_c as well as d_c are also increased, the increments are less obvious. These phenomena are induced

4 Study on Aging of HDPE Pipes by Solid-State NMR

by the synergistic effects of annealing/creep and SCG. The first effect assists the growth of w_c and d_c , while the second one reduces them. In stage I failure, the annealing/creep effect is more remarkable, therefore, w_c and d_c increase obviously, while in stage II failure, due to the embrittlement of the material, SCG becomes more dominant and, consequently, reduces the increment.

Besides, the differences between two different HDPE classes were also observed, morphologically and molecular dynamically. From both DSC and solid-state NMR, w_c of PE100 is about 3~5% higher than PEHD, no matter before or after hydrostatic pressure test. The crystal structure of PE100 is better as a higher T_m as well as a larger d_c were observed. All these indicate the mechanical strength of PE100 is higher. However, as discussed before the higher crystallinity is not always good, as it may increase the brittleness. The superiorities of the PE100 are because of its properties in the interphase and the amorphous phase, i.e. much higher T_2^i and T_2^a than that of PEHD. This indicates the higher chain flexibility and material toughness in these regions which guarantee an excellent Ω against SCG. It is also the reason that even after 12 000 h test at 80 °C, the stage II failure is still not observable in PE100 pipes.

5

Study of MWNT/LDPE Composite by Solid-State NMR

In materials research, polymer nanocomposites have become an interdisciplinary topic which attracts more and more research interests. Extensive investigations have led to revolutionary improvements of the properties of nanocomposites making them better than not only their virgin matrix, but also their conventional microcomposite counterparts. Nowadays, a large group of nanofillers has been well established, for instance, montmorillonite nanolayers, carbon nanotubes (CNT), titanium dioxide nanoparticles, etc. CNT was first reported by Iijima in 1991.^[206] Thanks to its remarkable mechanical, thermal, and electrical properties,^[207–210] it has been nominated as one of the most outstanding candidates for the modification of different polymer materials since the successful preparation of CNT/polymer nanocomposite by Ajayan *et al.*^[211] in 1994.

CNT/polymer nanocomposites have shown significant improvements of the material in diversified aspects, e.g. mechanical strength, thermal stability, rheological behavior, electrical property, flame retardancy, etc. Depending on the targeting properties, these materials cover wide application fields ranging from ultrastrong fibers for bullet-proof vests, flexible displays to electronic paper, etc.^[212] Up to now, great success has been achieved by hybridizing CNT with various thermoplastic polymers, for instance, amorphous rigid polystyrene, thermal plastic elastomer polyurethane, semicrystalline PE and PP, crosslinkable epoxy, etc.

5 Study of MWNT/LDPE Composite by Solid-State NMR

Among all, the investigation of CNT/PE nanocomposite has been carried out most intensively over the last years and has contributed to great progresses in this field including preparation^[213–222] and characterization.^[223–230] Besides, the theoretical and simulative studies concerning these materials also helped to understand the fundamentals of the nanocomposite effectively.^[231–234]

However, in order to develop CNT/PE as a candidate for wide applications, some remaining complex issues still need to be completely understood, for example, the dispersion of the CNTs in the PE matrix as well as the interfacial interactions between them. These issues not only influence the mechanical properties of the nanocomposites but also their thermal stability. In this context, solid-state NMR plays an important role. It is able to provide detailed information on nanocomposites and, thus, to describe the interactions between polymer matrix and nanofiller.^[43,99,235,236] In the present work, morphology and molecular dynamics of LDPE filled with multi-wall nanotubes (MWNT) were investigated by DSC and solid-state NMR, based on which, the reason of the change of the thermal stability and the mechanical properties of the nanocomposite will be discussed on a molecular level.

5.1 Materials

MWNT/LDPE nanocomposite was prepared and kindly donated by Institut für Angewandte Polymerchemie (IAP), Fachhochschule Aachen, Germany. Both MWNT and LDPE were used as received without any modification. All the samples were prepared by a mini extruder with identical parameters, thus, both the mechanical and thermal histories of them are uniform. In the current study, five samples with different MWNT loading from 0.1% to 5% were used for the investigation. Besides, the neat LDPE was also studied as a reference.

5.2 Thermal Properties

Thermal properties are important for material application, and the improvement of the thermal stability is one of the key pursuing objects for the development

of new high performance materials. Conventionally, thermal decomposition evaluated by thermogravimetric analysis (TGA) is the most widely used method to investigate the thermal properties of polymer materials.^[237,238]

5.2.1 TGA Measurement

Thermal decomposition of MWNT/LDPE composites was studied by NETZSCH TG 209 apparatus. All samples including the neat LDPE were analyzed in a temperature range of 200 °C to 800 °C and a heating rate of 10 °C/min. A nitrogen gas flow rate of 10 cm³/min was applied to create the inert atmosphere so as to prevent the oxidations. In order to eliminate the errors caused by the moisture in the polymer matrix, all the samples were first stabilized at 200 °C until they reach a weight constant stage and, after that, the temperature program is applied.

5.2.2 Thermal Stability and Decomposition

The thermal decomposition behavior of neat LDPE and MWNT/LDPE composite is displayed in Figure 5.1. The total MWNT loadings are low and the difference between the samples is very small. Therefore, in order to have a better observation, only the sample with 5% MWNT and the neat LDPE are presented. For temperatures between 200 °C and 400 °C, the weights of both specimens stay constant at 100%. This indicates the moisture in the specimen has been removed completely before the temperature programming. For temperatures between 400 °C and 550 °C, the MWNT/LDPE shows a shift of thermal decomposition trace to higher temperatures than that of the neat LDPE, which reflects a higher thermal stability. Besides, the different residual masses (m_r) after complete decomposition correlate with the MWNT loading amount.

Table 5.1 presents the detailed information about the thermal decomposition of the MWNT/LDPE composites. m_r increases with the MWNT amount accordingly. However, a systematic deviation of m_r ¹ from the actual MWNT loading

¹The residual mass is on average 0.8% higher than the actual MWNT amount. This may be caused by the undecomposable impurities in the polymer matrix. These impurities influence the mechanical properties of the material as they could act as stress concentration points as explained in Section 4.5.3.

5 Study of MWNT/LDPE Composite by Solid-State NMR

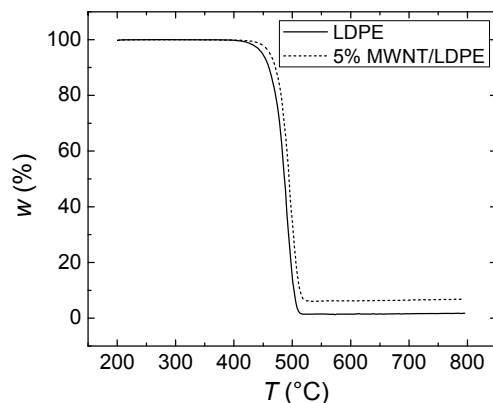


Figure 5.1: TGA traces of LDPE and MWNT/LDPE composite.

Table 5.1: Thermal decomposition parameters of MWNT/LDPE composites determined by TGA.

MWNT %	T_{onset} °C	$T_{\text{inflection}}$ °C	T_{end} °C	m_r %
0	471.3	481.5	498.4	0.74
0.1	469.8	491.9	504.6	1.34
0.5	470.1	493.9	506.4	1.66
1.0	465.4	495.6	505.0	1.98
2.0	469.5	492.7	504.9	2.63
5.0	480.4	493.8	506.1	5.58

amount is observed. The decomposition onset temperature (T_{onset}) is around 470 °C for both neat LDPE and nanocomposites, except the one with the highest MWNT amount of 5%, where a 10 °C higher T_{onset} was observed. The inflection temperature ($T_{\text{inflection}}$) is the point with the highest weight loss rate observed in the TGA traces. It is a key parameter which reflects the thermal stability of the nanocomposites. The result shows that $T_{\text{inflection}}$ increases significantly even with only 0.1% MWNT loading. However, among the nanocomposites the different MWNT amounts seems not to affect $T_{\text{inflection}}$ obviously. The decomposition end

temperature (T_{end}) shows the same behavior as $T_{\text{inflection}}$, in which only the differences between neat LDPE and nanocomposites are observable. All the specific temperatures extracted from the TGA traces indicate that by loading MWNT the thermal stability of LDPE matrix is enhanced and the specimen with the highest loading (5% MWNT) shows the most remarkable improvement.

5.3 Morphology and Molecular Relaxation

The changes of the physical properties are closely related to the morphology and molecular dynamics of the polymer matrix. Therefore, the study of phase composition, crystal lamella thickness, as well as the molecular relaxations is important. It is able to explain the physical performance of LDPE with the presence of MWNT based on the above information.

5.3.1 ^1H FID and DSC Measurement

The melting and latent behavior were evaluated by DSC. The same hardware and parameters as described in Section 4.3.1 were applied. Only the first heating up and melting scans were taken.

^1H transverse relaxation was investigated by the FIDs after single 90° pulse. Both the hardware and general parameters are the same as described in Section 4.3.1, except the sample temperature. In the current study, the optimized sample temperature of 70°C ¹ was applied to evaluate the molecular relaxation of the solid MWNT/LDPE composites.

5.3.2 Crystallinity Determined by DSC

Table 5.2 shows the w_c , T_m , and T_c determined by DSC. Both w_c and T_m decrease with increasing MWNT amount. For the 5% MWNT sample, the decrements of about 12.5% for w_c and 2% for T_m were observed. T_c behaves differently, it increases remarkably by loading even 0.1% MWNT. However, the T_c difference among nanocomposites is not obvious.

¹Appendix A and Appendix B

5 Study of MWNT/LDPE Composite by Solid-State NMR

Table 5.2: Crystallinity, melting temperature, and crystallization temperature of LDPE nanocomposite with different MWNT amounts determined by DSC.

MWNT %	T_c °C	T_m °C	w_c %
0	90.2	113.1	36.5
0.1	93.3	112.4	35.7
0.5	93.9	111.7	34.3
1.0	93.7	111.6	34.1
2.0	92.9	111.3	33.5
5.0	93.0	110.8	31.8

5.3.3 Lamella Thickness

Lauritzen and Hoffman^[239] as well as Wunderlich *et al.*^[240] have introduced the thermodynamic formula to semicrystalline polymers according to their melting behavior evaluated by DSC. It is able to estimate the crystal lamella thickness based on Δh_m and T_m , as:

$$L_c = \frac{2\sigma_e}{\rho_{cm}\Delta h_m^0} \frac{T_m^0}{T_m^0 - T_m}, \quad (5.1)$$

where L_c is the lamella thickness, σ_e is the average energy on the chain folding surface, T_m^0 is the melting temperature of 100% crystal, and ρ_{cm} is the crystal density. In order to apply this equation to MWNT/LDPE composite, some hypotheses are indispensable. For example, it is supposed that the presence of MWNT does not change the latent habit as well as the chain folding behavior of LDPE in the crystalline phase. Therefore, the previous values of $\Delta h_m^0 = 293 \text{ J/g}$ ^[111,112] as well as $\sigma_e \approx 77 \text{ erg/cm}^2$ to 96 erg/cm^2 ^[240-242] for PE are valid in our situation, and the arithmetic average value of 86 erg/cm^2 for σ_e was applied in this work. Besides, the density of the crystalline phase is not influenced by MWNT either, and $\rho_{cm} = 0.99 \text{ g/cm}^3$ ^[185] was used, currently.

5.3 Morphology and Molecular Relaxation

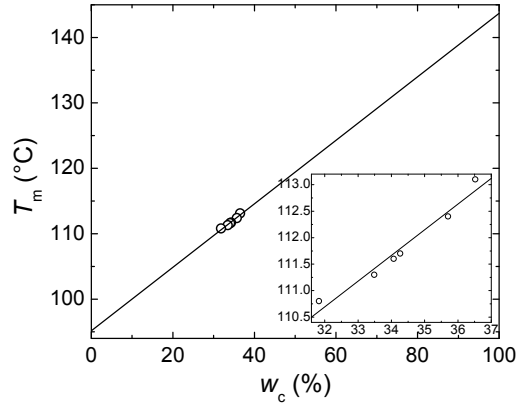


Figure 5.2: Correlation between melting temperature and crystallinity.

Figure 5.2 shows the correlation between T_m and w_c . The inserted figure illustrates the linear relationship. By extrapolating T_m to $w_c = 100\%$, a $T_m^0 = 143.7^\circ\text{C}$ is obtained. This value perfectly meets the previously reported T_m^0 of PE as $141\sim 143.5^\circ\text{C}$.^[242–244] Therefore, the assumptions mentioned above are valid, and the lamella thickness can be estimated by Equation 5.1 with the available parameters.

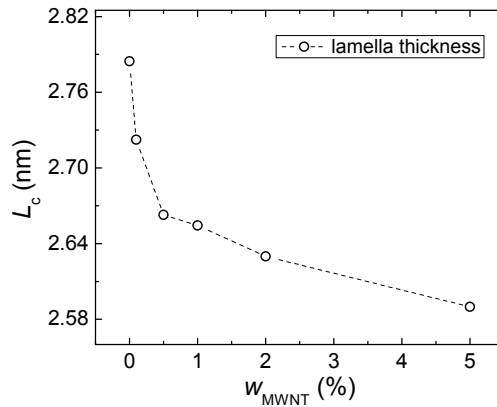


Figure 5.3: Lamella thickness of MWNT/LDPE nanocomposite.

Figure 5.3 presents the lamella thickness of MWNT/LDPE nanocomposites. The size is between 2.55 nm and 2.80 nm, it decreases in an analogous exponential decay manner with increasing MWNT amount. This indicates the presence of MWNT influences the morphology significantly, even with only 0.1% loading.

5.3.4 Phase Composition Determined by ^1H FID

Figure 5.4 depicts the phase composition determined by ^1H FID at 70°C . Three components are observed with different behavior according to the change of MWNT amount. In the crystalline phase, the same decreasing behavior of w_c as determined by DSC is observed, and the values are systematically 10% higher. However, the decrement is less obvious than that observed by DSC, only a 10% reduction was observed for the 5% MWNT sample. At the same time, both the amount of the interphase and the amorphous phase increase with the loading of MWNT and the increment is more obvious in the amorphous phase.

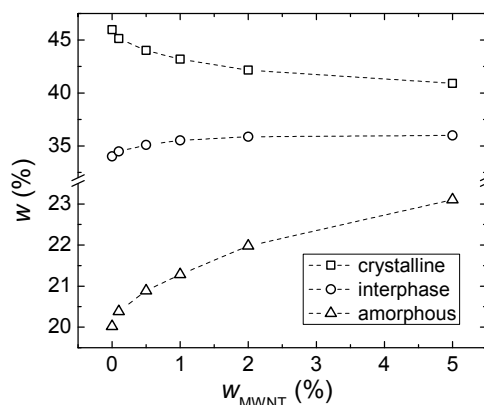


Figure 5.4: Phase composition of LDPE nanocomposite with different MWNT amounts determined by ^1H FID at 70°C .

5.3.5 Transverse Relaxation Times of Solid Composite

Figure 5.5 shows T_2 of different phases determined by ^1H FID at 70°C . Both T_2^a and T_2^i decrease with increasing MWNT amount. The decrement is more remarkable in amorphous phase, where an about 50% reduction is observed from the neat LDPE to 5% MWNT/LDPE composite, while it is only about 15% for T_2^i . It indicates that the presence of MWNT in the LDPE matrix reduces the chain mobilities both in the interphase and in the amorphous phase, and the reduction gets more significant with increasing MWNT amount. On the other side, T_2^c of the crystalline phase is almost constant. It supports the assumption

5.3 Morphology and Molecular Relaxation

that the presence of MWNT does not change the chain folding behavior in this region and also validate the lamella thickness calculation in Section 5.3.3.

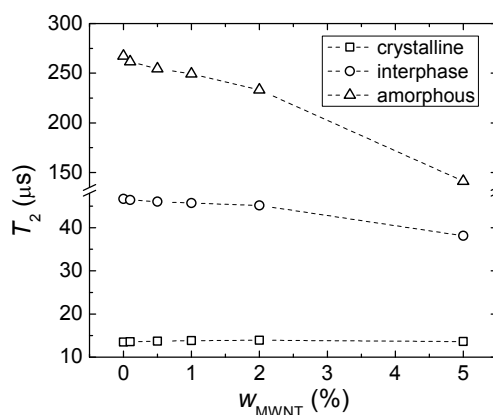


Figure 5.5: Transverse relaxation times of LDPE nanocomposite with different MWNT amounts determined by ^1H FID at 70°C .

Both the thermal and mechanical histories of the nanocomposites are identical, however, the morphological difference between the samples with different MWNT amounts was observed. This is most probably induced by the change of crystallization kinetics in the presence of MWNT during the extrusion. Crystallization kinetics are strongly related to the chain mobilities of the polymer melts during the cooling process. In order to understand this issue, it is necessarily to learn the molecular dynamics of the nanocomposite melts. To meet such end, the sample probing temperature was increased to 120°C to investigate the transverse relaxation of the MWNT/LDPE composite melts by ^1H FID.

5.3.6 Transverse Relaxation Time of Composite Melt

Figure 5.6 shows the ^1H FIDs of MWNT/LDPE composite melts measured at 120°C . In Figure 5.6(a), with increasing MWNT amount, the magnetization decays faster, especially the one with 5% MWNT. Figure 5.6(b) shows the initial parts of the decays in half logarithmic scale on the ordinate axis. The signals display a linear or approximate linear relation between $\lg I(t)/I(0)$ and t , which indicates the polymer chains relax isotropically in the melts, and also illustrates

5 Study of MWNT/LDPE Composite by Solid-State NMR

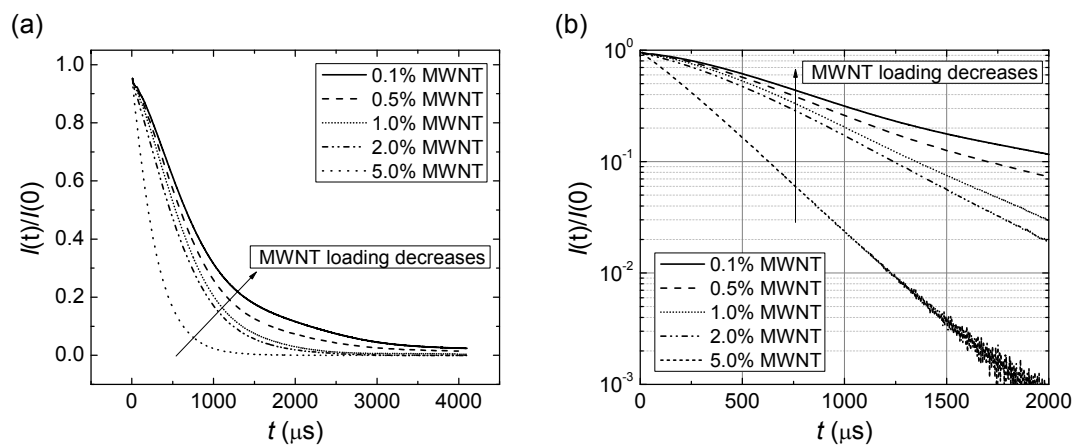


Figure 5.6: ^1H FID of LDPE nanocomposite melt with different MWNT amounts measured at 120°C : (a) in linear coordinates, and (b) in half logarithmic ordinates.

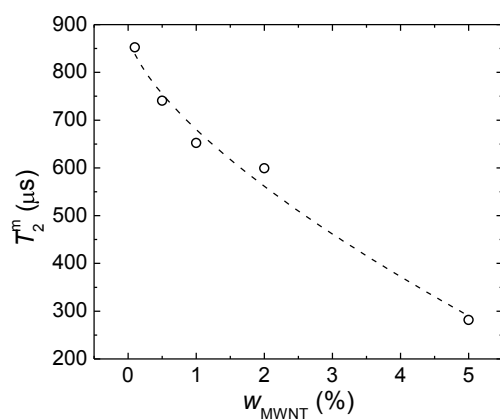


Figure 5.7: Transverse relaxation time of LDPE nanocomposite melts with different MWNT amounts determined by ^1H FID at 120°C .

MWNTs disperse homogeneously in the polymer matrix. Therefore, one exponential decay function is applied to describe the transverse relaxation for all samples. Figure 5.7 depicts the transverse relaxation times of the MWNT/LDPE melts (T_2^m). T_2^m decreases with increasing MWNT. It indicates the chain mobilities reduce in the LDPE melts which is caused by the chain confinement effect induced by the presence of MWNTs, and this effect increases with the increasing MWNT loading amount.

5.4 ^1H Residual Dipolar Coupling by Double-Quantum NMR

Due to the presence of MWNT in LDPE matrix, w_c and L_c decrease, while the amounts of the other two phases increase. The transverse relaxation times of both solid as well as the molten LDPE matrices reduce thanks to the chain confinement by MWNTs. However, the molecular mechanism behind the phenomena is still not clear. In order to understand this part, the study of the molecular interactions in each phase is necessary. ^1H double-quantum NMR is an advanced technique able to investigate the ^1H intra- and intermolecular interactions by looking into the dipolar couplings and, consequently, assistances to figure out the material physical performance on a molecular level.

5.4 ^1H Residual Dipolar Coupling by Double-Quantum NMR

^1H residual dipolar coupling (D_{res}) provides key information about the structure and molecular dynamics of polymer. It is able to reflect the influence of the chain confinement on their nonisotropic motions due to the presence of inorganic fillers in the polymer matrix.^[245–247] Different NMR methods can be applied to estimate D_{res} , such as the Hahn echo and solid echo relaxation measurements.^[248–251] However, the data analysis of these methods is not a trivial issue, errors occur easily if the data are overinterpreted.^[252–255] On the other hand, ^1H double-quantum buildup and decay curves which were first performed by Pines *et al.*^[256,257] in solid-state offer a convenient solution to access D_{res} and the molecular dynamics in a model-free manner.^[246,254,258–260] These double-quantum curves measured in the initial regime of the excitation/reconversion periods are able to provide the information of specific residual second van Vleck moment (M_2).^[261] They also provide information about the interactions between fillers and polymer matrices, as well as the polymer chain confinements.

5.4.1 Dipolar Filter

As described in Section 2.3, NMR signals deal with the transition of the spins between different energy levels in a magnetic field. When the system involves

5 Study of MWNT/LDPE Composite by Solid-State NMR

the coupling between two neighboring spins $\frac{1}{2}$, according to the spin states, four different combinations are possible which generate four different energy levels, as shown in Figure 5.8(a). There are two possible transition routes from the lowest to the highest energy level as marked with solid and dashed arrows.¹ In a homonuclear spin $\frac{1}{2}$ system, the energy levels in the middle are about the same at high-field which makes the two routes identical. When one of the spins in the spin pair flips, the energy level transition is called single quantum coherence, while if both spins flip, i.e. the energy level changes from level 1 to level 3, the transition is called double-quantum coherence. By applying a dipolar filter, double-quantum NMR is able to encode the energy transitions of the spin pairs and, thus, to extract the coupling information between the spins.

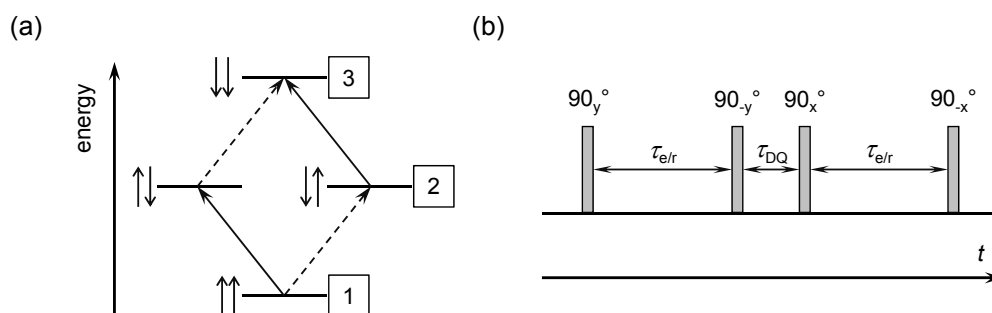


Figure 5.8: (a) Energy levels in a two-spin $\frac{1}{2}$ system. (b) Double-quantum dipolar filter.

The basic double-quantum pulse sequence is the same as described in Section 4.4.1 Figure 4.9. However, instead of the spin-diffusion, the most important part here is the dipolar filter, as shown in Figure 5.8(b). With the application of the first two 90° pulses a double-quantum coherence is excited. Subsequently, a time interval of τ_{DQ} is involved and after that with the third and fourth 90° pulses, the spin double-quantum coherence is converted back into non-equilibrium population differences, which are, subsequently, probed by transverse magnetization with the execution of the fifth 90° pulse. In a double-quantum NMR measurement, the varying list of $\tau_{e/r}$ enables the dipolar filter to encode different molecular inter-

¹The double-quantum energy level transitions are combined by one solid arrow and one dashed arrow.

5.4 ^1H Residual Dipolar Coupling by Double-Quantum NMR

actions according to their different coupling strength. The quantum mechanism behind the dipolar filter and the double-quantum pulse sequence is very complicated, for more detailed information previous work and the references there are recommended. [27,98,262–267]

5.4.2 Double-Quantum Measurement

In order to investigate the ^1H residual dipolar couplings of MWNT/LDPE composite from different phases, a modified pulse sequence based on the standard double-quantum pulse sequence was developed, as shown in Figure 5.9. [256] It is able to select the coupling information from different phases depending on their different relaxation behavior. Before the application of the dipolar filter, another two 90° pulses that act as a phase selection filter were incorporated, in which τ_r is the phase selection period and τ_i is the time interval between phase selection filter and dipolar filter. With a short τ_r , the transverse relaxation effects in all phases are small which enables the dipolar filter to excite the double-quantum coherence in the crystalline phase at short $\tau_{e/r}$. In this case, the modified pulse sequence provides the same information as a standard double-quantum pulse sequence. However, when τ_r is long, due to the fast transverse relaxation in the crystalline phase and in the interphase, the magnetization from these two phases is no longer detectable and, therefore, only the couplings from the amorphous phase are selected.

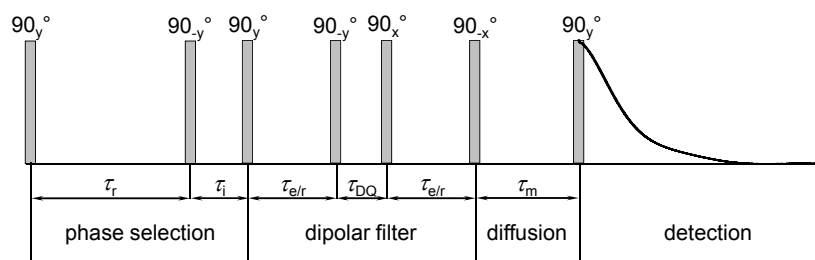


Figure 5.9: Double-quantum pulse sequence with a phase selection filter.

In the present work, ^1H static double-quantum measurements were carried out on a 500 MHz NMR spectrometer by applying a high power MAS probe body with

5 Study of MWNT/LDPE Composite by Solid-State NMR

a 4 mm coil. The optimized sample temperature was 70 °C and the optimized 90° rf pulse was 4 μ s. For PE, the optimum fixed time intervals between the pulses are $\tau_{\text{DQ}} = \tau_{\text{m}} = 5 \mu\text{s}$ and $\tau_{\text{i}} = 3 \mu\text{s}$. In order to select the best signals, different τ_{r} s were used for different phases for the nanocomposites with different MWNT amounts. For instance, for neat LDPE, $\tau_{\text{r}} = 3 \mu\text{s}$ for the crystalline phase, $\tau_{\text{r}} = 40 \mu\text{s}$ for the interphase, and $\tau_{\text{r}} = 190 \mu\text{s}$ for the amorphous phase were applied, respectively. Besides, due to the different responses to the dipolar filter, different varying lists of $\tau_{\text{e/r}}$ were applied for each specific phase.

5.4.3 Double-Quantum Curves

Figures 5.10 to Figures 5.12 display the ^1H broad line spectra of neat LDPE recorded by the pulse sequence, as indicated in Figure 5.9, with different τ_{r} s and different varying lists of $\tau_{\text{e/r}}$. In order to have a better comparison between the signals, the abscissa and ordinate axes in all subfigures are identical. For $\tau_{\text{r}} = 3 \mu\text{s}$, as shown in Figure 5.10, the phase selection filter keeps the signals from all phases and allows the dipolar filter encoding the magnetization in the crystalline phase. In this case, for short $\tau_{\text{e/r}}$, as shown in Figure 5.10(a) and Figure 5.10(b), the recorded spectra are very broad with two doublet peaks. This is a typical style for the two spins from the same methylene group in the crystalline phase with very strong dipolar couplings.^[13,38] At longer $\tau_{\text{e/r}}$, as shown in Figure 5.10(c) and Figure 5.10(d), the spectral line width narrows down. In this stage, the signals are mainly from the interphase. When $\tau_{\text{e/r}}$ is long enough, due to transverse relaxation, the spin dipolar couplings from both the crystalline phase and the interphase are undetectable, and the signals come only from the amorphous phase.^[24] Therefore, as shown in Figure 5.10(e) and Figure 5.10(f), the line widths are very narrow and the signal decays with increasing $\tau_{\text{e/r}}$.

For $\tau_{\text{r}} = 40 \mu\text{s}$, as shown in Figure 5.11, the phase selection period filters out the signals from the crystalline phase. Thus, the dipolar filter can only encode the magnetization from the interphase at short $\tau_{\text{e/r}}$. Here weaker doublet peak signals are observed with $\tau_{\text{e/r}}$ shorter than 13 μs . By increasing $\tau_{\text{e/r}}$, the dipolar filter transfers the signal encoding from the interphase to the amorphous phase, which can be told from the narrowing of line width.

5.4 ^1H Residual Dipolar Coupling by Double-Quantum NMR

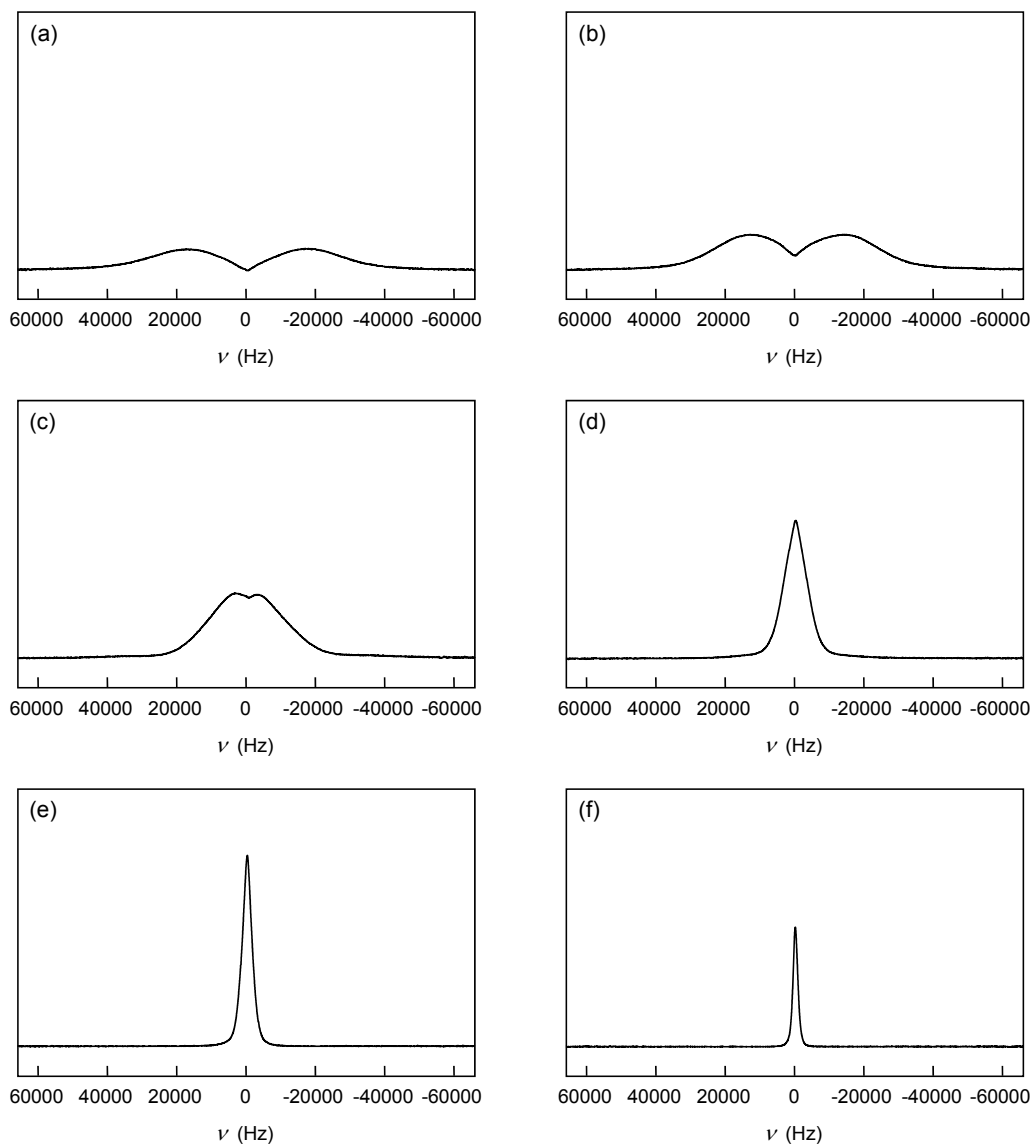


Figure 5.10: ^1H double-quantum spectra with a phase selection period of $\tau_r = 3 \mu\text{s}$ and different excitation/reconversion times in double-quantum dipolar filter: (a) $\tau_{e/r} = 3.5 \mu\text{s}$, (b) $\tau_{e/r} = 8 \mu\text{s}$, (c) $\tau_{e/r} = 18 \mu\text{s}$, (d) $\tau_{e/r} = 50 \mu\text{s}$, (e) $\tau_{e/r} = 120 \mu\text{s}$, and (f) $\tau_{e/r} = 300 \mu\text{s}$.

Figure 5.12 depicts the double-quantum spectra recorded at $\tau_r = 190 \mu\text{s}$. Here only narrow lines are observable, which indicates the signals from the interphase are also filtered out and the dipolar filter can only encode the couplings from the amorphous phase. In the current study, if increase τ_r to more than $350 \mu\text{s}$,

5 Study of MWNT/LDPE Composite by Solid-State NMR

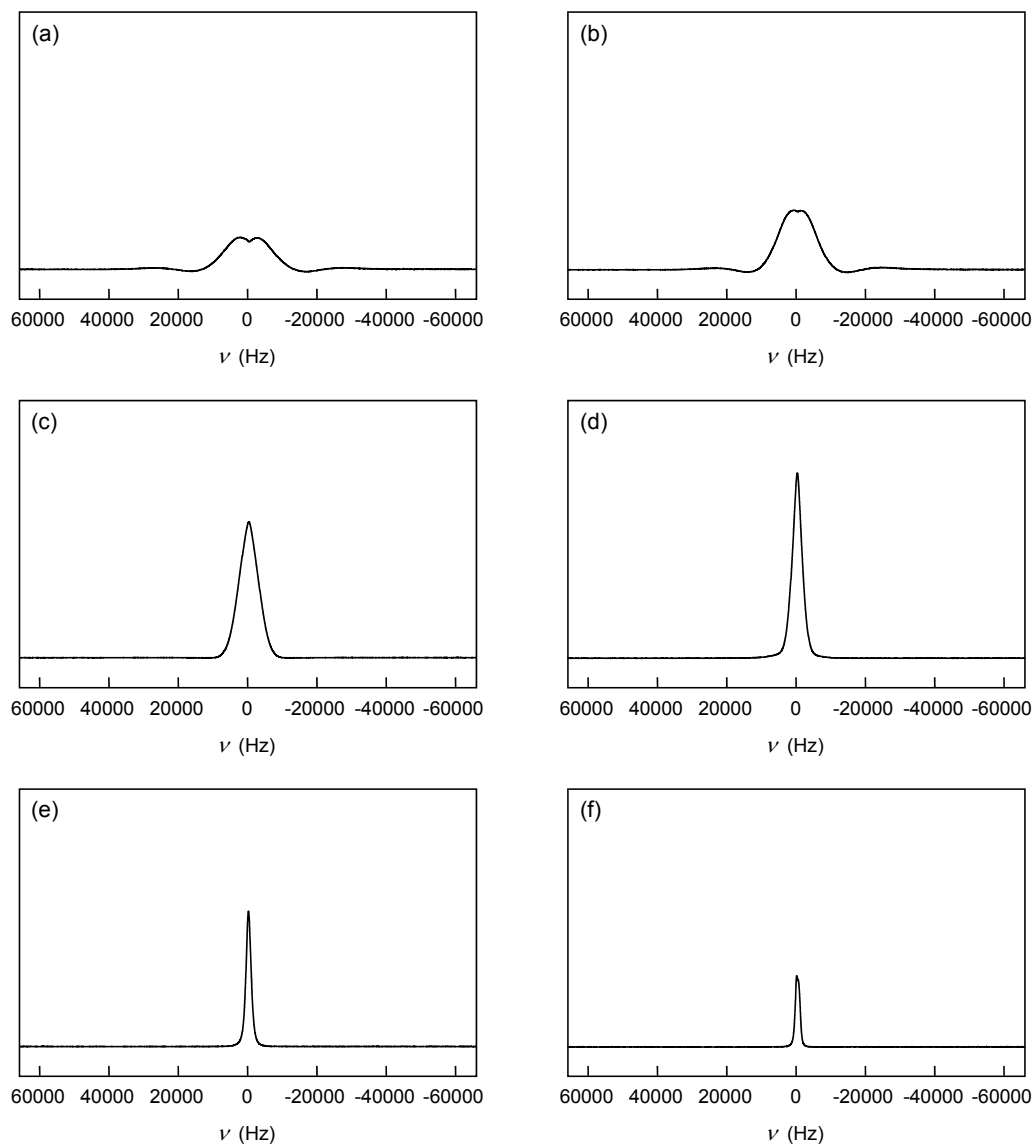


Figure 5.11: ^1H double-quantum spectra with a phase selection period of $\tau_r = 40 \mu\text{s}$ and different excitation/reconversion times in double-quantum dipolar filter: (a) $\tau_{e/r} = 5 \mu\text{s}$, (b) $\tau_{e/r} = 13 \mu\text{s}$, (c) $\tau_{e/r} = 40 \mu\text{s}$, (d) $\tau_{e/r} = 100 \mu\text{s}$, (e) $\tau_{e/r} = 250 \mu\text{s}$, and (f) $\tau_{e/r} = 500 \mu\text{s}$.

the magnetization from all phases decays completely during the phase selection period, and no signal was detectable after the dipolar filter.

According to the above results, it is clear that by applying the phase selection filter, the signals from various phases are highlighted, and based on which the

5.4 ^1H Residual Dipolar Coupling by Double-Quantum NMR

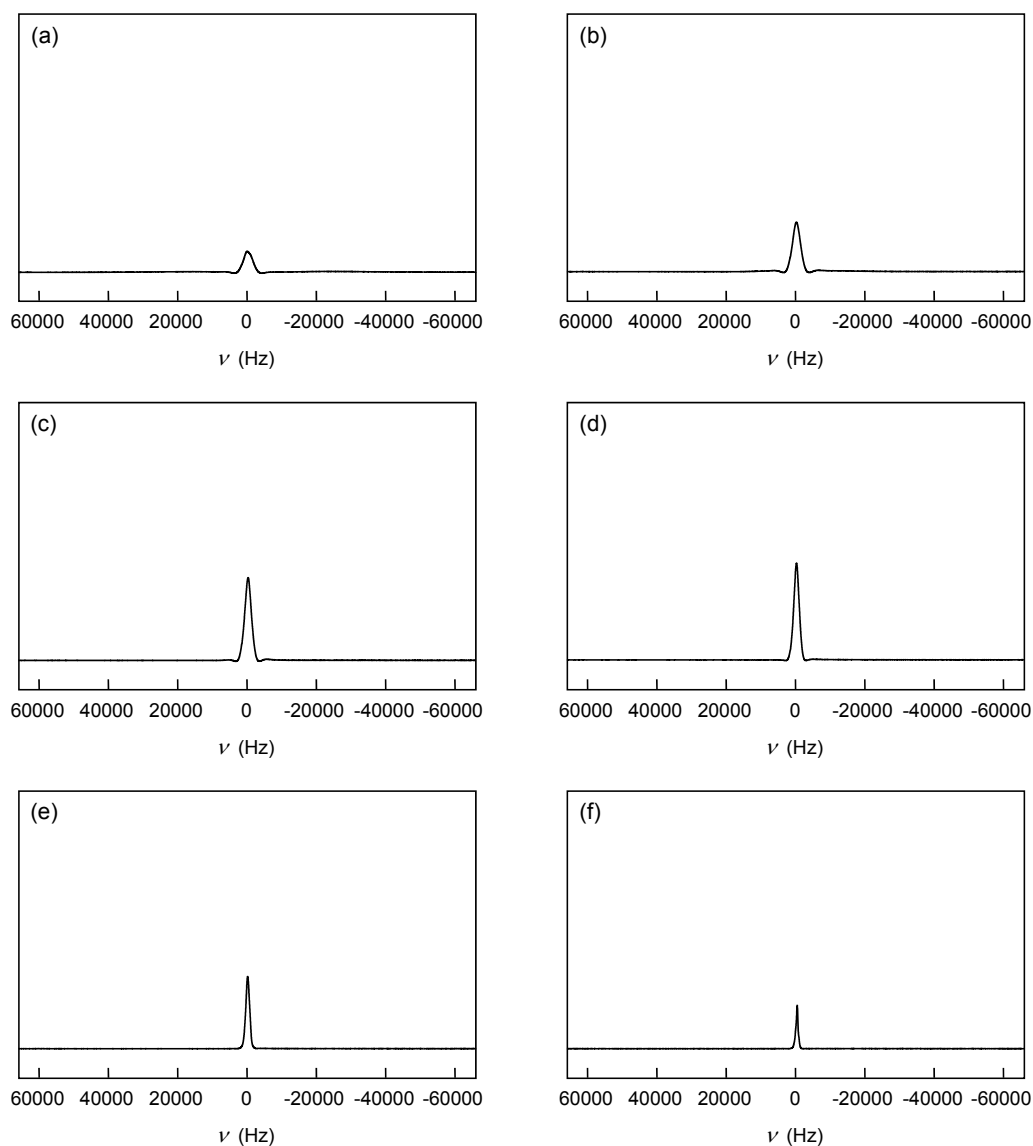


Figure 5.12: ^1H double-quantum spectra with a phase selection period of $\tau_r = 190 \mu\text{s}$ and different excitation/reconversion times in double-quantum dipolar filter: (a) $\tau_{e/r} = 7 \mu\text{s}$, (b) $\tau_{e/r} = 24 \mu\text{s}$, (c) $\tau_{e/r} = 55 \mu\text{s}$, (d) $\tau_{e/r} = 110 \mu\text{s}$, (e) $\tau_{e/r} = 250 \mu\text{s}$, and (f) $\tau_{e/r} = 1000 \mu\text{s}$.

^1H dipolar couplings from each phase can be studied. Figure 5.13 presents the double-quantum buildup curves of neat LDPE recorded at different τ_r s. The signal of each spectrum was normalized to the ^1H broad line recorded after a single 90° pulse with corresponding dead time of $t_d = \tau_r$. For instance, a FID of $t_d = 190 \mu\text{s}$

5 Study of MWNT/LDPE Composite by Solid-State NMR

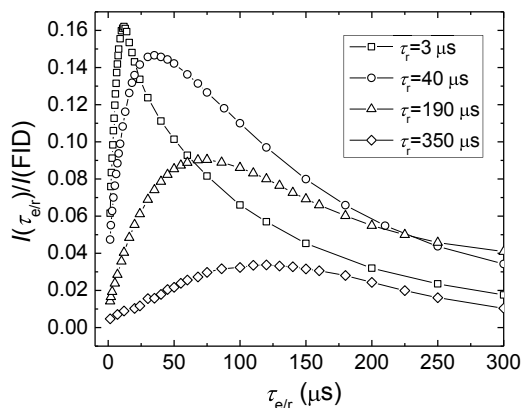


Figure 5.13: Double-quantum buildup curves of LDPE as a function of excitation/reconversion time recorded with different phase selection times.

was recorded for the normalization of the double-quantum curve measured at $\tau_r = 190 \mu\text{s}$. For $\tau_r = 3 \mu\text{s}$, the buildup curve reaches the maximum signal at $\tau_{e/r} = 12 \mu\text{s}$. Here the normalized signal intensity is about 16.5% and after that the intensity starts to decay. This is a typical PE double-quantum curve, in which the intramethylene ^1H dipolar couplings in the crystalline phase are emphasized. For $\tau_r = 40 \mu\text{s}$, the maximum signal shifts to a higher $\tau_{e/r}$ of $35 \mu\text{s}$ and, at the same time, the normalized signal reduces to 14%. In this stage, the dipolar filter encodes the couplings in the interphase. For $\tau_r = 190 \mu\text{s}$, the signals from both the crystalline and the interphase have been filtered out. The double-quantum curves is, therefore, featured by a slow buildup rate and low intensity, in which the maximum normalized intensity of 9% was observed at $\tau_{e/r} = 75 \mu\text{s}$.

Figure 5.14 presents the normalized double-quantum curves from different phases of LDPE and the nanocomposites. Figure 5.14(a) shows the signals from the crystalline phase. The difference between samples is not obvious: all the signals reach the maximum intensity of about 16% at $\tau_{e/r} = 12 \mu\text{s}$, except for the sample with 5% MWNT, in which the maximum intensity is relatively low. The same behavior is observed in the interphase, as shown in Figure 5.14(b). The only difference compared to that from the crystalline phase is the maximums shift to $\tau_{e/r} = 35 \mu\text{s}$ with around 14% normalized intensity. However, for the amorphous phase, the difference between the samples is obvious, as shown in Figure 5.14(c). First, the maximum intensity increases with increasing MWNT amount: only

5.4 ^1H Residual Dipolar Coupling by Double-Quantum NMR

about 9% normalized signal is observed for the neat LDPE, while it increases to about 12% for the nanocomposite with 5% MWNT. Second, $\tau_{e/r}$ for the highest signal intensity also shifts to lower values: for neat LDPE it is at $\tau_{e/r} \approx 75 \mu\text{s}$, while it shifts to about $68 \mu\text{s}$ for 5% MWNT composite.

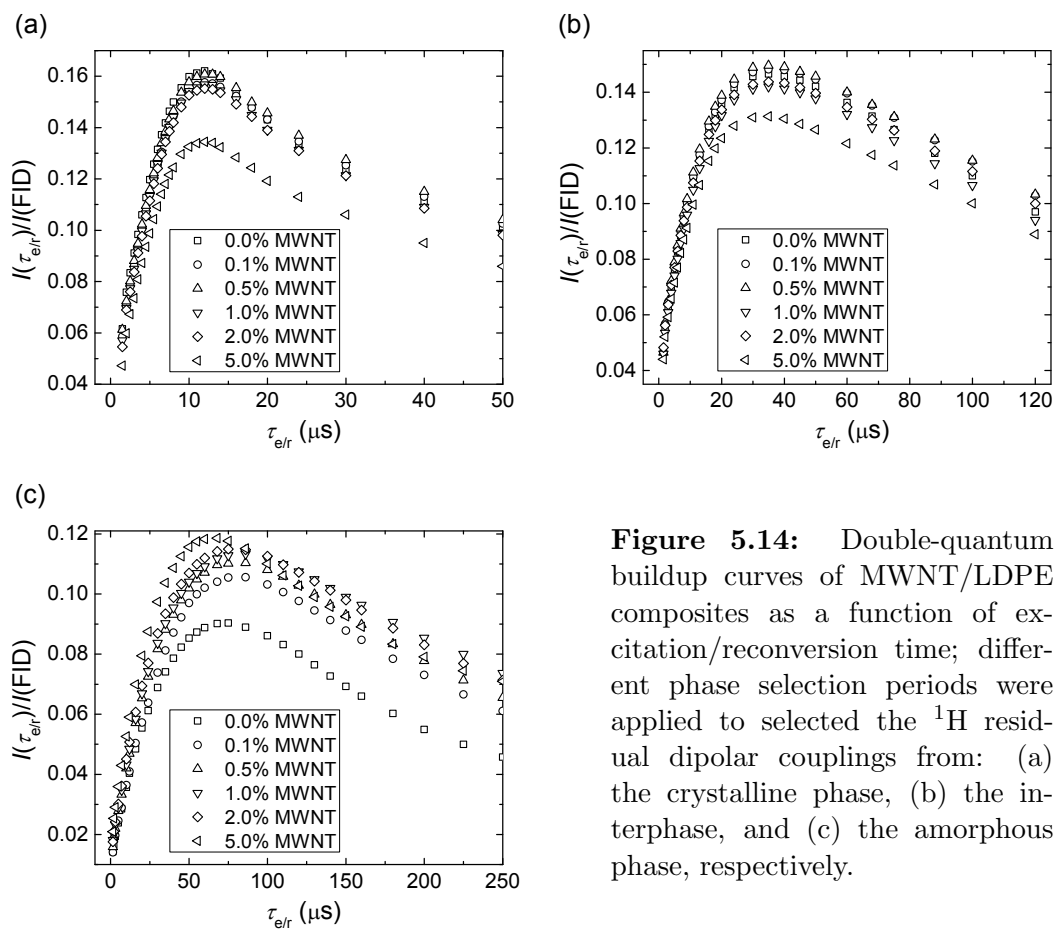


Figure 5.14: Double-quantum buildup curves of MWNT/LDPE composites as a function of excitation/reconversion time; different phase selection periods were applied to selected the ^1H residual dipolar couplings from: (a) the crystalline phase, (b) the interphase, and (c) the amorphous phase, respectively.

All the above results illustrate that the amplitude of the double-quantum curves is related to the relaxation times. For different phases, the highest double-quantum normalized signal was detected in the crystalline phase with the shortest T_2 , while the lowest signal is detected in the amorphous phase with the longest T_2 . Besides, the amplitude difference of the amorphous phase among the nanocomposites is also observed, which also fulfills the above rule, i.e. the shorter T_2 shows the higher double-quantum amplitude. This is caused by the incomplete averaging of spatially anisotropic dipolar couplings, also known as residual dipole-

5 Study of MWNT/LDPE Composite by Solid-State NMR

lar coupling. It is able to reflect the angular diversity of the spins which in turn illustrates the molecular mobilities of the spins.

5.4.4 Residual Dipolar Coupling

By interpreting double-quantum buildup curves, rich information about molecular dynamics can be obtained in terms of D_{res} and M_2 . However, up to now, there is no precise analytical solution able to fit the double-quantum curves in the whole $\tau_{e/r}$ range. For instance, Saalwächter *et al.*^[268,269] assumed a Gaussian distribution of double-quantum signals with $\tau_{e/r}$ and introduced a fit model which is able to extract D_{res} for elastomer networks. However, an as high as 50% standard fit deviation that may impose significant errors on D_{res} has to be taken into consideration.^[247,270]

Blümich *et al.*^[261,271] demonstrated that for signals at short $\tau_{e/r}$ region, the double-quantum buildups can be well described by polynomial functions with a T_2 correction as:

$$\begin{aligned} S_{\text{DQ}}(2\tau_{e/r}) &\approx \left[(D_{\text{res}}^{\text{DQ}})^2 \tau_{e/r}^2 + \sum_{j=2}^g (-1)^{j-1} (D_j^{\text{DQ}})^{2j} \tau_{e/r}^{2j} \right] \exp\left(-\frac{2\tau_{e/r}}{T_2}\right) \\ &\approx \left[\frac{1}{2} M_2^{\text{DQ}} \tau_{e/r}^2 + \sum_{j=2}^g (-1)^{j-1} \frac{M_{2j}^{\text{DQ}}}{2j!} \tau_{e/r}^{2j} \right] \exp\left(-\frac{2\tau_{e/r}}{T_2}\right), \end{aligned} \quad (5.2)$$

where S_{DQ} is the normalized double-quantum signal, $D_{\text{res}}^{\text{DQ}}$ and M_2^{DQ} are the effective residual dipolar coupling and effective second van Vleck moment encoded by dipolar filter. The other terms in the sums are the contributions from other couplings which will not be discussed here. Goldman^[186] and Mehring^[132] proved that thanks to the nature of spin $\frac{1}{2}$ dipolar coupling and double-quantum dipolar filter edition, M_2^{DQ} , in fact, equals to M_2 . Besides, $D_{\text{res}}^{\text{DQ}}$ and D_{res} are also similar. Furthermore, based on Equation 5.2, it is easy to obtain the relation of:

$$M_2^{\text{DQ}} \approx 2(D_{\text{res}}^{\text{DQ}})^2 \quad (5.3a)$$

and

$$M_2 \approx 2(D_{\text{res}})^2. \quad (5.3b)$$

5.4 ^1H Residual Dipolar Coupling by Double-Quantum NMR

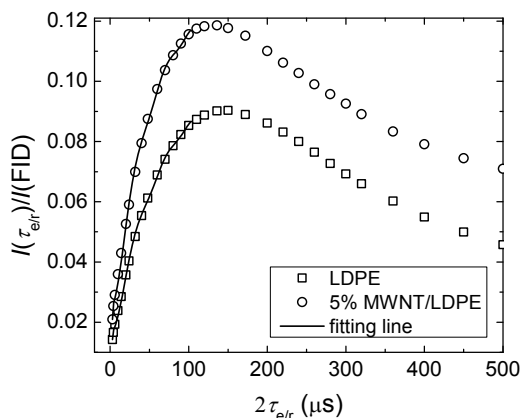


Figure 5.15: Fit result of double-quantum buildup curves at the initial excitation/reconversion period. The curves displayed here are from the amorphous phase of neat LDPE and the nanocomposite with 5% MWNT amount.

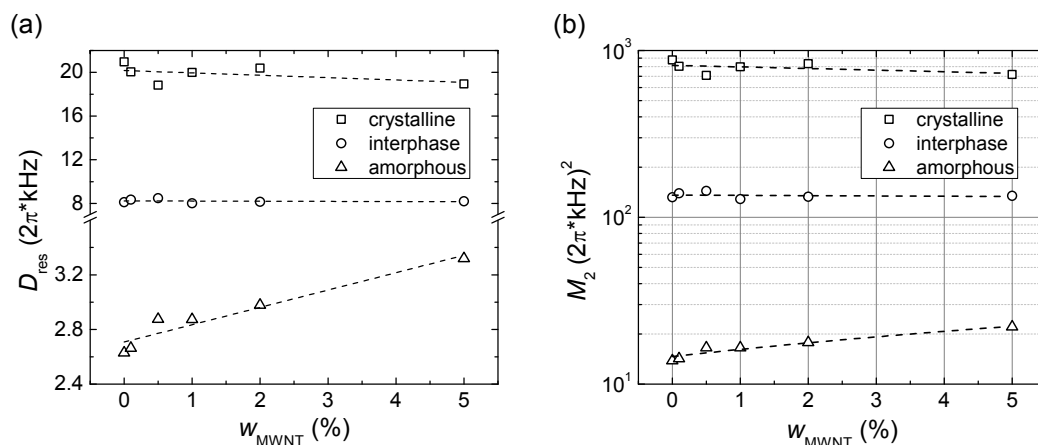


Figure 5.16: (a) Residual dipolar coupling, and (b) second van Vleck moment of LDPE and the composites as a function of MWNT amount.

Figure 5.15 shows the fit quality which is perfect at the beginning of the buildup curves. Figure 5.16 displays the fit results according to different MWNT amounts. As indicated in Equation 5.3, the behavior of D_{res} and M_2 must be the same. The ^1H dipolar couplings in the crystalline phase are the strongest, and those in the amorphous phase are the weakest, while those in the interphase stay in between. By increasing the loading amount of MWNT in LDPE matrix, the dipolar couplings in the crystalline phase and in the interphase do not change

5 Study of MWNT/LDPE Composite by Solid-State NMR

obviously. This indicates the presence of MWNT does not affect the fundamental building of the crystal or the chain conformation in the interphase. However, on the other hand, both D_{res} and M_2 increase with increasing MWNT amount in the amorphous phase, in which a 25% and 60% increment of the sample with 5% MWNT than those of the neat LDPE are observed for D_{res} and M_2 , respectively. By loading MWNT, the ^1H dipolar couplings in the amorphous phase get stronger, and the stronger interaction indicates either a closer proton-proton distance or stronger chain restrictions. Therefore, it is not difficult to elaborate that by loading MWNT in LDPE, the chain conformation in the amorphous phase is affected significantly and, consequently, influences the physical performance of the nanocomposite.

5.5 MWNT/LDPE Structure and Properties

In CNT/PE nanocomposite, the noncovalent interactions between CNTs and polymer matrix cause the CNTs to act as physical joints among the polymer chains. At the same time, they enable the polymer matrix to incorporate the physical merits of CNT for the improvement of the performance of the nanocomposite, in different aspects. However, the presence of CNTs also induces some side effects, for example, the noncovalent interaction confines the polymer chains due to physical crosslinking effect and, thus, reduces the chain mobilities. It influences the material performance in two ways: first the crystallization kinetics during processing which in turn changes the morphology of the final products. Second, the molecular dynamics in solid matrix are also changed. Both these two aspects affect the physical properties of the nanocomposite.

5.5.1 Influence on the Crystallization Kinetics

The crystallization kinetics of polymer material are somewhat similar to those of small molecules, which can be described as a two-step procedure, i.e. nucleation and crystal growth. Avrami function^[272] is widely applied to describe this process as:

$$w_c(t) = 1 - \exp(-Kt^\xi), \quad (5.4)$$

5.5 MWNT/LDPE Structure and Properties

where $w_c(t)$ is the crystallinity at t , K is the crystallization constant, and ξ is Avrami exponent which is decided by the nucleation mechanism as well as the crystal growth geometry. In a specified system, ξ is always fixed, while K is more complicated which depends not only on the molecular dynamics, but also the crystallization temperature.

In the current case, the presence of MWNT changes the crystallization kinetics of the nanocomposite from that of the neat LDPE. First, the MWNTs act as the nucleation agent. The polymer chains tend to condense on the CNTs and form the crystal nuclei. This assists the heterogeneous nucleation and, thus, speeds up the crystallization by increasing K and changing ξ . Second, due to the chain confinement and lower chain mobilities, the growth of crystals is, however, hampered by decreasing K . Therefore, K is determined by both nucleation step and crystal growth step, it is related to the crystallization temperature as well as the activation energies of the above two steps. These relations can be well described by Arrhenius equation. Based on Kissinger equation,^[273] Lauritzen and Hoffman^[239,274] have proposed a calculation model to describe both nucleation and crystal growth during crystallization for polymers, simultaneously. However, due to the new findings on the polymer crystal morphology, the old model can not fulfill all aspects. Recently, a more general model has been introduced to describe K when the crystallization takes place by cooling polymers from their melts as:^[275–278]

$$K(T) = K_0 \exp \left[\frac{-E_a^n}{\lambda R(T_m - T)} \right] \exp \left[\frac{-E_a^g}{R(T - T_g)} \right], \quad (5.5)$$

where K_0 is the crystal growth rate constant; E_a^n and E_a^g are the activation energies for nucleation as well as crystal growth, respectively; and λ is a calibration constant. If the activation energies are constant, the crystallization rate is controlled by temperature. When the temperature is too high, e.g. close to T_m the nucleation step is depressed due to the strong molecular disturbance caused by the Brownian chain motions. However, if it is too low, e.g. close to T_g , the crystal growth is not possible because of the chain-frozen effect. Therefore, T_c with the highest crystallization rate must at certain point between T_g and T_m . In this study, $T_c \approx 90^\circ\text{C}$ was observed for the neat LDPE, as shown in Table 5.2.

5 Study of MWNT/LDPE Composite by Solid-State NMR

With the presence of MWNT in the LDPE matrix, both E_a^n and E_a^g are influenced, but in different ways. With the function of nucleation agent, MWNTs assist the nucleation step by decreasing E_a^n . However, on the other hand, due to the chain confinement which is caused by the physical crosslinking effects, as we observed by dramatic T_2^m decrement of the melts in Figure 5.7, the mobilities of the chain segments decrease. Therefore, the diffusivity of the chains to the crystal nuclear surface decreases and, thus, E_a^g increases. By loading MWNT, kinetically, the nucleation step gets faster while the crystal growth step becomes slower. This is the reason that for the nanocomposites T_c shifts to higher value than that of neat LDPE, as shown in Table 5.2. It also explains the decreasing lamella thickness, as shown in Figure 5.3, as more nuclei generates on the MWNT walls at the first step, while the crystal growth rate on the nuclei reduces at the second step. In addition, the reduction of crystallinity and the increment of the amounts of the interphase as well as the amorphous phase observed in Table 5.2 and Figure 5.4 reflect that the chain confinement effect is more remarkable than the nucleation assistant effect. This also indicates the strong interactions between LDPE chains and MWNTs.

5.5.2 Nanohybrid Shish-Kebab Structure

MWNTs generally have a outer diameter of about 2~100 nm which consist of a varying number of graphene layers with an interlayer separation of about 0.3 nm, and the specific surface area of MWNT is about 40~300 m²/g.^[279,280] Due to the interactions between MWNT and LDPE matrix, the crystal lamella are more easily to grow in a two dimensional manner around the MWNTs. The MWNT acts not only as the nucleation agent but also as the morphological ‘c’ axis to string the lamellae together.^[227,229] This MWNT linked lamellar structure is similar to the classic shish-kebab polymer crystallography which is first observed by Reneker *et al.*^[281] and Pennings *et al.*^[282]

A typical polymer shish-kebab crystal structure is usually constructed by a fibrils stem (shish) and the disk shaped lamellae (kebab) arranged perpendicularly along the stem. It is generated by placing the bulk polymers under shear field during the crystallization, thus, to originate the fibril stems. However, in

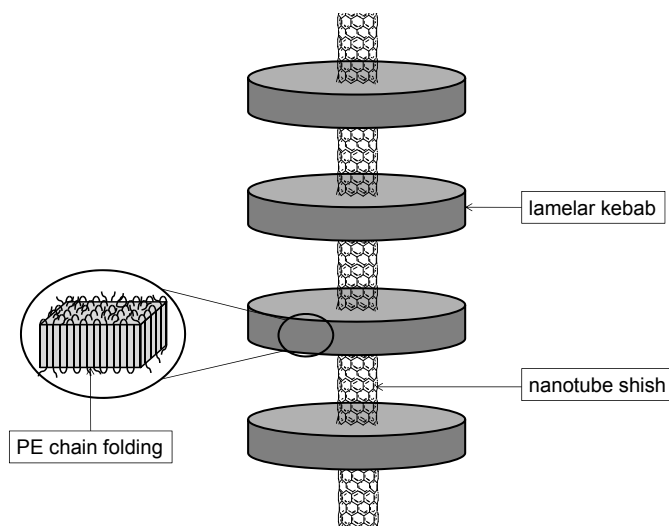


Figure 5.17: Schematic digram of MWNT/LDPE nanohybrid shish-kebab supermolecular structure.

nanocomposite, the MWNTs perform as the crude fibril stems to string up the lamellar disks. Therefore, similar structures can be yield even without shear field. In such occasion, the stringed structure is referred as nanohybrid shish-kebab,^[283] as shown in Figure 5.17.

The crystalline phase of the nanohybrid shish-kebab has been well interpreted in previous work, in which the crystal can be well described by the switchboard model.^[284,285] Besides, it has been widely accepted that the building block of a crystal is unaffected by the introduction of nanotube.^[286] However, up to now, the description of the noncrystalline region of such supermolecular structure is still unclear. Furthermore, the model in Figure 5.17 is not able to describe the interactions between the naked nanotubes and the rest of polymer chains, for instance, the chains from the interphase and the amorphous phase. As a matter of fact, all the three morphological phases¹ strongly interact with the nanotubes, and the interfaces between different morphological phases and nanotubes behave differently, which in turn influence the corresponding molecular dynamics of the phases differently.

¹crystalline phase, interphase, and amorphous phase

5 Study of MWNT/LDPE Composite by Solid-State NMR

According to the current results, as shown in Figure 5.5 and Figure 5.16, molecular dynamics of the amorphous phase are influenced most severely by the presence of MWNTs, in which T_2 decreases by 50% with 5% MWNT loading, while at the same time, D_{res} and M_2 increase by 25% and 60%, respectively. Zheng *et al.*^[230] observed the wrapping effect of the CNTs by polymer thin films, which is induced by the surface tension of the MWNTs. In the semicrystalline polymer cases, the thin film is contributed mainly by the amorphous phase. Due to the strong noncovalent interactions, the “tie” and “loop” molecules tend to collapse on the nanotubes, which leads to a more compact chain conformation in the amorphous phase. Therefore, the chain mobilities and the average distance between the neighboring protons in this region reduce, which in turn influence the physical properties of the nanocomposite.

5.5.3 MWNT/LDPE Physical Properties

The physical properties of the nanocomposite is strongly related to the interactions between the nanotubes and polymer matrix both in melt and solid states. The interactions also influence the morphology and molecular dynamics which can be described by solid-state NMR. According to the current observations, the improvement of the thermal stability of the nanocomposites can be explained by the increasing of the thermal decomposition activation energy of the molecular chains due to the noncovalent molecular interactions, and the decomposition kinetics can also be described by Kissinger’s equation.^[273] Besides, according to the result of mechanical test carried out in IAP,^[287] Young’s modulus of the nanocomposite increases with the increasing MWNT amount, while the fracture strain decreases. In addition, the tensile strength of nanocomposites is consistently higher than that of the neat LDPE. The improvement of Young’s modulus can be estimated by the short fiber reinforced polymer composite theory as:^[288]

$$E_c = \eta_0 \eta_1 V_n E_n + (1 - V_n) E_p, \quad (5.6)$$

where E_c , E_n , and E_p are Young’s modulus of nanocomposite, MWNT, and polymer matrix, respectively; η_0 and η_1 are the interaction coefficients which

related to the MWNT critical length and their orientations in the polymer matrix; and V_n is the volume fraction of MWNT. As E_n of MWNT is extremely high,^[208] it is not difficult to understand that E_c improves with the presence of MWNT and the improvement increases with increasing MWNT amount.

On the other hand, the reduction of the fracture strain indicates the toughness of LDPE matrix decreases. As demonstrated in the previous section, due to the presence of MWNT, the spontaneous formation of the nanohybrid shish-kebab structure changes the molecular dynamics and chain conformations, especially, in the amorphous phase. These aspects strongly relate with the physical properties of the material. The fractures of the specimens during the mechanical drawing are typical ductile with high elongation ratios. However, for the MWNT/LDPE composite, the reductions of the chain mobilities and the conformation diversities cause the decreasing of the stretchability of the “ties” and “loops” in the amorphous phase and, consequently, reduce the toughness of the material. Besides, the reductions of crystallinity and lamella thickness also reduce the chain adhesiveness in the crystalline phase which lead the slips between chain segments to occur more easily under drawing and, thus, generates the Mosaic blocks in an earlier stage, as discussed in Section 4.5.2. Furthermore, MWNTs also act as impurities in LDPE, the interface between nanotubes and polymer matrix causes the stress concentration effect, which also increases the brittleness of the material, as explained in Section 4.5.3. All in all, by increasing the MWNT amount, the elongation ratio of LDPE matrix reduces at fracture, which indicates a transformation trend from ductile to brittle fracture under stress. For real application these side effects must be taken into consideration and should be avoided. In fact, thanks to the superior properties of CNT, its loading amount is actually very low and will not influence the toughness of polymer matrix strongly.

5.6 Summary

MWNT/LDPE nanocomposites have been investigated by a combination of DSC and solid-state NMR study. According to the current observations, morphology and molecular dynamics of the LDPE matrix are closely related to each other and

5 Study of MWNT/LDPE Composite by Solid-State NMR

influence the physical properties of the nanocomposite synergistically. Both the crystallinity and the lamella thickness decrease with increasing MWNT amount, while the amounts of the interphase and the amorphous phase increase. This is caused by the change of the crystallization kinetics. The presence of MWNTs has double functions during the crystallization of LDPE from its melt: nucleation agent which assists the formation of the nuclei and chain confinement effect which hinders the growth of the crystal. As a result, the crystal core number increases, while their growth rate decreases and, consequently, both the average crystal size and the crystallinity decreases.

Besides, the molecular dynamics also change and it is most remarkable in the amorphous phase. It has been observed that T_2 decreases and ^1H residual dipolar coupling increases with increasing MWNT amount. This can be explained by the high surface tension of the MWNTs which leads the flexible chains in the amorphous phase to collapse on them. Therefore, the conformation of the chains in this region is more compacted which increases the neighboring ^1H interactions as well as the chain restrictions.

All the above aspects influence the physical properties of the nanocomposite in comparison with its neat polymer matrix. The thermal stability and the tensile strength increase due to the strong interaction between MWNTs and LDPE matrix as well as the excellent mechanical properties of MWNT. However, the toughness of the material reduces due to decreasing flexibility of the amorphous phase, which is also caused by the strong noncovalent interactions between MWNTs and polymer chains.

6

Conclusions and Outlooks

Morphology and molecular dynamics of PE were investigated by DSC and ^1H solid-state NMR. The correlation between different methods proves that the advantages of NMR are its abilities to define the three-component phase composition via different molecular relaxations in a wide range of crystallinities precisely, and based on which the information of molecular dynamics of different phases is extractable. Besides, the effectiveness of the NMR-MOUSE on semicrystalline polymer study has been proved in a wide range of crystallinities, and its application to the quality control of HDPE pipe production in a noninvasive manner has been carried out successfully. Furthermore, most importantly, by the applications of spin-diffusion pulse sequence and modified phase selectable double-quantum pulse sequence, solid-state NMR is able to describe the domain sizes as well as the residual dipolar couplings of each phase,¹ respectively. In terms of these bases, two major application systems were interpreted: the physical aging of HDPE pipes as well as the physical properties of the MWNT/LDPE nanocomposites.

The results indicate that the physical performances of PE are strongly related to the amount and the properties of the amorphous phase. It was found that both aging and nanofiller affect the chain conformation and reduce the molecular dynamics in the amorphous phase. Therefore, as a consequence, the material toughness is influenced. The change of the amorphous phase influences the material differently in different systems. In pipe physical aging, the ability of the pipes

¹Such detailed information of the interphase and the amorphous phase is not available by the current other techniques.

6 Conclusions and Outlooks

to hinder the slow crack growth decreases due to the embrittlement effect and, thus, influences their long term performance. In the nanocomposite system, the chain conformation diversities and flexibilities reduce due to the surface tension effect and, consequently, the impact strength of the material suffers. Both above cases illustrate that the understanding of the molecular structure, conformation, and dynamics in the amorphous phase is extremely important for the application of semicrystalline polymers.

After intensive study on the above topics, the conclusions not only answered the application difficulties/problems of PE, but also improved the contribution of solid-state NMR on solid polymer studies. There are several achievements worth to mention: (1) the correlation between morphology/molecular dynamics and the pipe resistance against aging has high application potential to the lifetime estimation of the existing PE pipe systems. (2) The highlighted importance of the properties of the amorphous phase helps to understand the physical behavior of the semicrystalline polymer better and, thus, provides more guidances for the tailored application development of the material. (3) The investigation of the NMR-MOUSE on the solid polymer study has validated its application to this field, it allows the NMR-MOUSE using on the quality control of plastic productions in industry, and the most important advantages are its nondestructive detecting manner and its portable identity. (4) The successful modification of the double-quantum pulse sequence makes the detailed phase investigation of the multicomponent polymers possible, which also assists to understand the properties of the material more effectively.

However, the current work is just some of the initializations for the whole study on morphology and molecular dynamics of semicrystalline polymers by solid-state NMR relaxometry. There are still remaining problems. Besides, there are also some interesting subjects worth to be further studied and will bring rewarding progresses to not only in scientific researches but also in industry applications. First, the application of high resolution NMR of rare nuclei, for example, the cross polarization measurement with MAS is able to describe the couplings between ^{13}C and ^1H in different phases. Its detecting sensitivity is different from ^1H NMR, and can provide supplement information in the material study. Second, the application of NMR-MOUSE to solid polymers is another attractive topic

still need to be further pursued in two aspects: (1) its application to the low crystallinity region of semicrystalline polymer need to be continually investigated and confirmed; (2) the on-site evaluation of the plastic pipes by the NMR-MOUSE is expected to estimate the remaining service time of the existing pipe systems in a nondestructive manner. This in field application issue leads to the third topic: the relation between T_2 and the performance of the pipes. As mentioned above, this question has been answered partially according to the current results that the material mechanical resistance against the slow crack growth decreases with decreasing T_2 . However, in order to establish a consolidate relation between them, more results are necessarily, and based on which the estimation of the remaining lifetime of the pipe system can come into being. Fourth, the aging of MWNT/LDPE composite is also an interesting topic, in which with the presence of MWNT, the aging mechanism must be influenced and is worth for further investigation as a scientific topic in the current stage.

6 Conclusions and Outlooks

Appendix

In this appendix two issues will be discussed. The first one is the temperature dependences of phase composition and relaxation times of PE determined by ^1H FID. This helps to figure out the best probing temperature and, thus, to improve the phase resolution as well as the result reliability. The second one is the errors of the research system, including the systematic error of DSC and NMR, as well as the inhomogeneity of the PEHD pipe. It helps to confirm the conclusions drawn by the current observations.

A Probe Body Temperature Calibration

Calibration of the BTV3000 temperature controlling system was carried out on both 200 MHz and 500 MHz spectrometers with their respective 4 mm solid probe bodies used in this study. Ethylene glycol was used as the reference, and the real temperature of the sample in the probe body (T_r) can be calculated by the chemical shift difference between the two peaks in the spectra.^[289,290] The deviation between the programmed temperature (T_p) and T_r can be described by encoding T_p with the BTV3000 system.

Figure I shows the calibration results performed from room temperature to the thresholds of the probe bodies. The deviations between T_r and T_p are observed in both probe bodies, in which T_r is systematically higher than T_p . The deviation becomes more severe with increasing temperature. This is caused by the overheating problem during the temperature encoding, and the effect is slightly more significant on the 200 MHz probe body than that of the 500 MHz.

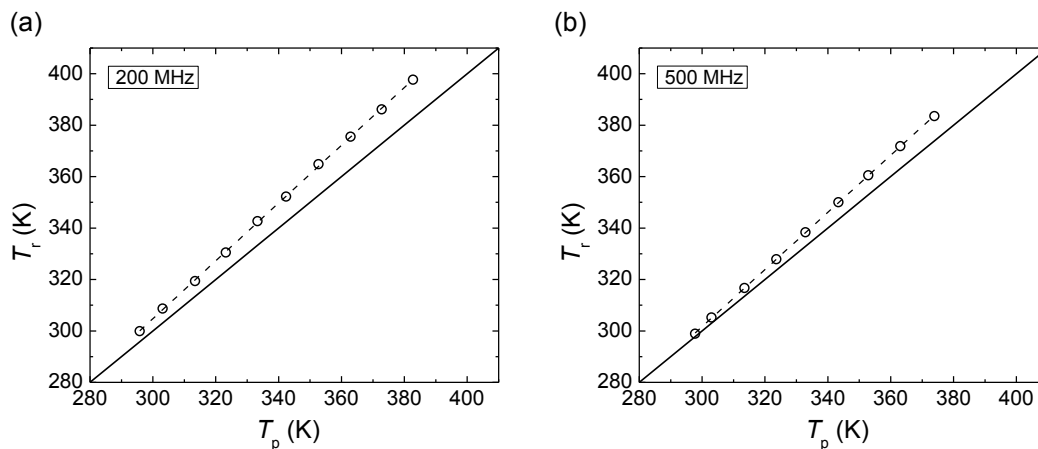


Figure I: Calibration of sample temperatures in the NMR solid probe bodies encoded by BTV3000 temperature controlling system: (a) 200 MHz and (b) 500 MHz.

B Temperature Dependence of NMR Results

Temperature dependences of the phase composition and T_2 of both HDPE and LDPE determined by ^1H FID is studied on the 200 MHz spectrometer. The probing temperature was from room temperature to 380 K, and an increment of 10 K per step is used. Figure II shows the relation between phase compositions and the probing temperatures, in which the same temperature dependence is observed for HDPE and LDPE. Both w_c and w_i decrease with increasing temperature, while at the same time, w_a increases. The increments are also temperature dependent, in which they become more significant at high temperature region for all phases. This is due to the melting effect which destroys the small and/or imperfect crystals at an early stage, as shown in Figure 3.1. Besides, the sensitivities of LDPE and HDPE are different, in which the phase composition changes more remarkably in LDPE due to increasing temperature.

Figure III shows the T_2 s, both T_2^i and T_2^a increase with the temperature, but T_2^c is independent on it. The behavior is basically the same between LDPE and HDPE, except T_2^a in HDPE is more stable at low temperatures. However, it goes up steeply at the higher temperature region. Based on the above observations we are now able to figure out the best detecting temperature regions for both LDPE

B Temperature Dependence of NMR Results

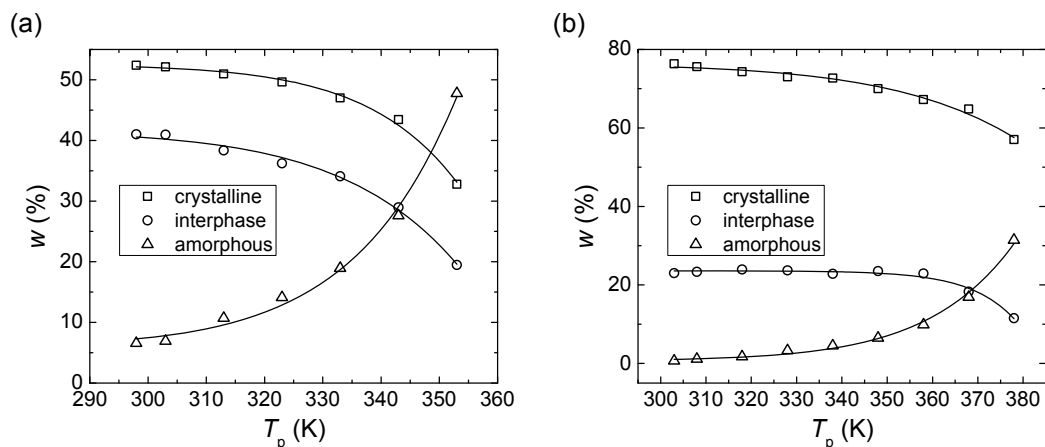


Figure II: Temperature dependence of phase composition of PE determined by ^1H FID: (a) LDPE and (b) HDPE.

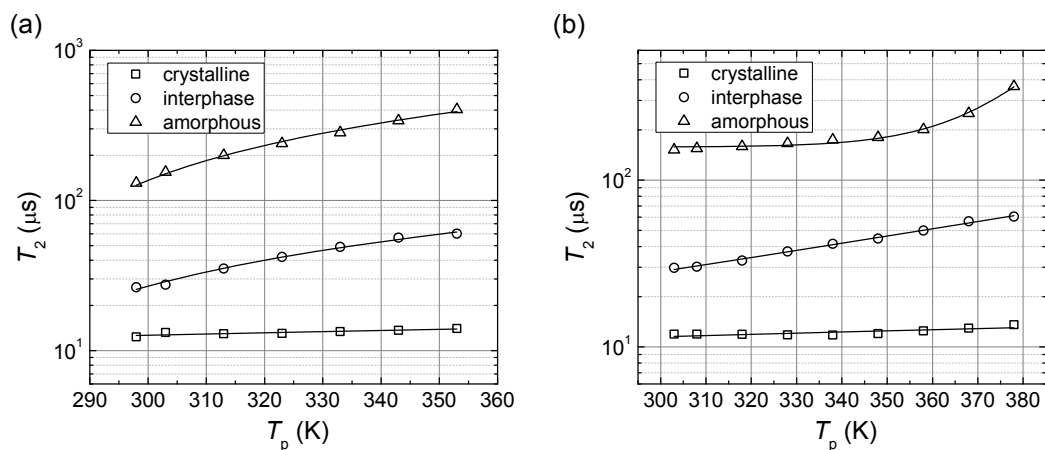


Figure III: Temperature dependence of transverse relaxation times of PE determined by ^1H FID: (a) LDPE and (b) HDPE.

and HDPE. For LDPE if T_p is higher than 340 K, the melting effect becomes very significant, and influences the characterized phase composition severely. For HDPE, this transition point is observed at around 370 K. On the other side, if T_p is too low, due to the chain confinement effect the amorphous phase is almost unobservable, while by increasing the detecting temperature the phase resolution improves. This phenomenon is especially obvious for HDPE. Thus, in order to have a better phase resolution, it is necessarily to increase the temperature

and, at the same time, the melting effect must also be taken into account. In the current study, the optimal T_p on the 200 MHz spectrometer is defined to 363 K for HDPE and 333 K for LDPE, both of the values are around 35 K lower than their T_m s determined by DSC. Additionally, in considering almost the same temperature deviation behavior of the probe bodies, these values are also applied to the 500 MHz spectrometer.

C Systematic Error of DSC

Systematic error of DSC was investigated on the DSC 200F3 apparatus. The measurement parameters are the same as mentioned in Section 3.2.1. Seven heating and cooling scans were run for the same HDPE sample, separately. Between each scan, the crucible was first taken out and then replaced in the furnace. In such a way, it is able to inspect the influence of the position of the crucible on the results. In order to have the scans be measured from the sample with identical thermal history, only the traces from the second to the seventh scan were taken.

Table I: Systematic error of DSC.

Scans	Δh_m J/g	T_m °C	T_{onset} °C	T_{end} °C
2	188.1	130.4	117.2	137.0
3	182.3	130.5	117.2	136.9
4	183.7	130.4	117.2	136.7
5	183.0	130.2	117.3	136.5
6	187.8	130.3	117.5	136.5
7	185.7	130.3	117.4	136.4
Average	185.1	130.4	117.3	136.7
STDV ^a	±2.5	±0.1	±0.1	±0.2
Error	1.3%	0.1%	0.1%	0.2%

^astandard deviation

D Systematic Error of NMR-MOUSE

Table I shows the systematic errors that occur during the measurement. The accuracy of the temperature is very high, in which only 0.1% errors of T_m and T_{onset} are ignorable. The error of Δh_m is relatively higher of about 1.3%. This is mainly induced by the change of the crucible positions between the scans. If keep the crucible still and perform the measurements successively, the error of Δh_m can be controlled to only about 0.3%.

D Systematic Error of NMR-MOUSE

Systematic error of NMR-MOUSE is investigated by solid echo pulse sequence with the same parameters as described in Section 3.4.1. The samples were fixed on the top of the coil, thus, to make sure the same voxels were taken. Six decays were recorded with the NMR-MOUSE at the home position of the digital lift. Between each measurement, the sensor was first moved away from the home position by the lift and then move back to it. Therefore, the errors caused by the surrounding noises can be evaluated.

Table II: Systematic error of NMR-MOUSE.

Measurements	w_c %	w_i %	w_a %	$T_{2\text{eff}}^c$ μs	$T_{2\text{eff}}^i$ μs	$T_{2\text{eff}}^a$ μs
1	67.6	19.3	13.1	92.5	639.2	1810.7
2	67.1	18.7	14.1	92.9	634.7	1834.4
3	66.4	18.7	14.9	89.2	592.7	1800.3
4	66.4	19.0	14.6	90.3	596.7	1758.2
5	66.9	19.7	13.3	92.0	624.1	1830.8
6	67.4	18.0	14.7	92.1	613.9	1803.6
Average	67.0	18.9	14.1	91.5	616.9	1806.3
STDV	± 0.6	± 0.7	± 0.8	± 1.4	± 19.3	± 27.4
Error	0.7%	3.1%	5.3%	1.6%	3.1%	1.5%

Appendix

Table II presents the systematic error of NMR-MOUSE. The highest error is shown by the fraction of the amorphous phase, in which a ± 0.8 STDV with an error of 5.3% is detected. The error of the rest parameters are basically less than 3%, which indicates the noise level of the NMR-MOUSE is well controlled.

E Systematic Error of High-Field NMR

Systematic error of high-field NMR is investigated by ^1H FIDs with the same hardware and parameters as mentioned in Section 4.3.1. Six FIDs were recorded for the same HDPE sample. Between each measurement, the sample was taken out of the rotor and then repacked, so as to evaluate the influences of sample packing as well as the change of the rotor position in the coil on the results.

Table III: Systematic error of high-field NMR.

Measurements	w_c %	w_i %	w_a %	T_2^c μs	T_2^i μs	T_2^a μs
1	69.6	22.6	7.8	12.2	49.8	207.7
2	71.0	21.4	7.6	12.1	53.2	217.7
3	70.1	22.2	7.7	12.2	52.6	219.5
4	70.4	21.8	7.8	12.2	52.8	218.2
5	70.7	21.6	7.7	12.1	53.6	222.1
6	70.3	21.9	7.8	12.1	51.9	214.9
Average	70.4	21.9	7.7	12.1	52.3	216.6
STDV	± 0.5	± 0.4	± 0.08	± 0.05	± 1.3	± 5.1
Error	0.7%	2.0 %	1.0%	0.4%	2.6%	2.4%

Table III shows the systematic error of high-field NMR. All the errors are less than 3%, and the level is similar to that observed by DSC. The coil size of the 4 mm probe body for the Bruker 200 MHz spectrometer is not 100% precise, which induces the errors due to the position variation of the rotor. However, the

error indicates that this effect does not influence the precise of the measurement significantly. The other used probe bodies can control the rotor position better, for instance, MAS probe bodies for 500 MHz and 700 MHz spectrometers.

F Inhomogeneity of PEHD Pipes

PEHD pipes are reference samples only for laboratory study. Due to the inhomogeneity of the material throughout the pipe, the randomly picked specimen may not reflect the true property of the whole pipe. Therefore, it is necessarily to investigate the inhomogeneity of the pipe and evaluate its influence on the acquisition of the consolidate conclusions. In this work, six points from different positions of a nonaged PEHD pipe were picked, these points are evenly distributed throughout the whole segment. The inhomogeneity of the pipe is investigated by both DSC and high-field ^1H FID.

Table IV: Inhomogeneity of PEHD pipe determined by DSC.

Samples	w_c %	T_m °C	T_{onset} °C	T_{end} °C
1	57.9	133.1	125.6	139.4
2	59.4	132.4	121.6	139.4
3	57.9	131.4	121.7	137.6
4	58.0	132.5	122.4	138.4
5	58.8	132.1	120.6	138.6
6	63.5	133.0	120.9	138.1
Average	59.3	132.4	122.1	138.6
STDV	±2.1	±0.6	±1.8	±0.7
Errors	3.6%	0.5%	1.5%	0.5%

Table IV presents the inhomogeneity of nonaged PEHD pipe determined by DSC. w_c shows an error of about 3.6% among the specimens from different posi-

Appendix

tions of the pipe. The errors for the specific temperatures are less, in which that of T_m is about 0.5% and that of T_{onset} is about 1.5%. The result indicates the difference between the first five points are very small, only the sixth point shows relatively high deviation.

Table V: Inhomogeneity of PEHD pipe determined by high-field ^1H FID.

Samples	w_c %	w_i %	w_a %	T_2^c μs	T_2^i μs	T_2^a μs
1	61.8	29.0	9.2	13.1	49.5	173.9
2	61.8	28.6	8.6	13.4	51.2	177.4
3	62.0	28.1	9.9	13.3	50.8	178.6
4	65.9	26.6	7.5	12.6	50.2	173.9
5	65.0	27.1	7.9	12.8	49.0	170.5
6	66.7	26.1	7.2	12.5	50.2	178.0
Average	63.9	27.6	8.4	13.0	50.1	175.4
STDV	± 2.3	± 1.1	± 1.0	± 0.3	± 0.8	± 3.1
Error	3.5%	4.1%	12.5%	2.7%	1.6%	1.8%

Table V shows the inhomogeneity of nonaged PEHD pipe determined by high-field ^1H FID on the 200 MHz spectrometer. All the specimens are from the regions close to those for DSC test. The error of w_c determined by ^1H FID is 3.5%, which is the same as that observed by DSC. However, the errors of the other two phases are relatively higher. Especially, for the amorphous phase, an error of as high as 12.5% was observed. The accuracy of T_2 s is higher, all the errors observed are less than 3%.

The results of both DSC and high-field ^1H FID indicate that the inhomogeneity of the PEHD pipes is still in tolerance scale for the current study. The difference showed between pipes with different t_s under hydrostatic pressure test is reliable. Besides, the homogeneity of PE100 pipes is much higher than that of PEHD pipes. Therefore, the aging results for PE100 pipes are also consolidate.

References

- [1] Schaefer, J; Stejskal, EO. High-Resolution Carbon-13 NMR of Solid Polymers. *Topics in Carbon-13 NMR Spectroscopy* **1979**, *3*, 283–324.
- [2] Bovey, FA; Jelinski, LW. Nuclear Magnetic Resonance. In *Encycl. Polym. Sci. Eng.*, volume 10, pages 254–327. Wiley, **1987**.
- [3] Blümich, B; Hagemeyer, A; Schaefer, D; Schmidt-Rohr, K; Spiess, HW. Solid State NMR Spectroscopy in Polymer Science. *Adv. Mater.* **1990**, *2*, 72–81.
- [4] Yasunaga, H; Kobayashi, M; Matsukawa, S; Kurosu, H; Ando, I. Structures and Dynamics of Polymer Gel Systems Viewed Using NMR Spectroscopy. *Annu. Rep. NMR Spectrosc.* **1997**, *34*, 39–104.
- [5] Spiess, HW. Multidimensional Solid State NMR Studies of Complex Dynamics in Polymers. *AIP Conference Proceedings* **2000**, *519*, 33–39.
- [6] Cheng, HN. Compositional Heterogeneity in NMR Polymer Analysis. *Polym. Prepr. (Am. Chem. Soc., Div. Polym. Chem.)* **2003**, *44*, 261–262.
- [7] Spiess, HW. Overview of NMR of Bulk Polymers. *ACS Symp. Ser.* **2011**, *1077*, 17–35.
- [8] Brown, SP. Applications of High-Resolution ^1H Solid-State NMR. *Solid State Nucl. Magn. Reson.* **2012**, *41*, 1 – 27.
- [9] Hahn, EL. Spin Echoes. *Phys. Rev.* **1950**, *80*, 580–594.
- [10] Carr, HY; Purcell, EM. Effects of Diffusion on Free Precession in Nuclear Magnetic Resonance Experiments. *Phys. Rev.* **1954**, *94*, 630–638.
- [11] Meiboom, S; Gill, D. Modified Spin–Echo Method for Measuring Nuclear Relaxation Times. *Rev. Sci. Instrum.* **1958**, *29*, 688–691.
- [12] Dadayli, D; Harris, RK; Kenwright, AM; Say, BJ; Sünnetçioğlu, M. Solid-State ^1H NMR Studies of Polypropylene. *Polymer* **1994**, *35*, 4083 – 4087.

REFERENCES

- [13] Kristiansen, PE; Hansen, EW; Pedersen, B. Phase Distribution during Isothermal Crystallization of Polyethylene Probed by Solid-State Proton NMR Free Induction Decay. *J. Phys. Chem. B* **1999**, *103*, 3552–3558.
- [14] Horii, F; Luo, Q. *Solid State NMR for Precision Measurement of Polymers*. Kyoritsu Shuppan, **2007**.
- [15] Hansen, EW; Roots, J. Determination of Crystallinity in Polyethylene from ^1H -NMR FID Analysis Effect of Non-Curie Temperature Behavior. *Inter. J. Res. Rev. Appl. Sci.* **2010**, *5*, 207–212.
- [16] Colquhoun, IJ; Packer, KJ. Nuclear Magnetic Resonance in Solid Ethylene/ α -Olefin Copolymers: Relaxation, Spin-Diffusion and Lamellar Widths. *Brit. Polym. J.* **1987**, *19*, 151–63.
- [17] Clayden, NJ. Lamellar Thickness of Crystallizable Ethene Runs in Ethene-Propene Copolymers by Solid State NMR. *J. Polym. Sci., Part B: Polym. Phys.* **1994**, *32*, 2321–2327.
- [18] Blümich, B; Casanova, F. *Mobile NMR*. Springer Netherlands, **2006**.
- [19] Blümich, B. Mobile NMR: How Aged is Polyethylene. *Nachr. Chem.* **2007**, *55*, 158–160.
- [20] Blümich, B; Perlo, J; Casanova, F. Mobile Single-Sided NMR. *Prog. Nucl. Magn. Reson. Spectrosc.* **2008**, *52*, 197 – 269.
- [21] Blümich, B. Solid-State NMR of Heterogeneous Materials. *Adv. Mater.* **1991**, *3*, 237–245.
- [22] Schmidt-Rohr, K; Spiess, H. *Multidimensional Solid-State NMR and Polymers*. Academic Press London, **1994**.
- [23] Demco, DE; Johansson, A; Tegenfeldt, J. Proton Spin Diffusion for Spatial Heterogeneity and Morphology Investigations of Polymers. *Solid State Nucl. Magn. Reson.* **1995**, *4*, 13 – 38.
- [24] Buda, A; Demco, DE; Blümich, B; Litvinov, VM; Penning, JP. Complex Morphology of Melt-Spun Nylon-6 Fibres Investigated by ^1H Double-Quantum-Filtered NMR Spin-Diffusion Experiments. *ChemPhysChem* **2004**, *5*, 876–883.
- [25] Buda, AA; Demco, DE; Bertmer, M; Blmich, B. Multiple-Quantum NMR on Structure, Orientation, Morphology and Dynamics of Polymers, Biomolecules and Ordered Tissues. *C. R. Chim.* **2006**, *9*, 346 – 356.

REFERENCES

- [26] Munowitz, M; Pines, A. Principles and Applications of Multiple-Quantum NMR. *Adv. Chem. Phys.* **1987**, *66*, 1–152.
- [27] Brown, S; Spiess, H. Advanced Solid-State NMR Methods for the Elucidation of Structure and Dynamics of Molecular, Macromolecular, and Supramolecular Systems. *Chem. Rev.* **2001**, *101*, 4125.
- [28] Spiess, HW. Nuclear Magnetic Resonance Spectroscopy in Macromolecular Science. *Macromol. Chem. Phys.* **2003**, *204*, 340–346.
- [29] Voda, A; Voda, MA; Beck, K; Schaubert, T; Adler, M; Dabisch, T; Bescher, M; Viol, M; Demco, DE; Blümich, B. Segmental Orientation of Thermoplastic Polyurethanes Investigated by ^1H Double-Quantum NMR. Correlation with Thermodynamic and Mechanical Properties. *Polymer* **2006**, *47*, 2069 – 2079.
- [30] Saalwächter, K. Proton Multiple-Quantum NMR for the Study of Chain Dynamics and Structural Constraints in Polymeric Soft Materials. *Prog. Nucl. Magn. Reson. Spectrosc.* **2007**, *51*, 1 – 35.
- [31] von Pechmann, H. Über Diazomethan und Nitrosoacylamine. *Ber. Dtsch. Chem. Ges.* **1898**, *31*, 2640–2646.
- [32] Friedrich, MEP; Marvel, CS. The Reaction Between Alkali Metal Alkyls and Quaternary Arsonium Compounds. *J. Am. Chem. Soc.* **1930**, *52*, 376–384.
- [33] Ziegler, K; Gellert, HG. Germany Patent 878560, **1953**.
- [34] Natta, G; Pino, P; Corradini, P; Danusso, F; Mantica, E; Mazzanti, G; Moraglio, G. Crystalline High Polymers of α -Olefins. *J. Am. Chem. Soc.* **1955**, *77*, 1708–1710.
- [35] Polyethylene. Technical report, World Petrochemical Report, **2011**.
- [36] Natarajan, K; Samulski, E; Cukier, R. Molecular Morphology of Polyethylene Determined by NMR. *Nature* **1978**, *275*, 527–530.
- [37] Hughes, CD; Sethi, NK; Baltisberger, JH; Grant, DM. Polyethylene Crystallinity from Static, Solid-State NMR Spectra. *Macromolecules* **1989**, *22*, 2551–2554.
- [38] Hansen, EW; Kristiansen, PE; Pedersen, B. Crystallinity of Polyethylene Derived from Solid-State Proton NMR Free Induction Decay. *J. Phys. Chem. B* **1998**, *102*, 5444–5450.
- [39] Litvinov, VM; Penning, JP. Phase Composition and Molecular Mobility in Nylon 6 Fibers as Studied by Proton NMR Transverse Magnetization Relaxation. *Macromol. Chem. Phys.* **2004**, *205*, 1721–1734.

REFERENCES

- [40] Hedesiu, C; Demco, DE; Kleppinger, R; Buda, AA; Blümich, B; Remerie, K; Litvinov, VM. The Effect of Temperature and Annealing on the Phase Composition, Molecular Mobility and the Thickness of Domains in High-Density Polyethylene. *Polymer* **2007**, *48*, 763 – 777.
- [41] Hedesiu, C; Demco, DE; Kleppinger, R; Poel, GV; Gijsbers, W; Blümich, B; Remerie, K; Litvinov, VM. Effect of Temperature and Annealing on the Phase Composition, Molecular Mobility, and the Thickness of Domains in Isotactic Polypropylene Studied by Proton Solid-State NMR, SAXS, and DSC. *Macromolecules* **2007**, *40*, 3977–3989.
- [42] Zhang, L; Hansen, EW; Helland, I; Hinrichsen, E; Larsen, Å; Roots, J. Crystallinity in Ethene-1-Hexene Copolymers Determined by ^1H and ^{13}C NMR. A Comparative Study. *Macromolecules* **2009**, *42*, 5189–5195.
- [43] Li, W; Adams, A; Wang, J; Blümich, B; Yang, Y. Polyethylene/Palygorskite Nanocomposites: Preparation by *in-situ* Polymerization and Their Characterization. *Polymer* **2010**, *51*, 4686 – 4697.
- [44] Keller, A. A Note on Single Crystals in Polymers: Evidence for a Folded Chain Configuration. *Philos. Mag.* **1957**, *2*, 1171–1175.
- [45] Keller, A. Polymer Crystals. *Rep. Prog. Phys.* **1968**, *31*, 623.
- [46] Petraccone, V; Allegra, G; Corradini, P. Calculation of Minimum Potential Energy of Folds and Kinks in Polyethylene Crystals. *J. Polym. Sci., Part C: Polym. Sym.* **1972**, *38*, 419–427.
- [47] Ungar, JKABI, G. Stejny; Whiting, MC. The Crystallization of Ultralong Normal Paraffins: The Onset of Chain Folding. *Science* **1985**, *229*, 386–389.
- [48] Toda, A. Growth of Polyethylene Single Crystals from the Melt: Change in Lateral Habit and Regime I–II Transition. *Colloid Polym. Sci.* **1992**, *270*, 667–681.
- [49] Fischer, EW. Step and Spiral Crystal Growth of High Polymers. *Z. Naturforsch.* **1957**, *12a*, 753–4.
- [50] Kitamaru, R; Horii, F; Hyon, SH. Proton Magnetic Resonance Studies of the Phase Structure of Bulk-Crystallized Linear Polyethylene. *J. Polym. Sci., Polym. Phys. Ed.* **1977**, *15*, 821–836.
- [51] Vonk, CG; Pijpers, AP. An X-Ray Diffraction Study of Nonlinear Polyethylene. I. Room-Temperature Observations. *J. Polym. Sci., Polym. Phys. Ed.* **1985**, *23*, 2517–2537.

REFERENCES

- [52] Mutter, R; Stille, W; Strobl, G. Transition Regions and Surface Melting in Partially Crystalline Polyethylene: A Raman Spectroscopic Study. *J. Polym. Sci., Part B: Polym. Phys.* **1993**, *31*, 99–105.
- [53] Sadler, DM; Keller, A. Neutron Scattering of Solution-Grown Polymer Crystals: Molecular Dimensions Are Insensitive to Molecular Weight. *Science* **1979**, *203*, 263–265.
- [54] Spells, S; Keller, A; Sadler, D. I.R. Study of Solution-Grown Crystals of Polyethylene: Correlation with the Model from Neutron Scattering. *Polymer* **1984**, *25*, 749 – 758.
- [55] Fischer, EW; Schmidt, GF. Über Langperioden bei Verstrecktem Polyäthylen. *Angew. Chem.* **1962**, *74*, 551–562.
- [56] Flory, PJ. On the Morphology of the Crystalline State in Polymers. *J. Am. Chem. Soc.* **1962**, *84*, 2857–2867.
- [57] Guttman, CM; DiMarzio, EA; Hoffman, JD. Calculation of SANS Intensity for Polyethylene: Effect of Varying Fold Planes and Fold Plane Roughening. *Polymer* **1981**, *22*, 597 – 608.
- [58] DiMarzio, E; Guttman, C. Three Statistical Mechanical Arguments that Favour Chain Folding in Polymer Systems of Lamellar Morphology. *Polymer* **1980**, *21*, 733 – 744.
- [59] Hoffman, JD; Williams, G; Passaglia, E. Analysis of the α , β , and γ Relaxations in Polychlorotrifluoroethylene and Polyethylene: Dielectric and Mechanical Properties. *J. Polym. Sci., Part C: Polym. Sym.* **1966**, *14*, 173–235.
- [60] Fröhlich, H. Dielectric Loss in Paraffin-Wax Solutions. *Proc. Phys. Soc.* **1942**, *54*, 422.
- [61] Fröhlich, H; Maradudin, A. *Theory of Dielectrics*, volume 12. **1959**.
- [62] Aylwin, P; Boyd, R. Aliphatic Polyesters as Models for Relaxation Processes in Crystalline Polymers: 1. Characterization. *Polymer* **1984**, *25*, 323 – 329.
- [63] Nakayasu, H; Markovitz, H; Plazek, D. The Frequency and Temperature Dependence of the Dynamic Mechanical Properties of a High Density Polyethylene. *J. Rheol.* **1961**, *5*, 261.
- [64] Hu, WG; Boeffel, C; Schmidt-Rohr, K. Chain Flips in Polyethylene Crystallites and Fibers Characterized by Dipolar ^{13}C NMR. *Macromolecules* **1999**, *32*, 1611–1619.
- [65] Ferry, J. *Viscoelastic Properties of Polymers*. John Wiley & Sons Inc, **1980**.

REFERENCES

- [66] Williams, ML; Landel, RF; Ferry, JD. The Temperature Dependence of Relaxation Mechanisms in Amorphous Polymers and Other Glass-Forming Liquids. *J. Am. Chem. Soc.* **1955**, *77*, 3701–7.
- [67] Fox, J, Thomas G.; Flory, P.J. Second-Order Transition Temperatures and Related Properties of Polystyrene. I. Influence of Molecular Weight. *J. Appl. Phys.* **1950**, *21*, 581–91.
- [68] Cowie, J. *Polymers: Chemistry and Physics of Modern Materials*. CRC press, **1991**.
- [69] He, M; Chen, W; Dong, X. Polymer Physics. *Shanghai: Fudan University Press* **1990**, page 227.
- [70] Wunderlich, B. Motion in Polyethylene. III. The Amorphous Polymer. *J. Chem. Phys.* **1962**, *37*, 2429.
- [71] Boyer, R. The Relation of Transition Temperatures to Chemical Structure in High Polymers. *Rubber Chem. Technol.* **1963**, *36*, 1303.
- [72] Schatzki, TF. Molecular Interpretation of the γ -Transition in Polyethylene and Related Compounds. *J. Polym. Sci., Part C: Polym. Sym.* **1966**, *14*, 139–140.
- [73] Khanna, YP; Turi, EA; Taylor, TJ; Vickroy, VV; Abbott, RF. Dynamic Mechanical Relaxations in Polyethylene. *Macromolecules* **1985**, *18*, 1302–1309.
- [74] Crissman, JM. On the Transition from Paraffinic to Polymeric Behavior: Mechanical Properties. *J. Polym. Sci., Polym. Phys. Ed.* **1975**, *13*, 1407–1416.
- [75] Sayre, JA; Swanson, SR; Boyd, RH. The Effect of Pressure on the Volume and the Dielectric Relaxation of Linear Polyethylene. *J. Polym. Sci., Polym. Phys. Ed.* **1978**, *16*, 1739–1759.
- [76] Heaton, N; Benavente, R; Pérez, E; Bello, A; Pereña, J. The γ Relaxation in Polymers Containing Ether Linkages: Conformational Dynamics in the Amorphous Phase for a Series of Polybibenzoates Containing Oxyethylene Spacers. *Polymer* **1996**, *37*, 3791 – 3798.
- [77] Krigbaum, W; Roe, RJ; Jr, KS. A Theoretical Treatment of the Modulus of Semi-Crystalline Polymers. *Polymer* **1964**, *5*, 533 – 542.
- [78] Boyd, RH. Relaxation Processes in Crystalline Polymers: Experimental Behaviour—a Review. *Polymer* **1985**, *26*, 323 – 347.
- [79] Popli, R; Mandelkern, L. The Transition in Ethylene Copolymers: The β -Transition. *Polym. Bull.* **1983**, *9*, 260–267.

REFERENCES

- [80] Popli, R; Glotin, M; Mandelkern, L; Benson, RS. Dynamic Mechanical Studies of α and β Relaxations of Polyethylenes. *J. Polym. Sci., Polym. Phys. Ed.* **1984**, *22*, 407–448.
- [81] Matsuo, M; Bin, Y; Xu, C; Ma, L; Nakaoki, T; Suzuki, T. Relaxation Mechanism in Several Kinds of Polyethylene Estimated by Dynamic Mechanical Measurements, Positron Annihilation, X-ray and ^{13}C Solid-State NMR. *Polymer* **2003**, *44*, 4325 – 4340.
- [82] Hronský, V; Murín, J; Uhrin, J. Dynamic-Mechanical and Nuclear Magnetic Resonance Study of Relaxation Processes in Ultra-High Molecular Weight Polyethylene Fibres. *Czech. J. Phys* **2006**, *56*, 289–302.
- [83] Uehara, H; Yamanobe, T; Komoto, T. Relationship between Solid-State Molecular Motion and Morphology for Ultrahigh Molecular Weight Polyethylene Crystallized under Different Conditions. *Macromolecules* **2000**, *33*, 4861–4870.
- [84] Rastogi, S; Yao, Y; Lippits, DR; Höhne, GWH; Graf, R; Spiess, HW; Lemstra, PJ. Segmental Mobility in the Non-crystalline Regions of Semicrystalline Polymers and its Implications on Melting. *Macromol. Rapid Commun.* **2009**, *30*, 826–839.
- [85] Bloembergen, N. *Nuclear Magnetic Relaxation.* **1948**.
- [86] McBrierty, V; Douglass, D. Analysis of NMR Relaxation Times in Polymers with Fiber Symmetry. *J. Magn. Reson.* **1970**, *2*, 352 – 360.
- [87] McCall, D. Nuclear Magnetic Resonance Studies of Molecular Relaxation Mechanisms in Polymers. *J. Elastom. Plast.* **1976**, *8*, 60.
- [88] Davidson, D; Cole, R. Dielectric Relaxation in Glycerol, Propylene Glycol, and *n*-Propanol. *J. Chem. Phys.* **1951**, *19*, 1484.
- [89] Eidmann, G; Savelsberg, R; Blümmler, P; Blümich, B. The NMR-MOUSE, a Mobile Universal Surface Explorer. *J. Magn. Reson., Series A* **1996**, *122*, 104 – 109.
- [90] Blümich, B. *Essential NMR for Scientists and Engineers.* Springer Verlag, **2005**.
- [91] McBrierty, V; Packer, K. *Nuclear Magnetic Resonance in Solid Polymers.* Cambridge University Press, **1993**.
- [92] Perlo, J; Demas, V; Casanova, F; Meriles, CA; Reimer, J; Pines, A; Blümich, B. High-Resolution NMR Spectroscopy with a Portable Single-Sided Sensor. *Science* **2005**, *308*, 1279.
- [93] Perlo, J; Casanova, F; Blümich, B. Ex Situ NMR in Highly Homogeneous Fields: ^1H Spectroscopy. *Science* **2007**, *315*, 1110–1112.

REFERENCES

- [94] Blümich, B; Blümmler, P; Eidmann, G; Guthausen, A; Haken, R; Schmitz, U; Saito, K; Zimmer, G. The NMR-MOUSE: Construction, Excitation, and Applications. *Magn. Reson. Imag.* **1998**, *16*, 479 – 484.
- [95] Anferova, S; Anferov, V; Adams, M; Blümmler, P; Routley, N; Hailu, K; Kupferschläger, K; Mallett, M; Schroeder, G; Sharma, S; Blümich, B. Construction of a NMR-MOUSE with Short Dead Time. *Concepts Magn. Reson.* **2002**, *15*, 15–25.
- [96] Blümich, B; Anferov, V; Anferova, S; Klein, M; Fechete, R; Adams, M; Casanova, F. Simple NMR-MOUSE with a Bar Magnet. *Concepts Magn. Reson.* **2002**, *15*, 255–261.
- [97] Perlo, J; Casanova, F; Blümich, B. Profiles with Microscopic Resolution by Single-Sided NMR. *J. Magn. Reson.* **2005**, *176*, 64 – 70.
- [98] Ernst, R; Bodenhausen, G; Wokaun, A; et al. *Principles of Nuclear Magnetic Resonance in One and Two Dimensions*, volume 332. Clarendon press Oxford, **1987**.
- [99] Geppi, M; Borsacchi, S; Mollica, G; Veracini, CA. Applications of Solid-State NMR to the Study of Organic/Inorganic Multicomponent Materials. *Appl. Spectrosc. Rev.* **2008**, *44*, 1–89.
- [100] Kins, CF; Dudenko, D; Sebastiani, D; Brunklaus, G. Molecular Mechanisms of Additive Fortification in Model Epoxy Resins: A Solid State NMR Study. *Macromolecules* **2010**, *43*, 7200–7211.
- [101] Bohle, A; Brunklaus, G; Hansen, MR; Schleuss, TW; Kilbinger, AFM; Seltmann, J; Spiess, HW. Hydrogen-Bonded Aggregates of Oligoaramide-Poly(ethylene glycol) Block Copolymers. *Macromolecules* **2010**, *43*, 4978–4985.
- [102] Boudenne, A; Ibos, L; Candau, Y; Thomas, S. *Handbook of Multiphase Polymer Systems*. Wiley Online Library, **2012**.
- [103] Chiang, R; Flory, P. Equilibrium between Crystalline and Amorphous Phases in Polyethylene. *J. Am. Chem. Soc.* **1961**, *83*, 2857–2862.
- [104] Isasi, J; Mandelkern, L; Galante, M; Alamo, R. The Degree of Crystallinity of Monoclinic Isotactic Poly(propylene). *J. Polym. Sci., Part B: Polym. Phys.* **1999**, *37*, 323–334.
- [105] Hagemann, H; Snyder, R; Peacock, A; Mandelkern, L. Quantitative Infrared Methods for the Measurement of Crystallinity and its Temperature Dependence: Polyethylene. *Macromolecules* **1989**, *22*, 3600–3606.

REFERENCES

- [106] Gedde, U; Eklund, S; Jansson, JF. Molecular Fractionation in Melt-Crystallized Polyethylene: 2. Effect of Solvent Extraction on the Structure as Studied by Differential Scanning Calorimetry and Gel Permeation Chromatography. *Polymer* **1983**, *24*, 1532 – 1540.
- [107] Hosoda, S; Nozue, Y; Kawashima, Y; Utsumi, S; Nagamatsu, T; Wagener, K; Berda, E; Rojas, G; Baughman, T; Leonard, J. Perfectly Controlled Lamella Thickness and Thickness Distribution: A Morphological Study on ADMET Polyolefins. *Macromol. Symp.* **2009**, *282*, 50–64.
- [108] Kitamaru, R; Horii, F; Murayama, K. Phase Structure of Lamellar Crystalline Polyethylene by Solid-State High-Resolution Carbon-13 NMR Detection of the Crystalline-Amorphous Interphase. *Macromolecules* **1986**, *19*, 636–643.
- [109] Flynn, JH. Thermal Analysis. *Ency. Polym. Sci. Eng.* **1990**, *Supplement Volume*, 690–723.
- [110] Menczel, J; Prime, R. *Thermal Analysis of Polymers*. Wiley Online Library, **2009**.
- [111] Wunderlich, B. *Macromolecular Physics–Volume 3: Crystal Melting*. Academic Press, New York, **1980**.
- [112] TN48. *Polymer Heats of Fusion*. TA Instruments, New Castle, **DE**.
- [113] Litvinov, V; Soliman, M. The Effect of Storage of Poly(propylene) Pipes Under Hydrostatic Pressure and Elevated Temperatures on the Morphology, Molecular Mobility and Failure Behaviour. *Polymer* **2005**, *46*, 3077 – 3089.
- [114] Uehara, H; Aoike, T; Yamanobe, T; Komoto, T. Solid-State ^1H NMR Relaxation Analysis of Ultrahigh Molecular Weight Polyethylene Reactor Powder. *Macromolecules* **2002**, *35*, 2640–2647.
- [115] Engelsberg, M; Lowe, IJ. Free-Induction-Decay Measurements and Determination of Moments in CaF_2 . *Phys. Rev. B* **1974**, *10*, 822–832.
- [116] Lowe, IJ; Vollmers, KW; Punkinen, M. New Method for Measuring the Short Time Behavior of the Free Induction Decay with Applications to Calcium Fluoride and Ammonium Chloride. In *Pulsed Nuclear Magnetic Resonance Spin Dynamic Solids, Proceedings of the First Specialized Colloque Ampere*, pages 70–9. Inst. Nucl. Phys., Krakow, Poland, **1973**.
- [117] Pake, GE. Nuclear Resonance Absorption in Hydrated Crystals: Fine Structure of the Proton Line. *J. Chem. Phys.* **1948**, *16*, 327–336.

REFERENCES

- [118] Look, DC; Lowe, IJ; Northby, JA. Nuclear Magnetic Resonance Study of Molecular Motions in Solid Hydrogen Sulfide. *J. Chem. Phys.* **1966**, *44*, 3441–52.
- [119] Brereton, MG. An Exact Expression for the Transverse Nuclear Magnetic Resonance Relaxation of a Dynamic Scale Invariant Polymer Chain Governed by a Single Relaxation Time. *J. Chem. Phys.* **1991**, *94*, 2136–2142.
- [120] Abragam, A. *The Principles of Nuclear Magnetism*. Oxford University Press, Oxford, **1961**.
- [121] Weibull, W. A Statistical Distribution Function of Wide Applicability. *J. Appl. Mech.* **1951**, *September*, 293–297.
- [122] Klüver, W; Ruland, W. NMR-Studies of Semicrystalline Polymers Using Pulse Techniques. *Prog. Coll. Polym. Sci.* **1978**, *64*, 255–266.
- [123] Bergmann, K; Schmiedberger, H; Unterforsthuber, K. Meßverfahren zur Untersuchung der Protonen-Spin-Spin-Relaxation Ein und Zweiphasiger Polymerer in einem Zeitbereich von Fünf Dekaden. *Colloid Polym. Sci.* **1984**, *262*, 283–293.
- [124] de Langen, M; Luigjes, H; Prins, K. High Pressure NMR Study of Chain Dynamics in the Orthorhombic Phase of Polyethylene. *Polymer* **2000**, *41*, 1183–1191.
- [125] Kristiansen, P; Hansen, E; Pedersen, B. Isothermal Crystallization of Polyethylene Monitored by *in-situ* NMR and Analyzed within the Avrami Model Framework. *Polymer* **2001**, *42*, 1969–1980.
- [126] Blümich, B. *NMR Imaging of Materials*. Oxford University Press, USA, **2000**.
- [127] Blümich, B; Casanova, F; Buda, A; Kremer, K; Wegener, T. Mobile NMR for Analysis of Polyethylene Pipes. *Acta Phys. Pol. A* **2005**, *108*, 13–23.
- [128] Blümich, B; Casanova, F; Buda, A; Kremer, K; Wegener, T. Applications of Mobile NMR for State Assessment of Polyethylene Components. *3R Intern.* **2005**, *44*, 349–354.
- [129] Blümich, B; Buda, A; Kremer, K. Non-Destructive Testing with Mobile NMR. *Gummi Fasern Kunststoffe* **2006**, *59*, 290–293.
- [130] Blümich, B; Adams-Buda, A; Baias, M. Aging of Polyethylene: Nondestructive Testing with Mobile Magnetic Resonance. *GWF, Gas/Erdgas* **2007**, *148*, 95–98.
- [131] Ostroff, ED; Waugh, JS. Multiple Spin Echoes and Spin Locking in Solids. *Phys. Rev. Lett.* **1966**, *16*, 1097–1098.

REFERENCES

- [132] Mehring, M. *Principles of High Resolution NMR in Solids. 2nd Ed.* Springer, Berlin, Heidelberg, New York, **1983**.
- [133] Bull, TE. Effect of RF Radio Frequency Field Inhomogeneities on Spin-Echo Measurements. *Rev. Sci. Instrum.* **1974**, *45*, 232–42.
- [134] Guthausen, A; Zimmer, G; Blmler, P; Blmich, B. Analysis of Polymer Materials by Surface NMR via the MOUSE. *J. Magn. Reson.* **1998**, *130*, 1 – 7.
- [135] Bain, AD; Randall, E. Hahn Spin Echoes in Large Static Gradients Following a Series of 90° Pulses. *J. Magn. Reson., Series A* **1996**, *123*, 49 – 55.
- [136] Hürlimann, M; Griffin, D. Spin Dynamics of Carr-Purcell-Meiboom-Gill-like Sequences in Grossly Inhomogeneous B₀ and B₁ Fields and Application to NMR Well Logging. *J. Magn. Reson.* **2000**, *143*, 120 – 135.
- [137] Packer, KJ; Poplett, IJF; Taylor, MJ. ¹H Nuclear Magnetic Resonance and Spin-Lattice Relaxation in Solid, High-Density Polyethylene. *J. Chem. Soc., Faraday Trans.* **1988**, *84*, 3851–63.
- [138] So, P; Broutman, LJ. Residual Stresses in Polymers and Their Effect on Mechanical Behavior. *Polym. Sci. Eng.* **1976**, *16*, 785–791.
- [139] Sandilands, G; White, J. Effect of Injection Pressure and Crazeing on Internal Stresses in Injection-Moulded Polystyrene. *Polymer* **1980**, *21*, 338 – 343.
- [140] Williams, JG; Hodgkinson, JM; Gray, A. The Determination of Residual Stresses in Plastic Pipe and Their Role in Fracture. *Polym. Sci. Eng.* **1981**, *21*, 822–828.
- [141] Williams, J. *Fracture Mechanics of Polymers*. Wiley, New York, **1984**.
- [142] Mruk, SA. *Encyclopedia of Polymer Science and Engineering. Second Edition*, volume 11. Wiley, New York, **1988**.
- [143] Desai, PC. High Density Polyethylene Pipes for Preventing Accidents During Building Construction. *Pop. Plast. Packag.* **2011**, *56*, 17–19.
- [144] Thermoplastics Materials for Pipes and Fittings for Pressure Applications—Classification, Designation and Design Coefficient, **2005**.
- [145] Sanders, J; Shepherd, M; Belmonte, H; Dear, J. Methods for Determining the In-service Life of Polymer Water Pipes. *J. Mater. Sci.* **2009**, *44*, 4683–4691.
- [146] Verdu, J. Effect of Aging on the Mechanical Properties of Polymeric Materials. *J. Macromol. Sci., Part A: Pure Appl. Chem.* **1994**, *31*, 1383–1398.

REFERENCES

- [147] Viebke, J; Hedenqvist, M; Gedde, UW. Antioxidant Efficiency Loss by Precipitation and Diffusion to Surrounding Media in Polyethylene Hot-Water Pipes. *Polym. Sci. Eng.* **1996**, *36*, 2896–2904.
- [148] Ward, A; Lu, X; Huang, Y; Brown, N. The Mechanism of Slow Crack Growth in Polyethylene by an Environmental Stress Cracking Agent. *Polymer* **1991**, *32*, 2172 – 2178.
- [149] Eriksson, P; Ifwarson, M. Paper 40A. In *Proceedings Plastic Pipes VI*. Plastic and Rubber Institute, York, UK, **1985**.
- [150] Lu, X; Brown, N. The Ductile-Brittle Transition in a Polyethylene Copolymer. *J. Mater. Sci.* **1990**, *25*, 29–34.
- [151] Viebke, J; Elble, E; Ifwarson, M; Gedde, UW. Degradation of Unstabilized Medium-Density Polyethylene Pipes in Hot-Water Applications. *Polym. Sci. Eng.* **1994**, *34*, 1354–1361.
- [152] Andersson, U. Which Factors Control the Lifetime of Plastic Pipes and How the Lifetime Can be Extrapolated. In *Proceedings Plastic Pipes XI*. Bodycote Polymer AB, Nyköping, Sweden, **2001**.
- [153] Ifwarson, M; Eriksson, P. Experience from 12 Years Evaluation of Crosslinked Polyethylene. *Kunststoffe* **1986**, *76*, 245–8.
- [154] Eriksson, P; Ifwarson, M. Occurrence of Brittle Fracture in Polyethylene. *Kunststoffe* **1986**, *76*, 512–16.
- [155] Gedde, UW; Ifwarson, M. Molecular Structure and Morphology of Crosslinked Polyethylene in an Aged Hot-Water Pipe. *Polym. Sci. Eng.* **1990**, *30*, 202–10.
- [156] Michler, G; Balta-Calleja, F. *Mechanical Properties of Polymers Based on Nanostructure and Morphology*, volume 71. CRC Press, **2005**.
- [157] Colin, X; Audouin, L; Verdu, J; Rozental-Evesque, M; Rabaud, B; Martin, F; Bourguine, F. Aging of Polyethylene Pipes Transporting Drinking Water Disinfected by Chlorine Dioxide. I. Chemical Aspects. *Polym. Sci. Eng.* **2009**, *49*, 1429–1437.
- [158] Kelen, T. *Polymer Degradation*. Van Nostrand Reinhold Company, New York, **1983**.
- [159] Khelidj, N; Colin, X; Audouin, L; Verdu, J. A Simplified Approach for the Lifetime Prediction of PE in Nuclear Environments. *Nucl. Instrum. Meth. B* **2005**, *236*, 88 – 94.
- [160] Colin, X; Audouin, L; Verdu, J; Rozental-Evesque, M; Rabaud, B; Martin, F; Bourguine, F. Aging of Polyethylene Pipes Transporting Drinking Water Disinfected by Chlorine Dioxide. Part II. Lifetime Prediction. *Polym. Sci. Eng.* **2009**, *49*, 1642–1652.

REFERENCES

- [161] Gedde, UW; Viebke, J; Leijström, H; Ifwarson, M. Long-Term Properties of Hot-Water Polyolefin Pipes – a Review. *Polym. Sci. Eng.* **1994**, *34*, 1773–1787.
- [162] Viebke, J; Gedde, UW. Antioxidant Diffusion in Polyethylene Hot-Water Pipes. *Polym. Sci. Eng.* **1997**, *37*, 896–911.
- [163] Yu, W; Azhdar, B; Andersson, D; Reitberger, T; Hassinen, J; Hjertberg, T; Gedde, U. Deterioration of Polyethylene Pipes Exposed to Water Containing Chlorine Dioxide. *Polym. Degrad. Stab.* **2011**, *96*, 790 – 797.
- [164] Brown, N. Intrinsic Lifetime of Polyethylene Pipelines. *Polym. Sci. Eng.* **2007**, *47*, 477–480.
- [165] Hoffman, JD. Theoretical Aspects of Polymer Crystallization with Chain Folds: Bulk Polymers. *Polym. Sci. Eng.* **1964**, *4*, 315–362.
- [166] Goldman, M; Shen, L. Spin-Spin Relaxation in LaF₃. *Phys. Rev.* **1966**, *144*, 321–331.
- [167] Assink, RA. Nuclear Spin Diffusion between Polyurethane Microphases. *Macromolecules* **1978**, *11*, 1233–1237.
- [168] Caravatti, P; Neuenschwander, P; Ernst, RR. Characterization of Heterogeneous Polymer Blends by Two-Dimensional Proton Spin Diffusion Spectroscopy. *Macromolecules* **1985**, *18*, 119–122.
- [169] Schmidt-Rohr, K; Clauss, J; Blümich, B; Spiess, HW. Miscibility of Polymer Blends Investigated by ¹H Spin Diffusion and ¹³C NMR Detection. *Magn. Reson. Chem.* **1990**, *28*, S3–S9.
- [170] Schmidt-Rohr, K; Clauss, J; Spiess, HW. Correlation of Structure, Mobility, and Morphological Information in Heterogeneous Polymer Materials by Two-Dimensional Wideline-Separation NMR Spectroscopy. *Macromolecules* **1992**, *25*, 3273–3277.
- [171] Buda, A; Demco, DE; Bertmer, M; Blümich, B; Reining, B; Keul, H; Höcker, H. Domain Sizes in Heterogeneous Polymers by Spin Diffusion Using Single-Quantum and Double-Quantum Dipolar Filters. *Solid State Nucl. Magn. Reson.* **2003**, *24*, 39 – 67.
- [172] Clauss, J; Schmidt-Rohr, K; Spiess, HW. Determination of Domain Sizes in Heterogeneous Polymers by Solid-State NMR. *Acta Polym.* **1993**, *44*, 1–17.
- [173] VanderHart, DL. Proton Spin Diffusion Studies of Polymer Blends Having Modest Monomer Size: 1. Polystyrene/Poly(xylylene ether), a Miscible Blend. *Macromolecules* **1994**, *27*, 2837–2845.

REFERENCES

- [174] VanderHart, DL; Manley, RSJ; Barnes, JD. Proton Spin Diffusion Studies of Polymer Blends Having Modest Monomer Size. 2. Blends of Cellulose with either Poly(acrylonitrile) or Poly(4-vinylpyridine). *Macromolecules* **1994**, *27*, 2826–2836.
- [175] VanderHart, DL; Asano, A; Gilman, JW. Solid-State NMR Investigation of Paramagnetic Nylon-6 Clay Nanocomposites. 1. Crystallinity, Morphology, and the Direct Influence of Fe³⁺ on Nuclear Spins. *Chem. Mater.* **2001**, *13*, 3781–3795.
- [176] Caravatti, P; Neuenschwander, P; Ernst, RR. Characterization of Polymer Blends by Selective Proton Spin-Diffusion NMR Measurements. *Macromolecules* **1986**, *19*, 1889–1895.
- [177] Cheung, TTP; Gerstein, BC. Proton Nuclear Magnetic Resonance Studies of Domain Structures in Polymers. *J. Appl. Phys.* **1981**, *52*, 5517–28.
- [178] Cheung, TTP. Modulation of Proton NMR Free Induction Decay by Spin Diffusion. *J. Chem. Phys.* **1982**, *76*, 1248–54.
- [179] Glatter, O; Kratky, O. *Small Angle X-ray Scattering*. Academic press London, **1982**.
- [180] Higgins, J; Benoît, H. *Polymers and Neutron Scattering*. Clarendon Press Oxford, **1994**.
- [181] Buda, A; Demco, DE; Bertmer, M; Blümich, B; Litvinov, VM; Penning, JP. General Analytical Description of Spin-Diffusion for a Three-Domain Morphology. Application to Melt-Spun Nylon 6 Fibers. *J. Phys. Chem. B* **2003**, *107*, 5357–5370.
- [182] Buda, A. *Solid-State NMR for Advanced Material Characterization*. Ph.D. thesis, Rheinisch-Westfälischen Technischen Hochschule Aachen, **2004**.
- [183] Crank, J. *The Mathematics of Diffusion*. Oxford Univ. Press, **1975**.
- [184] Carslaw, HS; Jaeger, JC. *Conduction of Heat in Solids*. Oxford Univ. Press, **1986**.
- [185] Gedde, UW; Mattozzi, A. Polyethylene Morphology. *Adv. Polym. Sci.* **2004**, *169*, 29–74.
- [186] Goldman, M. *Spin Temperature and Nuclear Magnetic Resonance in Solids*. Clarendon Press Oxford, **1970**.
- [187] Reneker, DH. Point Dislocations in Crystals of High Polymer Molecules. *J. Polym. Sci.* **1962**, *59*, S39–S42.
- [188] Shah, A; Stepanov, EV; Klein, M; Hiltner, A; Baer, E. Study of Polyethylene Pipe Resins by a Fatigue Test that Simulates Crack Propagation in a Real Pipe. *J. Mater. Sci.* **1998**, *33*, 3313–3319.

REFERENCES

- [189] Hubert, L; David, L; Séguéla, R; Vigier, G; Degoulet, C; Germain, Y. Physical and Mechanical Properties of Polyethylene for Pipes in Relation to Molecular Architecture. I. Microstructure and Crystallisation Kinetics. *Polymer* **2001**, *42*, 8425 – 8434.
- [190] Tanaka, H. Proton Spin-Lattice and Spin-Spin Relaxation Times in Isotactic Polypropylene. II. Effects of Stretching Ratio and Temperature. *J. Appl. Polym. Sci.* **1983**, *28*, 1707–1715.
- [191] Lustiger, A. The Molecular Mechanism of Slow Crack Growth in Polyethylene. **1983**.
- [192] Glenz, W; Peterlin, A; Wilke, W. Crystallite Size in Highly Drawn Polyethylene. *J. Polym. Sci., Part A-2: Polym. Phys.* **1971**, *9*, 1243–54.
- [193] Peterlin, A. Morphology and Fracture of Drawn Crystalline Polymers. *J. Macromol. Sci., Part B* **1973**, *8*, 83–100.
- [194] Halse, Y; Lord Jr, A; Koerner, R. *Geosynthetic Testing for Waste Containment Application, ASTM STP 1081–Ductile to Brittle Transition Time in Polyethylene Geomembrane Sheet*. American Society for Testing and Materials, Philadelphia, **1990**.
- [195] Brown, N; Lu, X; Huang, YL; Qian, R. Slow Crack Growth in Polyethylene - A Review. *Makromol. Chem. Macromol. Symp.* **1991**, *41*, 55–67.
- [196] Brown, N; Bhattacharya, SK. The Initiation of Slow Crack Growth in Linear Polyethylene under Single Edge Notch Tension and Plane Strain. *J. Mater. Sci.* **1985**, *20*, 4553–4560.
- [197] Lu, X; Brown, N. Effect of Thermal History on the Initiation of Slow Crack Growth in Linear Polyethylene. *Polymer* **1987**, *28*, 1505 – 1511.
- [198] Wang, XQ; Brown, N. The Stress and Strain Fields in the Neighbourhood of a Notch in Polyethylene. *Polymer* **1989**, *30*, 1456 – 1461.
- [199] Brown, N. Slow Crack Growth-Notches-Pressurized Polyethylene Pipes. *Polym. Sci. Eng.* **2007**, *47*, 1951–1955.
- [200] Barry, D; Delatycki, O. Static Fatigue Fracture of Polyethylene: A Morphological Analysis. *J. Polym. Sci., Part B: Polym. Phys.* **1987**, *25*, 883–899.
- [201] Barry, D; Delatycki, O. The Effect of Molecular Structure and Polymer Morphology on the Fracture Resistance of High-Density Polyethylene. *Polymer* **1992**, *33*, 1261 – 1265.
- [202] Lu, X; Qian, R; Brown, N. Notchology-the Effect of the Notching Method on the Slow Crack Growth Failure in a Tough Polyethylene. *J. Mater. Sci.* **1991**, *26*, 881–888.

REFERENCES

- [203] Rose, LJ; Channell, AD; Frye, CJ; Capaccio, G. Slow Crack Growth in Polyethylene: A Novel Predictive Model Based on the Creep of Craze Fibrils. *J. Appl. Polym. Sci.* **1994**, *54*, 2119–2124.
- [204] Lu, X; Brown, N. Unification of Ductile Failure and Slow Crack Growth in an Ethylene-Octene Copolymer. *J. Mater. Sci.* **1991**, *26*, 612–620.
- [205] Brown, N; Lu, X. A Fundamental Theory for Slow Crack Growth in Polyethylene. *Polymer* **1995**, *36*, 543 – 548.
- [206] Iijima, S. Helical Microtubules of Graphitic Carbon. *Nature* **1991**, *354*, 56–58.
- [207] Frank, S; Poncharal, P; Wang, ZL; Heer, WAd. Carbon Nanotube Quantum Resistors. *Science* **1998**, *280*, 1744–1746.
- [208] Yu, MF; Lourie, O; Dyer, MJ; Moloni, K; Kelly, TF; Ruoff, RS. Strength and Breaking Mechanism of Multiwalled Carbon Nanotubes Under Tensile Load. *Science* **2000**, *287*, 637–640.
- [209] Yu, MF; Files, BS; Arepalli, S; Ruoff, RS. Tensile Loading of Ropes of Single Wall Carbon Nanotubes and their Mechanical Properties. *Phys. Rev. Lett.* **2000**, *84*, 5552–5555.
- [210] Collins, P; Avouris, P. Nanotubes for Electronics. *Sci. Am.* **2000**, *283*, 62–69.
- [211] Ajayan, PM; Stephan, O; Colliex, C; Trauth, D. Aligned Carbon Nanotube Arrays Formed by Cutting a Polymer Resin-Nanotube Composite. *Science* **1994**, *265*, 1212–1214.
- [212] Shonaike, G; Advani, S. *Advanced Polymeric Materials: Structure Property Relationships*. CRC, **2003**.
- [213] Haggemueller, R; Zhou, W; Fischer, J; Winey, K. Production and Characterization of Polymer Nanocomposites with Highly Aligned Single-Walled Carbon Nanotubes. *J. Nanosci. Nanotechnol.* **2003**, *3*, 105–110.
- [214] Uehara, H; Kato, K; Kakiage, M; Yamanobe, T; Komoto, T. Single-Walled Carbon Nanotube Nucleated Solution-Crystallization of Polyethylene. *J. Phys. Chem. C* **2007**, *111*, 18950–18957.
- [215] Toti, A; Giambastiani, G; Bianchini, C; Meli, A; Bredeau, S; Dubois, P; Bonduel, D; Claes, M. Tandem Action of Early–Late Transition Metal Catalysts for the Surface Coating of Multiwalled Carbon Nanotubes with Linear Low-Density Polyethylene. *Chem. Mater.* **2008**, *20*, 3092–3098.

REFERENCES

- [216] Park, S; Yoon, SW; Choi, H; Lee, JS; Cho, WK; Kim, J; Park, HJ; Yun, WS; Choi, CH; Do, Y; Choi, IS. Pristine Multiwalled Carbon Nanotube/Polyethylene Nanocomposites by Immobilized Catalysts. *Chem. Mater.* **2008**, *20*, 4588–4594.
- [217] Grady, BP; Arthur, DJ; Ferguson, J. Single-Walled Carbon Nanotube/Ultrahigh-Molecular-Weight Polyethylene Composites with Percolation at Low Nanotube Contents. *Polym. Sci. Eng.* **2009**, *49*, 2440–2446.
- [218] Park, S; Choi, IS. Production of Ultrahigh-Molecular-Weight Polyethylene/Pristine MWCNT Composites by Half-Titanocene Catalysts. *Adv. Mater.* **2009**, *21*, 902–905.
- [219] Yu, H; Liu, J; Wang, Z; Jiang, Z; Tang, T. Combination of Carbon Nanotubes with Ni₂O₃ for Simultaneously Improving the Flame Retardancy and Mechanical Properties of Polyethylene. *J. Phys. Chem. C* **2009**, *113*, 13092–13097.
- [220] Mai, F; Wang, K; Yao, M; Deng, H; Chen, F; Fu, Q. Superior Reinforcement in Melt-Spun Polyethylene/Multiwalled Carbon Nanotube Fiber through Formation of a Shish-Kebab Structure. *J. Phys. Chem. B* **2010**, *114*, 10693–10702.
- [221] Xiang, F; Wu, J; Liu, L; Huang, T; Wang, Y; Chen, C; Peng, Y; Jiang, C; Zhou, Z. Largely Enhanced Ductility of Immiscible High Density Polyethylene/Polyamide 6 Blends via Nano-Bridge Effect of Functionalized Multiwalled Carbon Nanotubes. *Polym. Adv. Technol.* **2011**, *22*, 2533–2542.
- [222] Xie, R; Wang, J; Yang, Y; Jiang, K; Li, Q; Fan, S. Aligned Carbon Nanotube Coating on Polyethylene Surface Formed by Microwave Radiation. *Compos. Sci. Technol.* **2011**, *72*, 85 – 90.
- [223] Zhang, Q; Lippits, DR; Rastogi, S. Dispersion and Rheological Aspects of SWNTs in Ultrahigh Molecular Weight Polyethylene. *Macromolecules* **2006**, *39*, 658–666.
- [224] Jeon, K; Lumata, L; Tokumoto, T; Steven, E; Brooks, J; Alamo, RG. Low Electrical Conductivity Threshold and Crystalline Morphology of Single-Walled Carbon Nanotubes – High Density Polyethylene Nanocomposites Characterized by SEM, Raman Spectroscopy and AFM. *Polymer* **2007**, *48*, 4751 – 4764.
- [225] Linares, A; Canalda, JC; Cagiao, ME; García-Gutiérrez, MC; Nogales, A; Martín-Gullón, I; Vera, J; Ezquerra, TA. Broad-Band Electrical Conductivity of High Density Polyethylene Nanocomposites with Carbon Nanoadditives: Multiwall Carbon Nanotubes and Carbon Nanofibers. *Macromolecules* **2008**, *41*, 7090–7097.
- [226] Schönhals, A; Goering, H; Costa, FR; Wagenknecht, U; Heinrich, G. Dielectric Properties of Nanocomposites Based on Polyethylene and Layered Double Hydroxide. *Macromolecules* **2009**, *42*, 4165–4174.

REFERENCES

- [227] Yang, J; Wang, C; Wang, K; Zhang, Q; Chen, F; Du, R; Fu, Q. Direct Formation of Nanohybrid Shish-Kebab in the Injection Molded Bar of Polyethylene/Multiwalled Carbon Nanotubes Composite. *Macromolecules* **2009**, *42*, 7016–7023.
- [228] Vega, JF; Martínez-Salazar, J; Trujillo, M; Arnal, ML; Müller, AJ; Bredeau, S; Dubois, P. Rheology, Processing, Tensile Properties, and Crystallization of Polyethylene/Carbon Nanotube Nanocomposites. *Macromolecules* **2009**, *42*, 4719–4727.
- [229] Kim, J; Kwak, S; Hong, SM; Lee, JR; Takahara, A; Seo, Y. Nonisothermal Crystallization Behaviors of Nanocomposites Prepared by *InSitu* Polymerization of High-Density Polyethylene on Multiwalled Carbon Nanotubes. *Macromolecules* **2010**, *43*, 10545–10553.
- [230] Zheng, X; Xu, Q. Comparison Study of Morphology and Crystallization Behavior of Polyethylene and Poly(ethylene oxide) on Single-Walled Carbon Nanotubes. *J. Phys. Chem. B* **2010**, *114*, 9435–9444.
- [231] Wang, Y; Ju, S; Huang, T; Wang, H. Modeling of Polyethylene, Poly(l-lactide), and CNT Composites: a Dissipative Particle Dynamics Study. *Nanoscale Res. Lett.* **2011**, *6*, 433.
- [232] Wang, YC; Ju, SP; Cheng, HZ; Lu, JM; Wang, HH. Modeling of Polyethylene and Functionalized CNT Composites: A Dissipative Particle Dynamics Study. *J. Phys. Chem. C* **2010**, *114*, 3376–3384.
- [233] Jia, L; Qingsheng, Y. Molecular Dynamics Simulation for Mechanical Properties of CNT/Polyethylene Composites. *J. Phys.: Conference Series* **2009**, *188*, 012052.
- [234] Mokashi, VV; Qian, D; Liu, Y. A Study on the Tensile Response and Fracture in Carbon Nanotube-Based Composites Using Molecular Mechanics. *Compos. Sci. Technol.* **2007**, *67*, 530 – 540.
- [235] Kuroki, S; Kimura, H; Ando, I. Structural Characterization of Si-Based Polymer Materials by Solid-State NMR Spectroscopy. Technical report, **2004**.
- [236] Grandjean, J. Solid-State NMR Study of Modified Clays and Polymer/Clay Nanocomposites. *Clay Miner.* **2006**, *41*, 567–586.
- [237] Groenewoud, W. *Characterisation of Polymers by Thermal Analysis*. Elsevier Science, **2001**.
- [238] Mittal, V. *Thermally Stable and Flame Retardant Polymer Nanocomposites*. Cambridge University Press, **2011**.

REFERENCES

- [239] Lauritzen, J, John I.; Hoffman, JD. Theory of Formation of Polymer Crystals with Folded Chains in Dilute Solution. *J. Res. Natl. Bur. Stand., Sec. A. Phys. Chem.* **1960**, *64A*, 73–102.
- [240] Wunderlich, B; Sullivan, P; Arakawa, T; Dicyan, AB; Flood, JF. Thermodynamics of Crystalline Linear High Polymers. III. Thermal Breakdown of the Crystalline Lattice of Polyethylene. *J. Polym. Sci., Part A: General Papers* **1963**, *1*, 3581–3596.
- [241] Wunderlich, B; Arakawa, T. Polyethylene Crystallized from the Melt under Elevated Pressure. *J. Polym. Sci., Part A: General Papers* **1964**, *2*, 3697–3706.
- [242] Illers, VKH; Hendus, H. Schmelzpunkt und Kristallitgröße von aus Schmelze und lösung Kristallisiertem Polyäthylen. *Macromol. Chem.* **1968**, *113*, 1–22.
- [243] Weeks, J. Melting Temperature and Change of Lamellar Thickness with Time for Bulk Polyethylene. *J. Res. Natl. Bur. Stand., Sec. A. Phys. Chem.* **1963**, *67*, 441–451.
- [244] Brown, R; Eby, R. Effect of Crystallization Conditions and Heat Treatment on Polyethylene: Lamellar Thickness, Melting Temperature, and Density. *J. Appl. Phys.* **1964**, *35*, 1156–1161.
- [245] Maxwell, R; Balazs, B. Residual Dipolar Coupling for the Assessment of Cross-Link Density Changes in γ -Irradiated Silica-PDMS Composite Materials. *J. Chem. Phys.* **2002**, *116*, 10492.
- [246] Wang, M; Bertmer, M; Demco, DE; Blümich, B; Litvinov, VM; Barthel, H. Indication of Heterogeneity in Chain-Segment Order of a PDMS Layer Grafted onto a Silica Surface by ^1H Multiple-Quantum NMR. *Macromolecules* **2003**, *36*, 4411–4413.
- [247] Valentín, JL; Mora-Barrantes, I; Carretero-González, J; López-Manchado, MA; Sotta, P; Long, DR; Saalwächter, K. Novel Experimental Approach To Evaluate Filler–Elastomer Interactions. *Macromolecules* **2010**, *43*, 334–346.
- [248] Collignon, J; Sillescu, H; Spiess, HW. Pseudo-Solid Echoes of Proton and Deuteron NMR in Polyethylene Melts. *Colloid Polym. Sci.* **1981**, *259*, 220–226.
- [249] Callaghan, PT; Samulski, ET. Molecular Ordering and the Direct Measurement of Weak Proton–Proton Dipolar Interactions in a Rubber Network. *Macromolecules* **1997**, *30*, 113–122.
- [250] Fischer, E; Grinberg, F; Kimmich, R; Hafner, S. Characterization of Polymer Networks Using the Dipolar Correlation Effect on the Stimulated Echo and Field-Cycling Nuclear-Magnetic Resonance Relaxometry. *J. Chem. Phys.* **1998**, *109*, 846.

REFERENCES

- [251] Fechete, R; Demco, D; Blümich, B. Chain Orientation and Slow Dynamics in Elastomers by Mixed Magic-Hahn Echo Decays. *J. Chem. Phys.* **2003**, *118*, 2411.
- [252] Brereton, MG. NMR Transverse Relaxation Function Calculated for Constrained Polymer Chains: Application to Entanglements and Networks. *Macromolecules* **1990**, *23*, 1119–1131.
- [253] Demco, DE; Hafner, S; Fuelber, C; Graf, R; Spiess, HW. Two-Dimensional Proton Magnetization-Exchange NMR Spectroscopy in Cross-Linked Elastomers. *J. Chem. Phys.* **1996**, *105*, 11285–11296.
- [254] Litvinov, VM. EPDM/PP Thermoplastic Vulcanizates As Studied by Proton NMR Relaxation: Phase Composition, Molecular Mobility, Network Structure in the Rubbery Phase, and Network Heterogeneity. *Macromolecules* **2006**, *39*, 8727–8741.
- [255] Şerbescu, A; Saalwächter, K. Particle-Induced Network Formation in Linear PDMS Filled with Silica. *Polymer* **2009**, *50*, 5434 – 5442.
- [256] Baum, J; Munowitz, M; Garroway, AN; Pines, A. Multiple-Quantum Dynamics in Solid State NMR. *J. Chem. Phys.* **1985**, *83*, 2015–25.
- [257] Baum, J; Pines, A. NMR Studies of Clustering in Solids. *J. Am. Chem. Soc.* **1986**, *108*, 7447–7454.
- [258] Wiesmath, A; Filip, C; Demco, D; Blümich, B. Double-Quantum-Filtered NMR Signals in Inhomogeneous Magnetic Fields. *J. Magn. Reson.* **2001**, *149*, 258 – 263.
- [259] Fechete, R; Demco, DE; Blümich, B. Segmental Anisotropy in Strained Elastomers by ^1H NMR of Multipolar Spin States. *Macromolecules* **2002**, *35*, 6083–6085.
- [260] Saalwächter, K. Detection of Heterogeneities in Dry and Swollen Polymer Networks by Proton Low-Field NMR Spectroscopy. *J. Am. Chem. Soc.* **2003**, *125*, 14684–14685.
- [261] Voda, M; Demco, D; Perlo, J; Orza, R; Blümich, B. Multispin Moments Edited by Multiple-Quantum NMR: Application to Elastomers. *J. Magn. Reson.* **2005**, *172*, 98 – 109.
- [262] Yen, YS. *Multiple-Quantum NMR in Solids*. Ph.D. thesis, Lawrence Berkeley, University of California, **1982**.
- [263] Blümich, B; Kaiser, R. Magnetization Exchange, Zero and Double Quantum Spectra in Stochastic NMR Spectroscopy. *J. Magn. Reson.* **1983**, *54*, 486 – 501.

REFERENCES

- [264] Weitekamp, DP. Time-Domain Multiple-Quantum NMR. *Adv. Magn. Reson.* **1983**, *11*, 111–274.
- [265] Bowden, G; Hutchison, W. Tensor Operator Formalism for Multiple-Quantum NMR. 1. Spin-1 Nuclei. *J. Magn. Reson.* **1986**, *67*, 403 – 414.
- [266] Munowitz, M; Pines, A. Multiple-Quantum Nuclear Magnetic Resonance Spectroscopy. *Science* **1986**, *233*, 525–531.
- [267] Navon, G; Shinar, H; Eliav, U; Seo, Y. Multiquantum Filters and Order in Tissues. *NMR Biomed.* **2001**, *14*, 112–132.
- [268] Saalwächter, K; Ziegler, P; Spyckerelle, O; Haidar, B; Vidal, A; Sommer, JU. ^1H Multiple-Quantum Nuclear Magnetic Resonance Investigations of Molecular Order Distributions in Poly(dimethylsiloxane) Networks: Evidence for a Linear Mixing Law in Bimodal Systems. *J. Chem. Phys.* **2003**, *119*, 3468–3482.
- [269] Saalwächter, K; Herrero, B; López-Manchado, MA. Chain Order and Cross-Link Density of Elastomers As Investigated by Proton Multiple-Quantum NMR. *Macromolecules* **2005**, *38*, 9650–9660.
- [270] Chassé, W; Lang, M; Sommer, JU; Saalwächter, K. Cross-Link Density Estimation of PDMS Networks with Precise Consideration of Networks Defects. *Macromolecules* **2012**, *45*, 899–912.
- [271] Schneider, M; Gasper, L; Demco, D; Blümich, B. Residual Dipolar Couplings by ^1H Dipolar-Encoded Longitudinal Magnetization, Double-and Triple-Quantum Nuclear Magnetic Resonance in Cross-Linked Elastomers. *J. Chem. Phys.* **1999**, *111*, 402.
- [272] Avrami, M. Granulation, Phase Change and Microstructure. Kinetics of Phase Change. III. *J. Chem. Phys.* **1941**, *9*, 177–84.
- [273] Kissinger, HE. Variation of Peak Temperature with Heating rate in Differential Thermal Analysis. *J. Res. Natl. Bur. Stand.* **1956**, *57*, 217–21.
- [274] Hoffman, JD; Lauritzen, J, John I. Crystallization of Bulk Polymers with Chain Folding: Theory of Growth of Lamellar Spherulites. *J. Res. Natl. Bur. Stand., Sec. A. Phys. Chem.* **1961**, *65A*, 297–336.
- [275] Schultz, JM. *Polymer Crystallization: The Development of Crystallines in Thermoplastic Polymers*. American Chemical Society, **2001**.
- [276] Mandelkern, L. *Crystallization of Polymers: Kinetics and Mechanisms*, volume 2. Cambridge Univiveristy Press, **2004**.

REFERENCES

- [277] Mark, J; Ngai, K; Graessley, W; Mandelkern, L; Samulski, E; Koenig, J; Wignall, G. *Physical Properties of Polymers, 3rd Edition*. Cambridge University Press, **2004**.
- [278] Reiter, G; Strobl, G. *Progress in Understanding of Polymer Crystallization*, volume 714. Springer Verlag, **2007**.
- [279] Prabhakar, C; Bala, K, Krishna. A Review on Carbon Nanotubes. *Res. J. Pharm., Biol. Chem. Sci.* **2011**, *2*, 850–854.
- [280] Chavan, R; Desai, U; Mhatre, P; Chinchole, R. A Review: Carbon Nanotubes. *Int. J. Pharm. Sci. Rev. Res.* **2012**, *13*, 125–134.
- [281] Reneker, DH; Geil, PH. Morphology of Polymer Single Crystals. *J. Appl. Phys.* **1960**, *31*, 1916–25.
- [282] Pennings, A; Kiel, A. Fractionation of Polymers by Crystallization from Solution, III. On the Morphology of Fibrillar Polyethylene Crystals Grown in Solution. *Colloid Polym. Sci.* **1965**, *205*, 160–162.
- [283] Li, C; Li, L; Cai, W; Kodjie, S; Tenneti, K. Nanohybrid Shish-Kebabs: Periodically Functionalized Carbon Nanotubes. *Adv. Mater.* **2005**, *17*, 1198–1202.
- [284] Li, L; Li, B; Hood, MA; Li, CY. Carbon Nanotube Induced Polymer Crystallization: The Formation of Nanohybrid Shish-Kebabs. *Polymer* **2009**, *50*, 953 – 965.
- [285] Liang, Y; Zheng, G; Han, W; Liu, C; Chen, J; Li, Q; Liu, B; Shen, C; Peng, X. Nano-Hybrid Shish-Kebab: Isotactic Polypropylene Epitaxial Growth on Electrospun Polyamide 66 Nanofibers via Isothermal Crystallization. *Mater. Lett.* **2011**, *65*, 653 – 656.
- [286] Grady, BP. Effects of Carbon Nanotubes on Polymer Physics. *J. Polym. Sci., Part B Polym. Phys.* **2012**, *50*, 591–623.
- [287] Claessen, O; Grefen, D; Mang, T; Dikland, HG; van Duin, M. Ageing Behaviour of White Window Sealings Based on Peroxide-Cured EPDM. *Kautsch. Gummi Kunstst.* **2010**, *63*, 350–360.
- [288] Xiao, K; Zhang, L; Zarudi, I. Mechanical and Rheological Properties of Carbon Nanotube-Reinforced Polyethylene Composites. *Compos. Sci. Technol.* **2007**, *67*, 177 – 182.
- [289] Kaplan, ML; Bovey, FA; Cheng, HN. Simplified Method of Calibrating Thermometric Nuclear Magnetic Resonance Standards. *Anal. Chem.* **1975**, *47*, 1703–1705.
- [290] Ammann, C; Meier, P; Merbach, A. A Simple Multinuclear NMR Thermometer. *J. Magn. Reson.* **1982**, *46*, 319 – 321.

Acknowledgements

First of all, I would like to thank Prof. Bernhard Blümich, an invaluable advisor. It is a great honor for me to be a member of Macromolecular Chemistry group and to work under his guidance. I have benefited a lot from his supports, and have learned systematically about how to do scientific research as well as how to be a good scientist from him.

Many thanks go to Dr. Alina Adams, who supports from every aspect for my whole Ph.D. work. For all helps including the initializations of NMR principle study, the solutions for the experimental problems, the nice discussions about my projects, the cares to my life, and many else.

I would also like to thank Dr. Mirko Wenzel from SKZ as well as Prof. Thomas Mang from IAP. The collaborations with them helped the progress of my projects tremendously.

Thanks a lot for the huge supports from Dr. Markus Küppers and Dipl.-Ing. Michael Adams. I could not have achieved my Ph.D. thesis such efficiently without their helps.

Many thanks for the tremendous supports from all the members in our group, who also made my last three years really memorable. I would also like to thank Lei Li from DWI for all the important helps.

My special thanks go to Markus Raue and Tyler Meldrum, my colleagues and also my friends. It was a great pleasure to share the same office with them. I appreciate their helps for my projects and language sincerely, and I always enjoy the discussions and entertainments with them.

Thanks lot for the supports from all my family members and my friends, especially, my sister. Finally, I would like to express my deepest thank to my parents, who love me and are always there for me. My life is exquisite because the parts of theirs.

16th December, 2012
RWTH-Aachen University

Curriculum Vitæ

Personal Details

Surname: Sun
First name: Ning
Birth date: 24th April, 1984
Birth place: Zhejiang, China
Nationality: Chinese

Education

09/1999 – 06/2002 **A-Levels**
Yiwu NO. 3 High School, China
09/2002 – 06/2006 **B. Eng. Polymer Material and Engineering**
Qingdao University, China
09/2006 – 03/2009 **M. Eng. Material Science and Engineering**
Shanghai Jiao Tong University, China
08/2009 – present **Ph.D. Macromolecular Chemistry**
RWTH-Aachen University, Germany
14/12/2012 **Defense for the Doctoral Degree in Natural Science**

Selected Publications

- N. Sun, M. Raue, D. Heinze, B. Blümich, T. Mang, and A. Adams. Morphology and Molecular Dynamics of MWNT/LDPE Composite: Chain Confinement due to the Presence of CNTs. (in preparation)
- N. Sun, M. Wenzel, B. Blümich, and A. Adams. Morphology and Molecular Dynamics of the HDPE Pipes due to the Storage under Hydrostatic Pressure and Elevated Temperature. (in preparation)
- N. Sun, M. Wenzel, B. Blümich, and A. Adams. Morphology and Phase Composition of Polyethylene: A Combined Study by DSC, High- and Low-Field NMR. (in preparation)
- N. Sun, D.-X. Chen, H.-C. Gu, and X.-L. Wang. Experimental Study on T_2 Relaxation Time of Protons in Water Suspensions of Iron-oxide Nanoparticles: Waiting Time Dependence. *J. Magn. Magn. Mater.*, **2009**, *321*, 2971–2975.

